ABSTRACT

Title of dissertation: DIRECTED FLOW IN HEAVY ION COLLISIONS AT $\sqrt{s_{NN}} = 2.76$ TeV

Jaime Gomez, Doctor of Philosophy, 2015

Dissertation directed by: Professor Alice Mignerey
Department of Chemistry

The directed flow of charged particles at midrapidity is measured in Pb-Pb collisions at $\sqrt{s_{NN}} = 2.76$ TeV relative to the collision Event Plane, defined by the participant plane using various subdetectors. The rapidity-even directed flow component is measured for the first time using an Event Plane weighted by the transverse momentum of the emitted charged hadrons and found to be largely independent of pseudorapidity with a sign change at transverse momenta p_T between 1.2 and 1.7 GeV/c. These results are compared to measurements made by two other experiments at the LHC. Combined with the observation from ALICE of a vanishing rapidity-even p_T shift along the spectator deflection plane is strong evidence for dipole like initial density fluctuations in the overlap zone of the nuclei. These observations open new possibilities for investigation of the initial conditions in heavy-ion collisions with spectator nucleons.

DIRECTED FLOW IN HEAVY ION COLLISIONS AT $\sqrt{s_{NN}} = 2.76$ GeV

by

Jaime Arturo Gomez

Dissertation submitted to the Faculty of the Graduate School of the
University of Maryland, College Park in partial fulfillment
of the requirements for the degree of
Doctor of Philosophy
2015

Advisory Committee:
Professor Alice Mignerey, Chair/Advisor
Professor Nicholas Hadley
Professor Millard Alexander
Professor Garyk Papoian
Professor Thomas Cohen

For Sarah and Mary

Acknowledgments

First and foremost I want to thank my advisor, Alice Mignerey. She has known me now for the better part of a decade. She has been there for me through success, failure, elation and heartbreak. Thank you Alice for all of the wisdom, patience, and in your own way, love, that you have shown me throughout the years. I have always appreciated our talks. I know I am an "acquired taste" but for as long as I have known you I have been able to talk to you about anything whether it was over the proverbial line or not. This has helped me grow as a scientist, and more importantly as a young(ish) man. I will never be able to repay you for flying me home on a two days notice from CERN so that I could be in DC with my great aunt in her final hours. Truly truly, thank you for being such a wonderful friend and colleague.

Next I would be remiss if I did not mention someone who has been there for me through nine years of a roller coaster ride. Sarah, there is no way at all I would be here without you. Writing this right now already brings tears to my eyes. You were the reason I even met Alice. You challenged me to be a better athlete, scholar, and man. Every word that comes to mind to even begin to thank you seems so cheap compared to how strongly I feel this thesis is earned by both of us. So many talks about how CMS management was driving me crazy. How you could probably come up and talk about tracking efficiency or directed flow better than many people even in my field... And all those times you had to just scratch my head and pick me up when I would stop believing in myself. You saved my life Sarah. This degree

is for you.

Alanna. Not much more needs to be said. My rock. The constant through all the storms in my life. Thank you for your guidance and patience these past years, specifically the last two or so. Im glad we have learned so much from one another and hope that as you enter graduate school again I can do as much for you as you did for me. I love you big sis!

Pollo and Macita (god rest). I am beyond thankful for all of the support that you guys have given. I am still heartbroken that Macita could not be here to celebrate with us but that is just what was in the cards. And Pollo, while you give me a lot of grief you and Alanna are easily the two people I am closest with in the family. You have listened to me ask you about religion, life, love and family and our talks have been really formative to create the man before you today (for better or worse). I love you Pollo.

Paul, thank you so much for the past 8 months. We have been fast friends and I have seldom been able to trust a person so quickly as you. You have been there for me as a reality check, a sanity check, someone to loosen me up if I am to tense, a protective shield if I am vulnerable and most importantly for me, an infinite source of joy. I cannot begin to tell you how much our friendship means to me, but I hope that I can provide for you an iota of what you have given me.

Cassie Taylor, thanks for being there for me right after I got back to College Park. Your advice of being gentle with myself has truly changed my life and I think gotten me back to a positive place much more quickly than I could have hoped for. You helped keep me sane these past few months and I thank you for your ardent

support through all of my life's troubles.

Katy, Lana and Dad. Thanks for supporting me through the years through all of my struggles both personal and professional. Lana, I owe much of my success from the examples you have set for me and my sisters through all these long years. Katy, I am glad that these past few years have brought a renaissance in our relationship and I hope we can continue to grow closer, thanks for your support and silly humor through all of this. Dad, thank you for all your talks and laughs. I am really glad that we have grown closer and I hope we can continue to do so moving forward, love you pops.

Tim, my brother. Thanks for all your support these past few years. We have been through the gamut together man. I wouldn't have made it without you. I hope you know that it means the world to me that we are still friends after having known each other for about half our lives now. Love you brother.

JoAnn, Greg, Dan, and Mike, more commonly known as the Muirs. You all have been so supportive of me through the years. All 12 of them! JoAnn thanks for being so open with me and in turn encouraging me to be open with others.

Andy and Ben Meyer, thank you guys for being so approachable and easy to talk to. And most certainly bridge buddies whenever I needed it the most.

Dr. Kolja "HERR" Kauder. Your thirst for life and knowledge has truly been an inspiration and a guiding light for me through all of the years that I have known you. Thanks for all the discussions about life, and sharing all of your stories with me. Thanks for the nights that I don't remember at "Little Joe's" playing darts with you and winding up in Wisconsin.

MT, and the rest of the Mignerey group. Thank you for keeping me smiling. MT thank you so much for holding my hand back in 2008 and helping me grow as a scientist. I am glad to have in any way shared your pains and joys over the past years.

To my colleagues, there are so so so many who helped me but to name a few: Michael Murray, Dave Hofman, Alan Bell, Gabor Veres, Christoff Roland, Matt Nyugen, Pat Kenny, Eric Appelt, Wei Li, Steve Sanders, thank you all so so so much.

A lot of love to my friends and colleagues back at UIC: Olga Evdokimov, Christine O'Brien and Yadav Pandit.

Perkins clan. I will never be able to thank you all enough. You know how much my current place in life was dependent on your taking me in at a very developmental time. Specifically to Danny, thanks for giving me a safe place to open up about things and be vulnerable.

Thanks to all of my other CP friends: Aaron Geller, Andrew Longhini, Chad Knipschild, Brian Calvert, Matt Murray, Zulya Tomova, Yi-Hsieh Wang, Zhiyue Lu, David Winogradoff.

Lastly, I wanted to mention the members of my "Victories" weekend group. Thank you all for truly saving me at a time when I was drowning. I would not be as close to sane as I am today without you all. Ian, Kristian, Terrence, Nat, Steve, Harold, Greg, Tim, Andy, Nate, Joel, Joe, David, Ray... I Love you all, my brothers.

Table of Contents

List of Tables ix

List of Figures x

List of Abbreviations xii

1 **Introduction** 1
- 1.1 **The Standard Model** . . . 1
  - 1.1.1 **Quantum Chromodynamics** . . . 3
- 1.2 **Heavy Ion Collisions** . . . 5
  - 1.2.1 **Event Characterization** . . . 6
- 1.3 **Azimuthal Anisotropy** . . . 8
  - 1.3.1 **Directed Flow** . . . 11

2 **Experimental Overview** 15
- 2.1 **The Large Hadron Collider** . . . 15
  - 2.1.1 **LHC Design** . . . 15
- 2.2 **Compact Muon Solenoid (CMS)** . . . 22
  - 2.2.1 **Forward Hadronic Calorimeter (HF)** . . . 26
  - 2.2.2 **Tracker** . . . 28
    - 2.2.2.1 **The Silicon Pixel Detector** . . . 30
    - 2.2.2.2 **The Silicon Strip Detector** . . . 31

3 **Tracking** 32
- 3.1 **Overview of Charged-Particle Reconstruction in the CMS Detector** . . . 32
  - 3.1.1 **Pixel and Strip Hit Reconstruction** . . . 34
  - 3.1.2 **Seed Generation, Pixel Tracking, and Pixel Vertexing** 40
  - 3.1.3 **Combinatorial Kalman Filter** . . . 42
- 3.2 **Charged-Particle Reconstruction in pp and pPb Collisions** . 44
  - 3.2.1 **Iterative Tracking** . . . 44
  - 3.2.2 **Primary Vertex Reconstruction** . . . 49
- 3.3 **Charged-Particle Reconstruction in PbPb Collisions** . . . 53

3.3.1 Primary Vertex Reconstruction . . . 57
3.3.2 First Iteration CKF Tracking . . . 59
3.3.3 Second Iteration Pixel Tracking . . . 59
3.3.4 Merging Procedure for Track Collections . . . 60

4 Analysis 61
4.1 Flow Theory and Analysis Techniques . . . 61
4.1.1 Event Plane Method . . . 61
4.2 Event Selection . . . 66
4.2.1 Trigger strategy and constraints . . . 67
4.2.2 Types of collisions and available L1 triggers . . . 69
4.2.3 Selecting minimum bias collisions . . . 71
4.2.3.1 Triggering . . . 71
4.2.3.2 Offline event selection . . . 72
4.2.3.3 Additional Offline Event Selection . . . 74
4.2.3.4 Vertex Position Cut . . . 76
4.2.4 Centrality Description . . . 78
4.2.5 Calculation of Centrality . . . 79
4.3 Track Selection . . . 79
4.4 Directed Flow Analysis . . . 81
4.4.1 v_1^{odd} . . . 81
4.4.2 v_1^{even} . . . 82

5 Systematics 83
5.1 Tracking Efficiency . . . 83
5.2 Event Plane Method Systematics . . . 86
5.2.1 Contribution of Fake Tracks . . . 86
5.2.2 EP Resolution . . . 90
5.2.3 Primary Vertex Position z± 5cm . . . 92
5.2.4 Primary Vertex Position z± 7cm . . . 95
5.2.5 $\rho\pm$ 0.09 cm . . . 97
5.3 Results . . . 101
5.3.1 $v_1^{odd}(\eta)$ . . . 101
5.3.1.1 Special Weights for HF Event Plane . . . 101
5.3.1.2 w/ Vertex Shifting Tests . . . 102
5.3.2 $v_1^{even}(p_T)$ . . . 109
5.4 Discussion . . . 114

List of Tables

3.1 **Track Seeding Parameters** 46
3.2 **Tracking Parameters** 48

4.1 The effects of various cuts on the data sample. % values are always with respect to to the line above (the cuts are applied in sequence). . 68
4.2 **Various track quality selection cuts for the full tracks (the cuts are applied in sequence).** 80
4.3 **Various track quality selection cuts for the pixel tracks (the cuts are applied in sequence).** 80

List of Figures

1.1 Generations of matter. . . . 2
1.2 Confinement. . . . 4
1.3 Asymptotic Freedom. . . . 5
1.4 Reaction Plane. . . . 7
1.5 Centrality. . . . 8
1.6 Correlation 9
1.7 v_2 Cartoon. . . . 10
1.8 v_1^{odd} cartoon. . . . 11
1.9 Published v_1^{odd} Results from PHOBOS and ALICE. . . . 12
1.10 v_1^{even} Cartoon. . . . 14

2.1 LHC layout. . . . 16
2.2 LHC Components. . . . 18
2.3 Integrated Luminosity. . . . 21
2.4 CMS[44]. . . . 23
2.5 CMS Slice. . . . 25
2.6 θ and η in High Energy Physics. . . . 26
2.7 HF. . . . 28
2.8 Schematic of the CMS Tracker. . . . 30
2.9 CMS Pixel Tracker. . . . 31

3.1 Strip RecHits. . . . 35
3.2 PixelCluster. . . . 37
3.3 HIEvent. . . . 54
3.4 TrackerOccupancy. . . . 56

4.1 Event Plane Flattening Example 64
4.2 Centrality Distribution 67
4.3 Pixel Multiplicity vs. HF Energy 73
4.4 PKAM Event Examples 75
4.5 η Asymmetry 77
4.6 Primary vertex location along z 78

5.1 Track Stats for 2011 MinBias Data Set . . . 84
5.2 Tracking efficiency as functions of η and p_T for the new "hiGeneralAndPixelTracks" in the 2011 dataset. . . . 85
5.3 Fake rate as functions of η and p_T for the new "hiGeneralAndPixelTracks" in the 2011 dataset. . . . 86
5.4 $v_1(\eta)$ contribution from fake tracks . . . 87
5.5 $v_1(p_T)$ contribution from fake tracks . . . 89
5.6 HF EP Resolution . . . 90
5.7 Tracker EP Resolution . . . 91
5.8 $v_1^{odd}(\eta)\,|z| < 5cm.$ . . . 93
5.9 $v_1^{even}(p_T)\,|z| < 5cm.$ . . . 94
5.10 $v_1^{odd}(\eta)\,|z| < 7cm.$ . . . 95
5.11 $v_1^{even}(p_T)\,|z| < 7cm.$ . . . 96
5.12 $v_1^{odd}(\eta)\,\rho > 0.09cm.$ . . . 98
5.13 $v_1^{even}(p_T)\,\rho < 0.09cm.$ . . . 99
5.14 $v_1^{even}(p_T)\,\rho > 0.09cm.$ . . . 100
5.15 Standard v_1^{odd} with HF versus modified EP weights . . . 102
5.16 Standard v_1^{odd} with HF versus modified EP weights $|z| < 5cm$ . . . 103
5.17 Standard v_1^{odd} with HF versus modified EP weights $|z| < 7cm$ . . . 104
5.18 $v_1^{odd}(\eta)$ w/ fit and errors . . . 106
5.19 Magnitude of $v_1^{odd}(\eta)$ versus centrality. . . . 107
5.20 $v_1^{odd}(\eta)$ in 2010 versus 2011/ . . . 108
5.21 $v_1^{even}(p_T)$ using the Tracker EP, 2010 vs. 2011 . . . 111
5.22 $v_1^{even}(p_T)$ using the Tracker EP in 2011 . . . 112
5.23 $v_1^{even}(p_T)$ CMS(EP) vs. ATLAS2 . . . 113
5.24 Standard EP resolution for HF with different Vertex Position Cuts . . . 114
5.25 ALICE $v_1^{odd}(\eta)$ . . . 116
5.26 v_1^{odd} from NA49 . . . 117
5.27 $v_1^{odd}(\eta)$ STAR versus centrality . . . 118
5.28 ALICE cartoon of Participant versus Spectator Planes . . . 119
5.29 $v_1^{odd}(\eta)$ from STAR using various methods . . . 120
5.30 $v_1^{even}(p_T)$ measurement from ALICE . . . 121
5.31 $v_1^{odd}(y)$ of identified particles from STAR . . . 122

List of Abbreviations

γ	A photon
e	Units of electron charge
e^-	Electron
e^+	Positron
μ^-	Muon
μ^+	Anti-Muon
τ^-	Tau particle
τ^+	Anti-Tau
EM	Electromagnetism/Electromagnetic
SM	Standard Model
u	Up quark
d	Down quark
c	Charm quark
s	Strange quark
t	Top quark
b	Bottom quark or the Impact parameter
QCD	Quantum Chromodynamics
QED	Quantum Electrodynamics
LHC	Large Hadron Collider
CERN	European Center for Nuclear Research
ALICE	A Large Ion Collider Experiment
ATLAS	A Toroidal LHC Apparatus
CMS	Compact Muon Solenoid
PS	Proton Synchrotron
SPS	Super Proton Synchrotron
IP	Interaction Point
IBS	Intrabeam Scattering
LEIR	Low Energy Ion Ring
QGP	Quark Gluon Plasma
ECAL	Electromagnetic Calorimeter
HF	Forward Hadronic Calorimeter

QGP	Quark Gluon Plasma
HI	Heavy Ion
RP	Reaction Plane Angle
p_T	Transverse Momentum
v_2	Elliptic Flow
RHIC	Relativistic Heavy Ion Collider
v_1	Directed Flow
EP	Event Plane
R	Resolution Correction Factor
cm	Centimeters
CMSSW	CMS Software
L1	Level-1 Trigger
Hz	Hertz
HLT	High Level Trigger
UPC	Ultra Peripheral Collision
BSC	Beam Scintillator Counters
ZDC	Zero Degree Calorimeter
PKAM	Previously Known As Monster events
TIB	Tracker Inner Barrel
TOB	Tracker Outer Barrel
TID	Tracker Inner Disc
TEC	Tracker Endcap
HIP	Highly-Ionizing Particle
CKF	Combinatorial Kalman Filter

Chapter 1: **Introduction**

1.1 The Standard Model

In our current understanding of the world there are four fundamental forces, gravity, electomagnetism (EM), and the strong and weak forces. The strong, weak, and EM interactions are understood as exchanges of various spin-one bosons amongst spin-half particles that make up matter. The Standard Model(SM) is composed of particles that arise from excitations of the different fields and force carriers that mediate the interaction between those particles.

Elementary particles can be classified by their intrisic properties like their mass and charge, but also by their quantum properties like color or flavor. Spin, perhaps the most famous of the quantum properties, is an intrisic property that adds an extra degree of freedom to the set of quantum numbers. Spin-1/2 particles are known as fermions. In the SM, fermions can be either leptons or quarks. Leptons and quarks both are broken into three generations. There are six known types of quarks with the different species being known colloquially as "flavors". These different flavors shown in Figure 1.1, they are: up (u), down (d), charm (c), strange (s), top (t), and bottom (b). The leptons are: electron (e), muon(μ), tau(τ) as well as the three neutrinos (ν_l, ν_m, ν_h), which stand for light, medium, and heavy

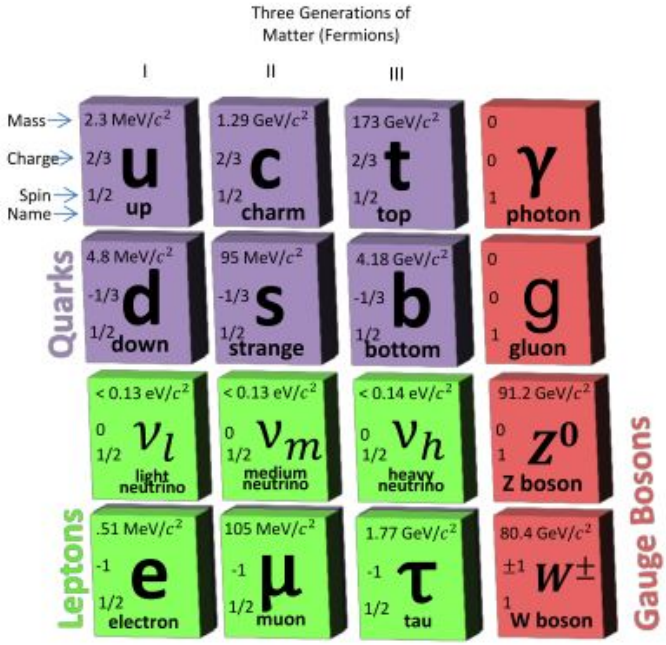

Figure 1.1: The three generations of matter in the standard model. The Higgs boson has been omitted from this due to lack of relevance.

respectively. Previously it was thought that neutrinos were strictly electron, muon and tau neutrinos but recent evidence points towards the three states all being linear combinations of the different quark types. All of the particles mentioned have their associated antiparticle, which is identical in every way but the charges (both color and electric) are flipped. If a quark is usually denoted q, its antiquark would be denoted $\overline{q}$, and a lepton denoted e^- and the antiparticle would be e^+. The spin-1 particles that are included in the SM are the force mediators. The photon (γ) mediates the EM interaction; the $W^{\pm}$ and Z^0 bosons mediate the weak force; while the gluon (g) mediates the strong force.

1.1.1 Quantum Chromodynamics

The current understanding of the strong force in the SM is the theory of *Quantum Chromodynamics* (QCD). This theory attempts to describe the interactions between quarks and gluons. The theory itself borrows heavily from the more well known theory, *Quantum Electrodynamics* (QED). Like electric charge in QED, QCD has a property called color charge. Unlike in QED however, where the force mediator has no charge within the corresponding field, in QCD the gluons themselves carry color just like the quarks. These three color charges are red, blue and green, with the corresponding antiquark charges of antired, antiblue and antigreen.

A feature of QCD (and other non-Abelian theories) is the correlation between the strength of the interaction and the distance scales. In QCD this manifests itself in two of the theories more notable and bizarre properties: confinement and asymptotic freedom.

Confinement means that the quarks (and gluons) themselves can never be seen in nature outside of a bound state, thus the name confinement. Everything we see in nature is a color neutral particle; this color neutrality gives rise to two different classes of particles. *Mesons* are made up of a quark, antiquark pair ($q\overline{q}$). There are also *baryons* , particles made up of three valence quarks; a red, a green, and a blue quark combine to give us the familiar protons and neutrons. The confinement phenomena is most easily thought about with an analogy of a spring. Imagine a $q\overline{q}$ pair sitting near each other in a bound state connected by a gluon (the spring). When you try to pull the two quarks apart you are storing potential energy in that

spring. As you keep "stretching" now there is enough energy in the spring to start creating particles in the form of a new $q\overline{q}$ pair and they are emitted in all directions coming from the spring. Eventually, if the quarks are separated enough a "color-flux" tube is created where this is thought of as a cylindrical tube of connected gluons that are holding all of the potential energy that you imparted on the system to separate the quarks. Pull just a bit farther and the tube "snaps" and what you are left with is a large shower of particles emitted in all directions, and two of those created particles will be a q and a $\overline{q}$ that become paired with the original $\overline{q}$ and q respectively, thus yielding two "new" color neutral particles.

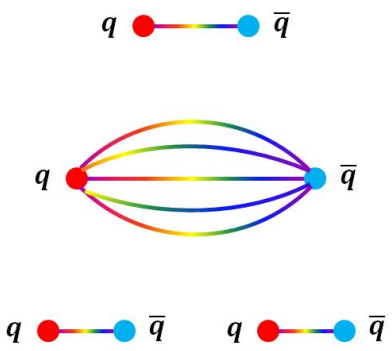

Figure 1.2: A cartoon depicting the process of trying to separate two paired quarks and the resulting two mesons.

Asymptotic freedom looks at strong interactions that happen in the reversed scenario. If we limit ourselves to focus on the very short range interactions, the strength of the strong force is lessened. At asymptotically high energies the quarks and gluons behave and can be probed as if there were free like in the right panel of Figure 1.3. Studying this state is the goal of the work of the Large Hadron Collider

(LHC) heavy ion program and the Relativistic Heavy Ion Collider (RHIC).

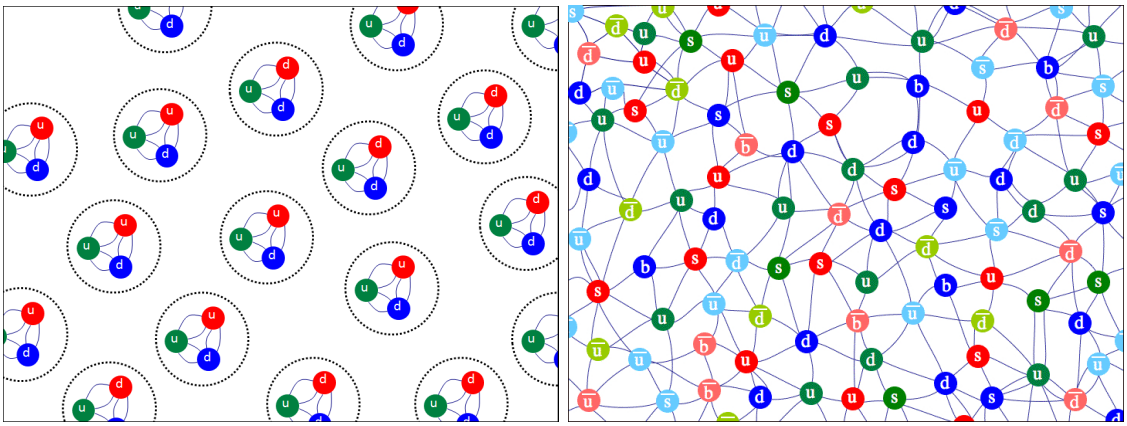

(a) (b)

Figure 1.3: A cartoon depicting confined quarks in normal matter (a) and deconfined quarks in the QGP produced in Heavy Ion collisions (b). Adapted from [41]

1.2 Heavy Ion Collisions

At the LHC researchers from around the world are now afforded the opportunity to study matter in extreme environments using a machine that, for Heavy Ions, can produce collisions of up to almost 28 times the previously highest achieved energy of 200 GeV, from the Relativistic Heavy Ion Collider (RHIC) at Brookhaven National Labs (BNL). In collisions of heavy ions at these energies, it is expected that the high temperatures and energy densities created produce systems in the asymptotic freedom regime and a new phase of nuclear matter is created called the *Quark Gluon Plasma* (QGP). This state of matter is created by an increase in parton (quarks and gluons) density, so great that the hadronic "borders" become blurred

and quarks become *deconfined* from their hadronic state and become free to move around and interact. The before and after effect are depicted in (a) and (b) of Fig 1.3, respectively.

Some of the specific measurements that describe the bulk properties of the medium are: charged particle multiplicity, transverse momentum (p_T) spectra of produced particles, particle species ratios and anisotropic flow. These measurements help determine the degree of thermalization and energy densities achieved in this medium.

1.2.1 Event Characterization

The magnets at the LHC are strong enough to steer the ions to collide with one another, but particularly in Heavy Ion (HI) collisions, where $A > 1$, the nucleus has a characteristic size to it and this leads to different types of collisions. Just as in the Rutherford Scattering problem, the impact parameter (b) is the line that connects the center of masses of the two colliding nuclei. The plane along the direction of the impact parameter is called the Reaction Plane (RP). Cleverly enough, the azimuthal orientation of the impact parameter with respect to the lab frame is called the RP angle. The RP angle cannot be experimentally measured, but can be approximated using methods described in Section 4.1.

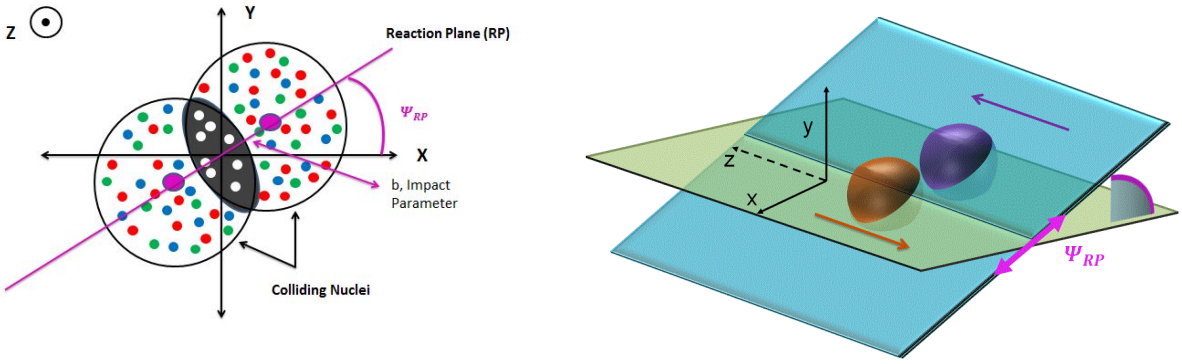

(a) (b)

Figure 1.4: Panel (a) shows a two dimensional cartoon of a collision between two nuclei from the perspective of looking down the beam axis (Z). Panel (b) shows a three dimensional cartoon of the whole Reaction Plane colored blue for emphasis.

Another important way to characterize an event is the $|b|$. The magnitude of the impact parameter is loosely related to what is called the event *centrality*. If b is shorter, that means that the two nuclei have a greater amount of overlap, this is called a central collision. As the magnitude of b increases the event is more and more what is colloquially called a "peripheral event". Of course it is not a binary designation, depending who you ask the terms: "central", "mid-central", "mid-peripheral" and "peripheral" all can be different values of centrality. Visual representations of different centrality classes can be found in Fig. 1.5. What is done in practice is to measure the number of particles produced in a collision. In an event where there is a higher degree of nuclear overlap, there will be a higher particle

multiplicity. The actual value of centrality is given as the percent of collisions having a higher particle multiplicity than the current event. So if an event has a centrality of 10%, then 10% of events will have created more particles than the event we are looking at. An important thing to note is that a given value of centrality is determined by observables, and does not correspond to a linear extrapolation of b. That is to say, a collision with a centrality of 50% does not have an impact parameter whose length is twice the magnitude of an event with a centrality of 25%.

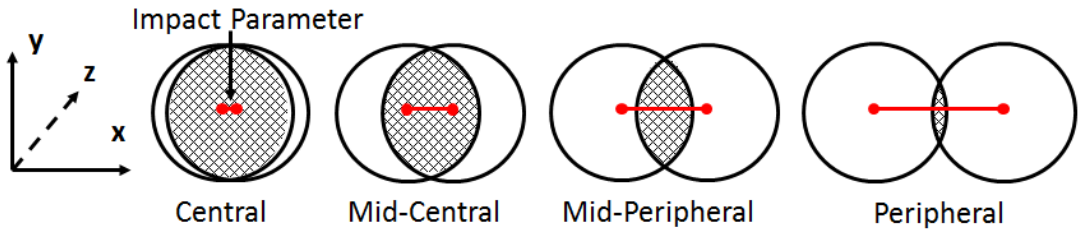

Figure 1.5: A cartoon showing different centrality classes and how it relates to percent overlap of the two nuclei. [41]

1.3 Azimuthal Anisotropy

One of the most interesting properties of the collision that is measured is anisotropic flow. Flow is defined as the azimuthal anisotropy measured with respect to the RP that was illustrated in Fig.1.4, but shown more explicitly shown in Fig 1.6. Flow is quantified by the Fourier coefficients (see Equation 1.1) of the azimuthal

distribution of the particles produced in a HI collision.

$$\frac{dN}{d\left(\phi - \Psi_R\right)} = \frac{1}{2\pi}\left(1 + \sum_{n=1}^{\infty} 2v_n \cos\left(n\left(\phi - \Psi_R\right)\right)\right) \tag{1.1}$$

The second order coefficient (v_2) is called "Elliptic Flow" and has been studied extensively at both the LHC and the Relativistic Heavy on Collider (RHIC). The first order Fourier coefficient, v_1 is called the "Directed Flow", and will be the focus of this thesis.

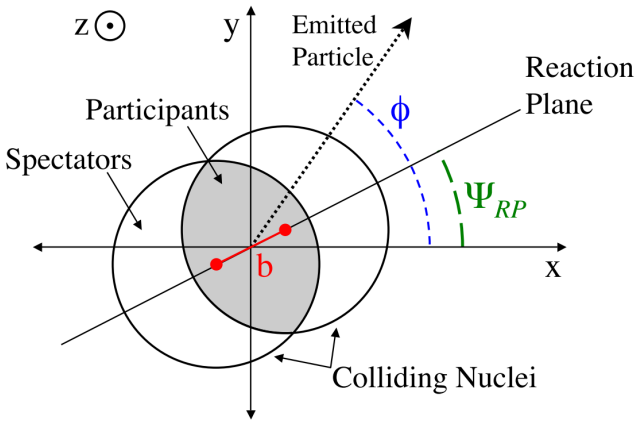

Figure 1.6: A diagram showing how a particle emitted at an azimuthal angle ϕ, may be correlated to the Reaction Plane angle denoted Ψ_{RP} .

The flow signal is generated from the initial spatial anisotropy of the overlapping region of non-central collisions. With significant interactions of the produced particles in this region, pressure gradients form, resulting in the particles streaming out in greater numbers and with a higher momentum in the direction of the RP, as illustrated in Fig. 1.7. Since the produced particles must interact with themselves to generate a signal, flow measurements provide information on the degree

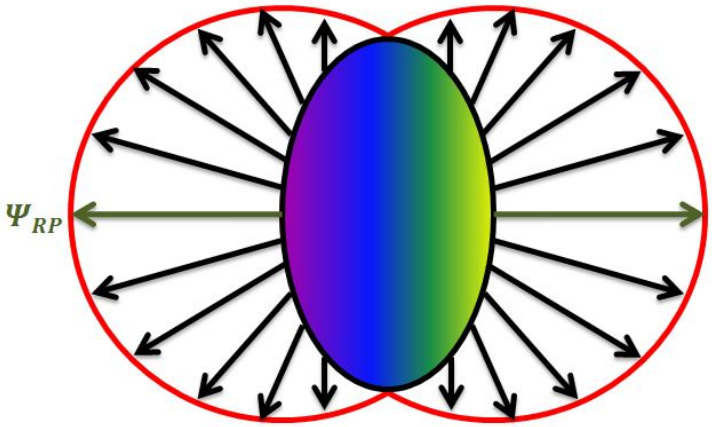

Figure 1.7: A cartoon representing the pressure gradients and the resulting anisotropy from the energetic medium formed in Heavy Ion collisions. Adapted from [41]

of thermalization of the source. Also, since the anisotropy becomes symmetric as the source expands due to the symmetry in the pressure gradients, a flow signal necessarily provides information on the very early times of the collision when the energy density is largest.

If the medium was strongly interacting, the gradient will be steepest along the direction of the RP (indicated in Fig. 1.7 by the green line), than orthogonal to it (long axis). If the medium was a weakly interacting plasma, as was expected in the late 1990's before the first RHIC data, the flow signal would be near zero with very little particle asymmetry. What has been seen however is a strong asymmetry. This indicated that the medium was strongly interacting and thermalized quickly. Additionally, the azimuthal distribution of lower p_T particles, which are the majority of the particles produced, was consistent with low viscosity hydrodynamic models.

1.3.1 Directed Flow

The first Fourier coefficient of the produced particle anisotropy has been measured since the very early days at AGS [46] with the E917 and E895 experiments and also at the CERN SPS with the NA experiments. These studies have since been further expanded on by the PHOBOS [13] and STAR [9, 10, 7, 11, 5] collaborations at RHIC, and the ATLAS [3] and ALICE [4] experiments at the LHC. This thesis, will present the first CMS Directed Flow measurement.

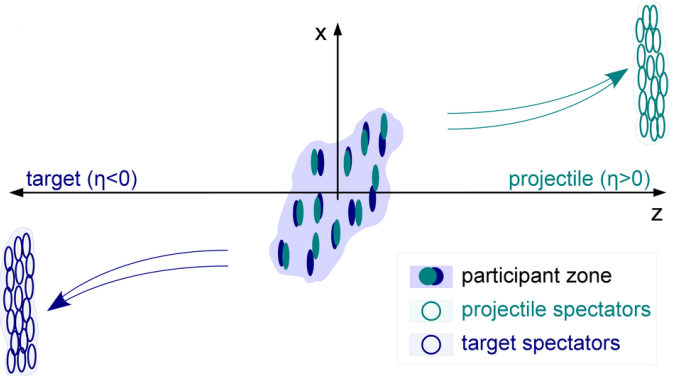

Figure 1.8: [4]

Directed flow is particularly sensitive to the initial conditions of the medium. The odd component of v_1 ($v_1(\eta) = -v_1(-\eta)$) is thought to stem from the deflection of the spectator matter at high pseudorapidity, as seen in Fig. 1.8. Near mid-rapidity v_1^{odd} approaches zero very quickly as the deflection anisotropy is very small, this is seen in all panels of Figure 1.9. With higher beam energy there seems to be smaller deflection perpendicular to the beam.

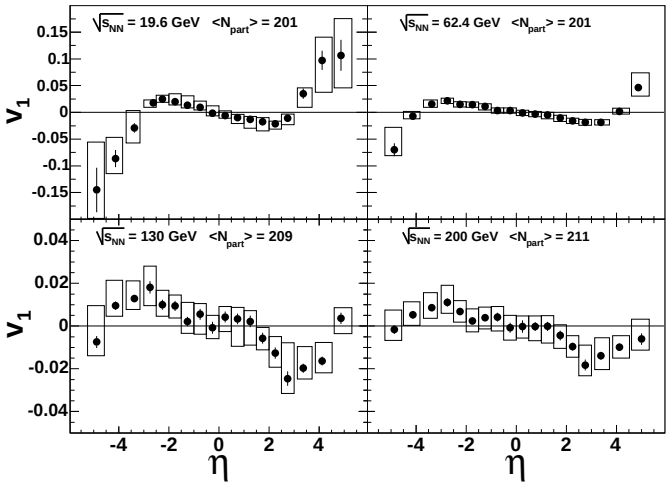

(a)

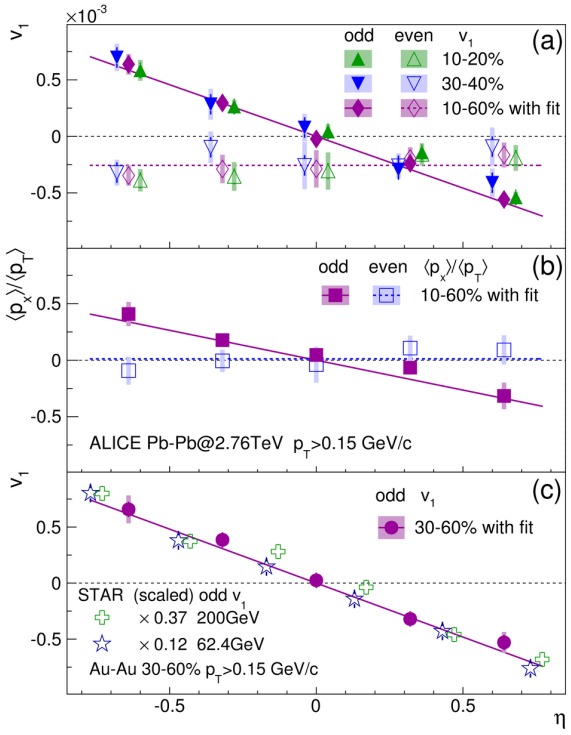

(b)

Figure 1.9: (a) shows the results of a PHOBOS directed flow measurement [13]. This is what is traditionally known as v_1^{odd}, while (b) shows the results of a directed flow measurement made by the ALICE collaboration [4] . Note the difference in scale on the y-axis.

The rapidity even component of directed flow (v_1^{even}) ($v_1(\eta) = v_1(-\eta)$) is thought to be sensitive to the "clumpyness" of the medium. That is to say if the created fireball does not have a uniform temperature or energy density, the result will be a v_1^{even} signal. The non-uniformity is depicted in the cartoons in Figure 1.10. This can be thought of as protons and neutrons having an asymmetric distribution of energy and quarks inside of them which v_1^{even} tries to statistically probe. Both the even and odd components of directed flow have been measured with respect to pesudorapidity, rapidity (for identified hadrons), and p_T.

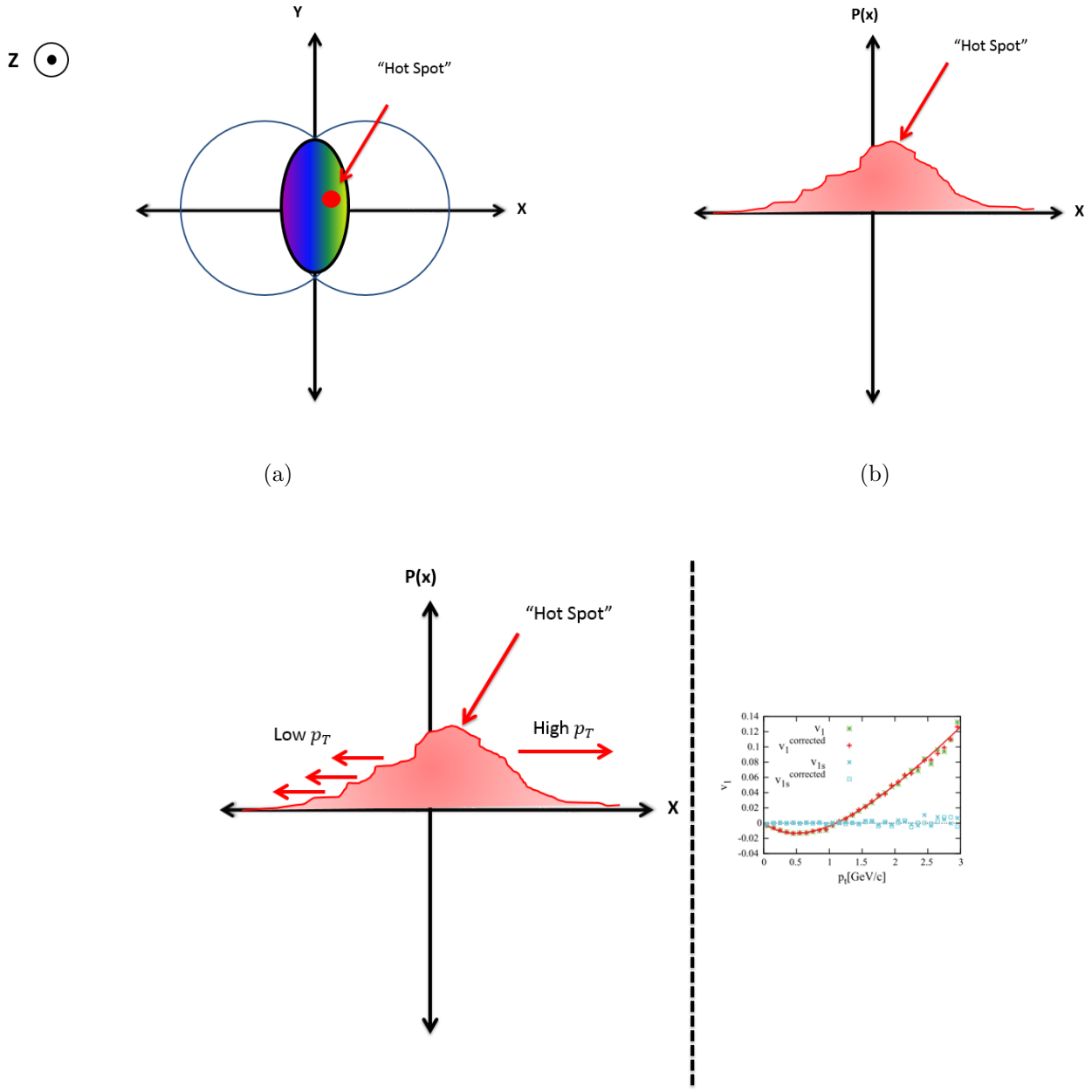

(a) (b)

(c)

Figure 1.10: A cartoon representing what a deviation of isotropic energy distribution would look like spatially (a), in pressure space (b) and a cartoon relating the v_1^{even} behavior of high and low-p_T particles [34] to the pressure picture (c).

Chapter 2: **Experimental Overview**

2.1 The Large Hadron Collider

The Large Hadron Collider (LHC) is a particle accelerator located at the European Center for Nuclear Research (CERN). The accelerator has an approximate circumference of 27 km and a particle in the accelerator will have its passport stamped four times as it crosses between Switzerland and France. The LHC itself is actually two adjacent synchrotrons that circulate the beams in opposite directions. Using over 9000 magnets, the LHC forces the beams to overlap at four different locations, and it is at these locations that the four biggest experiments of the LHC are located. These experiments are, ***A*** ***L***arge ***I***on ***C***ollider ***E***xperiment (ALICE), ***A*** ***T***oroidal ***L***HC ***A***pparatu***S*** (ATLAS), ***C***ompact ***M***uon ***S***olenoid (CMS), and LHC-b. The layout of the LHC with the location of these experiments indicated is shown in Fig. 2.1

2.1.1 LHC Design

The LHC is actually made up of several different components that ionize, store, and ramp up the energy of the beams. The LHC was originally designed as a

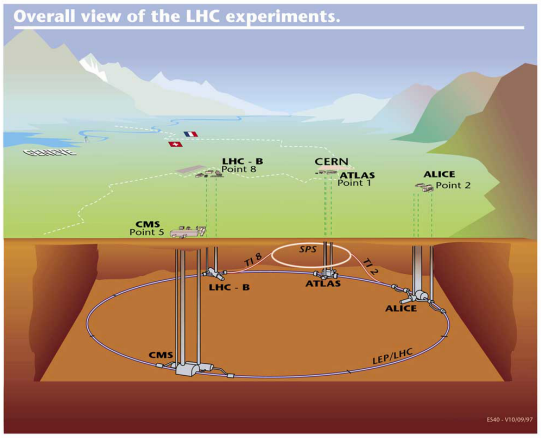

Figure 2.1: Cartoon depicting the placement of the various experiments at the LHC[22].

proton-proton collider. The protons (and Pb ions) are accelerated along the beam axis (z), and grouped into bunches along that axis by radio frequency (RF) cavities. The bunches are then steered in a circular orbit and focused by the magnets inside the LHC.

Accelerating the particles requires several intermediate accelerators. The Lorentz force equation, $\vec{F} = q\vec{v} \times \vec{B}$, where q is the charge of the particle, $\vec{v}$ is the velocity of the particle and $\vec{B}$ is the magnetic field. This equation can be used to determine the strength of the magnetic field required to contain particles of a given velocity within the radius of each accelerator in the ramp up process. As the kinetic energy of the particles increases within one accelerator in the chain, the magnetic field produced by the magnets increases in order to compensate. The maximum energy a particle can reach in a given accelerator is determined by the accelerator's radius. Once the particles reach the maximum energy within their current accelerator they are injected into the next accelerator in the chain. The particles finally reach their

energy of 3.5 TeV(for protons) or 1.38 (for the fully stripped Pb Ions), note that these energies are for Run 1 (2009-2013).

The various components of the acceleration process are shown in Fig. 2.2. In proton-proton running, the duoplasmatron ionizes the hydrogen gas by using electron cathodes. The protons are then accelerated through charged grids in order to focus the plasma into a beam using quadrapole magnets. Protons leave the duoplasmatron with an energy of 100 keV. The Linac 2 then increases the proton energy using voltage differentials applied via alternating current. Since the alternating current would ordinarily result in no net gain in the energy of the proton, the sections of the Linac 2 that would cause the protons to accelerate backwards are shielded. Protons leave the Linac 2 at about 50 MeV.

The proton synchrotron booster, proton synchrotron (PS) and super proton synchrotron (SPS) accelerate and bunch the protons using the RF standing waves. Similar to the Linac 2, the standing waves yield both positive and negative acceleration. However, here the protons are not shielded from the portion of the wave that causes negative acceleration which allows the protons to bunch. The booster injects protons into the PS with 1.4 GeV of energy, the PS inject protons into the SPS with 25 GeV of energy, and the SPS injects protons into the LHC with 450 GeV of energy. The total injection time takes about 16 minutes.

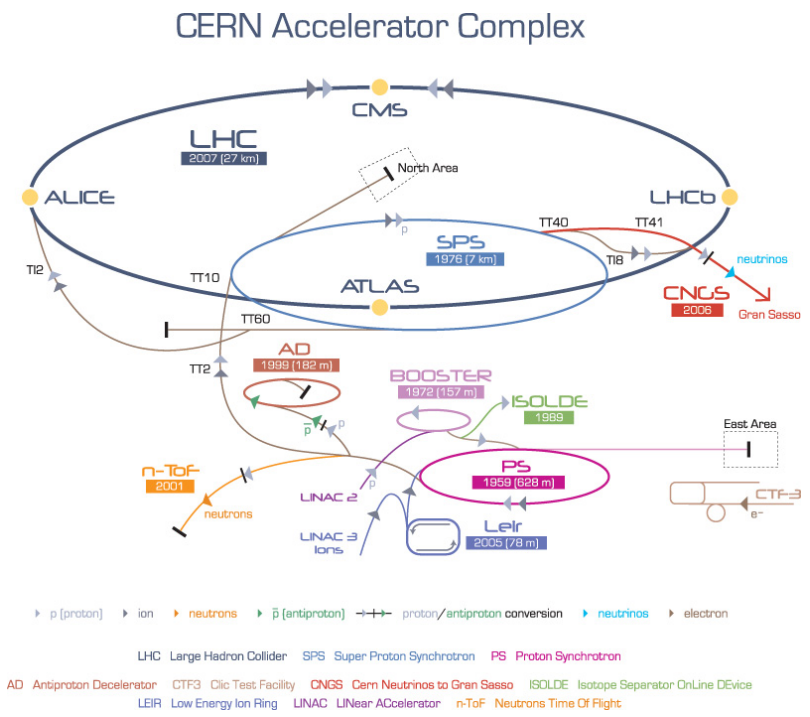

Figure 2.2: The various components and experiments at the LHC.

LHC Parameters

For proton-proton collisions the nominal center-of-mass energy is $\sqrt{s_{NN}}$=14 TeV. For other nuclear species the energy scales with Z/A, where Z and A are the nuclear proton and mass numbers, respectively. In the case of lead-lead (PbPb) collisions, we use $Z = 82, A = 208$ which can be collided at a maximum energy of $\sqrt{s_{NN}}$=5.5 TeV. The event rate generated in the LHC is given by Equation 2.1:

$$\frac{dN}{dt} = L\sigma_{process}, \tag{2.1}$$

where $\sigma_{process}$ is the cross section for the process in the study and L is the machine luminosity. The luminosity depends only on the beam parameters and is

$$L = \frac{N_b^2 n_b f_{rev} \gamma}{4\pi \epsilon_n \beta^\star} F. \tag{2.2}$$

For a Gaussian beam distribution, N_b is the number of particles per bunch, n_b is the number of bunches per beam [16], f_{rev} is the revolution frequency, γ is the lorentz factor, and the parameters $\epsilon_n, \beta^\star$, and F are related to the design of the accelerator and the angles of the beams at the interaction point (IP) at the detector.

The luminosity lifetime is not constant over a physics run. It decays due to degradation of intensities. The main cause of this is from collisions. The initial decay time of bunch intensity due to this effect is:

$$\tau_{nuclear} = \frac{N_{initial}}{L \sigma_{tot} k}, \tag{2.3}$$

where $N_{initial}$ is the initial beam intensity, L is the initial luminosity, σ_{tot} is the total cross section and k is the number of interaction points. If we assume an initial peak luminosity of $L = 10^{-34}$ cm^{-2}s^{-1} , Eq. 2.3 yields an initial decay time of τ of about 45 hrs. Other effects can decrease the luminosity in a given run, including intrabeam scattering (IBS) and residual beam gas scattering. Putting this all together gives an expected luminosity lifetime of:

$$\tau_L = \frac{1}{\tau_{Nuclear}} + \frac{1}{\tau_{IBS}} + \frac{1}{\tau_{beamgas}}. \tag{2.4}$$

The beam intensity and luminosity can also be written as functions of time (t):

$$N(t) = \frac{N_{initial}}{1 + \frac{t}{\tau_{nuclear}}} \tag{2.5}$$

$$L(t) = \frac{L_0}{\left(1 + \frac{t}{\tau_{nuclear}}\right)^2}. \tag{2.6}$$

The amount of data that an experiment collects is given by the integrated luminosity (Eq. 2.7)

$$L_{int} = L_0 \tau_L \left(1 - e^{\frac{-T_{run}}{\tau_L}}\right). \tag{2.7}$$

In 2011 CMS was able to record 157.57 μb^{-1} of data. Figure 2.3 is a plot of the total luminosity delivered by the LHC and the luminosity that was recorded by CMS, and shows that CMS was over 94 percent efficient.

Colliding Ions

Once a year the LHC changes the beam configuration to allow for about one month of Heavy Ion collisions. Through the winter 2013 the dipole magnets at the LHC were operating at half the designed field, achieving a center-of-mass energy of $\sqrt{s_{NN}} = 2.76$ TeV for symmetric PbPb collisions.

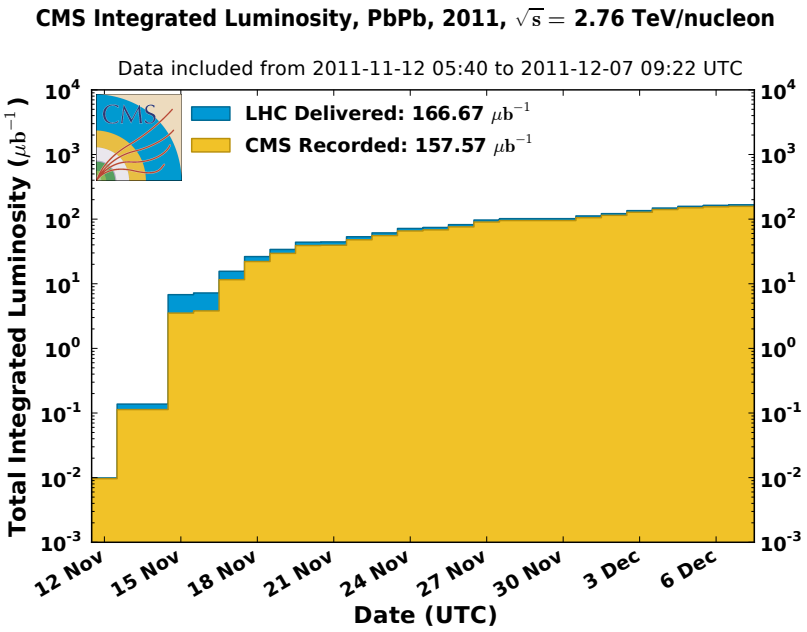

Figure 2.3: Integrated Luminosity for 2011.

The lead ions are produced from a highly purified lead sample that is heated to 550° C. Charge states up to Pb^{+27} are selected and accelerated to 4.2 $\frac{MeV}{nucleon}$ by the Linear Accelerator (Linac 3) before passing through a carbon foil, which strips more electrons from most of the ions to Pb^{+54}. The Pb^{+54} beam is accumulated, then accelerated to $72\frac{MeV}{nucleaon}$ in the Low Energy Ion Ring (LEIR). Then, the ions are transfered to the PS and accelerated to 5.9 $\frac{GeV}{nucleon}$ where they are then injected into the SPS after first passing through another foil where the ions become fully stripped to Pb^{+82}. The SPS accelerates the ions to $177\frac{GeV}{nucleon}$ and then injects them into the LHC where they reach the energy of $1.38\frac{TeV}{nucleon}$.

2.2 Compact Muon Solenoid (CMS)

CMS is one of the four experiments at the LHC and one of the two multi-purpose "discovery" experiments. In proton-proton running one of the main areas of interest was to study the potential (and now confirmed) existence of one or more species of Higgs bosons [24]. For the Heavy Ion program the focus is to study the state of strongly-interacting matter called the Quark Gluon Plasma at some of the highest energy densities ever reached in the laboratory. In order to achieve all of its physics goals CMS needed:

- a high performance system to detect muons,
- a high resolution method to detect and measure electrons and photons (ECAL)
- a high quality central tracking system to give accurate momentum measurements, and
- a "hermetic" hadron calorimeter, designed to entirely surround the collision point and prevent particles from escaping

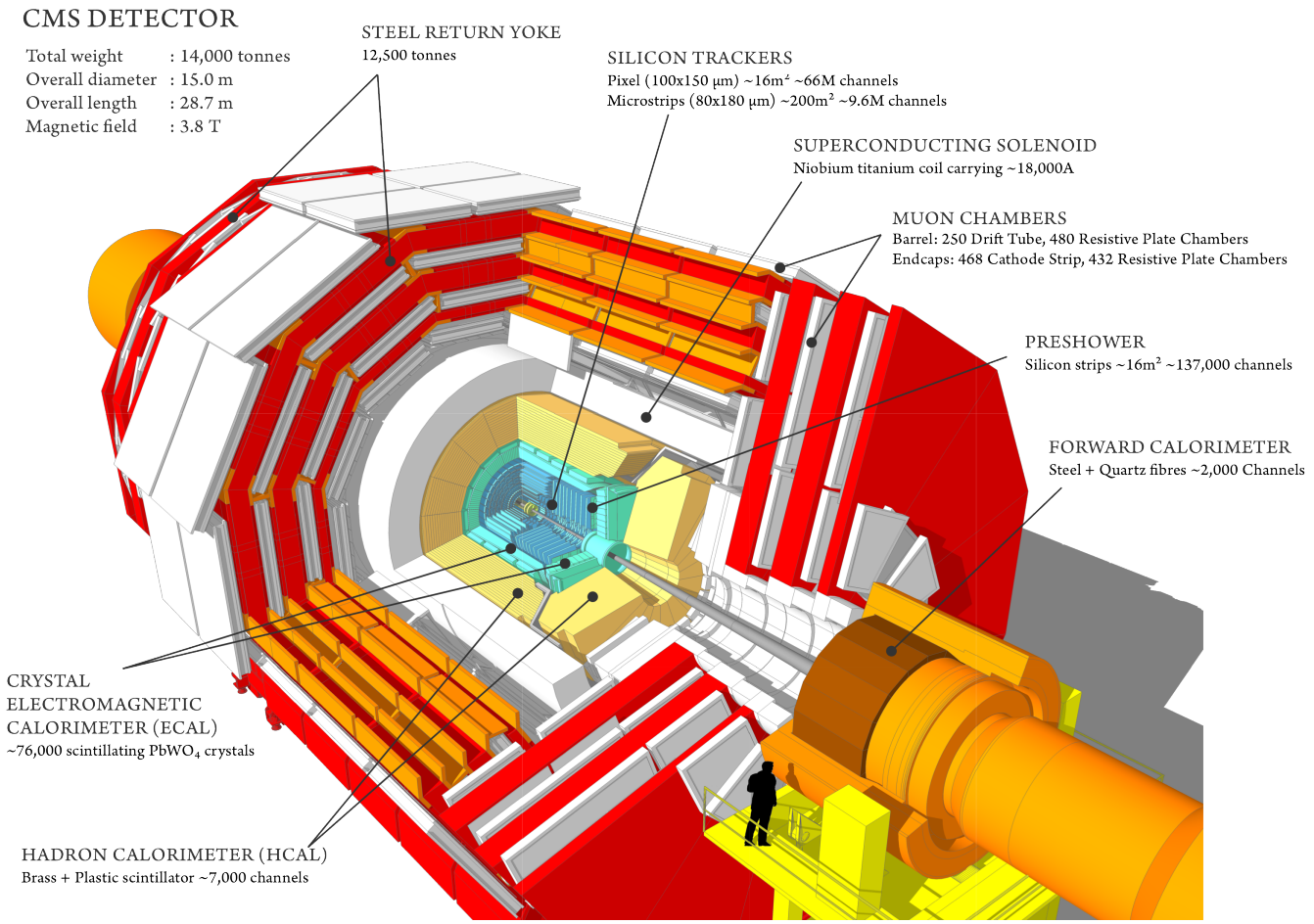

Figure 2.4: CMS.

CMS itself is 20 meters long and 14 meters in height and width. There are several different kinds of sub-detectors in CMS that provide different kinds of information about the particles as they pass through the detector. There are the tracking systems that record the passage of charged particles through layers of silicon strips and pads by measuring the ionization in the detector, termed "hits". These tracking detectors provide the particle's momentum by analyzing its radius of curvature as it propagates through the 3.8 Tesla magnetic field produced by the solenoid. The calorimeters are energy detectors of which there are two types EM and HAD calorimeters. The EM calorimeters use crystals made of lead tungstate ($PbWO_4$), and the HAD calorimeters use layers of brass or steel interlaced with quartz fibers. A particle will interact with these layers and create a shower. The energy of the shower is measured using photo-multiplier tubes and the total amount of energy collected for a specific channel can be determined. A transverse picture of CMS is shown in Fig. 2.5. The inner most ring shows the silicon tracking system which is used in this analysis and described in Section 2.2.2, the thin green layer just beyond is the Electromagnetic Calorimeter (ECAL). Just beyond the thick yellow layer is the Hadronic Calorimeter (HCAL), a part of which is also used in this analysis and whose description can be found in Section 2.2.1, and the far right part of the image shows the muon chambers and the return yolk. The cartoon also illustrates various particle species and the way they interact as they move through various levels of CMS.

In CMS a system of cylindrical coordinates is used with the beam direction serving as the z axis, and the r-ϕ (transverse) plane being perpendicular to it. In

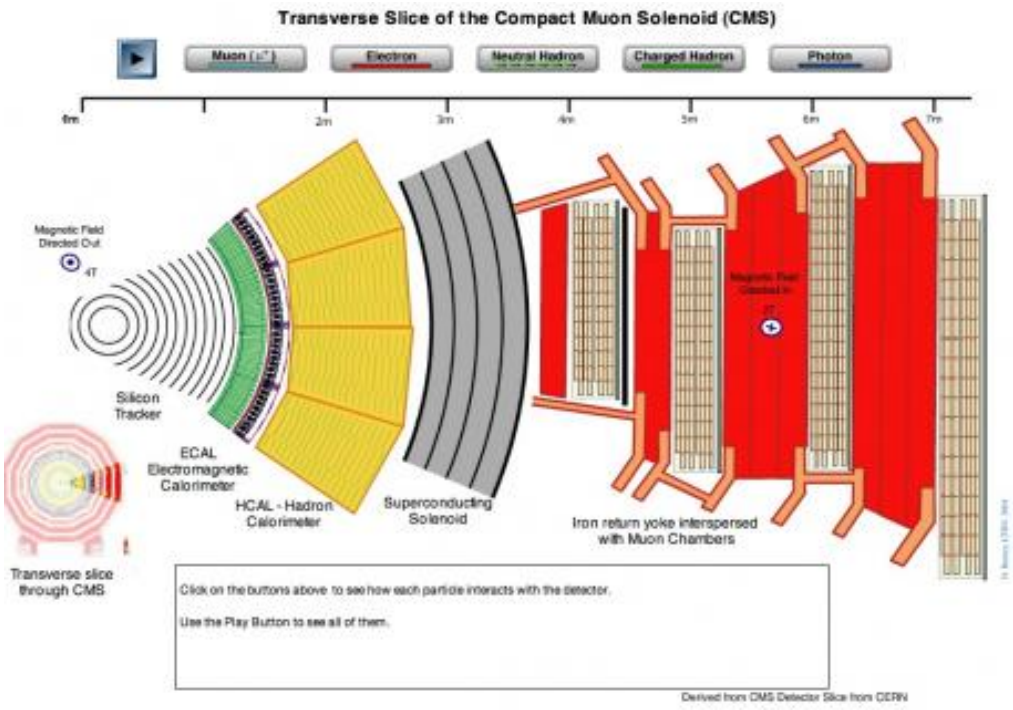

Figure 2.5: CMS Slice [14].

high energy physics it is common to use pseudorapidity denoted as η. It is empirically defined as $\eta = -ln\left[tan\left(\frac{\theta}{2}\right)\right]$. As its name suggests it is an approximation of the variable rapidity, which is given by $y = \frac{1}{2}ln\left(\frac{E+p_z}{E-pZ}\right)$. The distribution of particles in rapidity space is nearly flat, while in pseudorapidity space, only low mass particles are distributed evenly. In experiment a particle's momentum can be measured but its energy can only be sampled because we cannot know the total energy without knowing the particles identity. Because of this, rapidity is not a useful variable in current analysis. Psuedorapidity on the other hand can be discerned knowing only the particles angle of declination denoted θ. Pseudorapidity relies on the approximation that the particle in question is massless. As the particle becomes more and more massive, more energy from the beam needs to be used in

order to create it, reducing its boost in the z direction. Also, for very high energies the particle mass is less important so the approximation of y$\rightarrow \eta$ gets better.

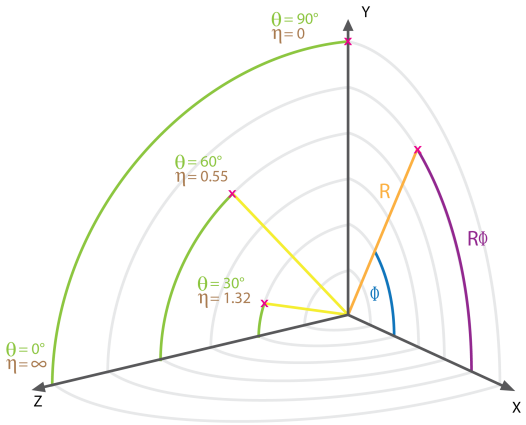

Figure 2.6: Simple picture showing the coordinate system used by High Energy physics [37].

2.2.1 Forward Hadronic Calorimeter (HF)

In order to measure more energetic particles including hadrons, a hermetic sampling calorimeter was designed. A sampling calorimeter is a kind of detector that has alternating layers of plastic scintillator or Cherenkov material and a heavy absorber material (in this case steel or brass). The idea is that when a particle hits the absorber it will cause the creation of secondary particles. As these secondaries propagate through the HF they also interact with other layers of absorber ultimately creating a "shower" of particles. These showers create blue-violet light as they pass through the quartz Cherenkov fibers. There are then many 1-mm diameter wavelength shifting fibers that collect this light and shift it to the green region and this light is collected and counted by the HF readout system. The amount of light

collected is multiplied by a calibration constant to estimate the amount of energy the particle deposited into the specific channel.

The Forward Hadronic Calorimeter(HF) detector subsytem provides full azimuthal coverage over $2.9 < |\eta| < 5.2$, and is required to withstand high particle flux. For each pp collision at design energy, it was estimated that approximately 70 GeV of total energy would be deposited into the HF, compared with only 100 GeV for all of the detector subsystems with $|\eta| < 3$. The HF is comprised of 6 mm thick grooved steel absorber players, with grooves that are approximately 1 mm wide and deep. Quartz fibers are inserted into these grooves. Along with the cladding, the diameter of the fibers is $800 \pm 30\mu m$, and over 1000 km of total fiber length was used to construct the HF.

A signal is generated in the quartz fibers when charged particles with an energy above the Cherenkov threshold ($\geq 190keV$ for electrons) generate Cherenkov light which is guided to photomultipliers stationed behind a shielding matrix. Half of the quartz fibers run over the full depth of the detector (165 cm) while the other half begin 22 cm from the front of the detector. These two sets of fibers are read out separately, allowing one to distinguish between showers generated by electrons or photons and those generated by hadrons. The hadron showers will on average deposit more energy deeper into the absorber material. Fibers are bundled into 175×0.15 ($\Delta\eta \times \Delta\phi$) towers. The HF is shown in Fig 2.7 [48].

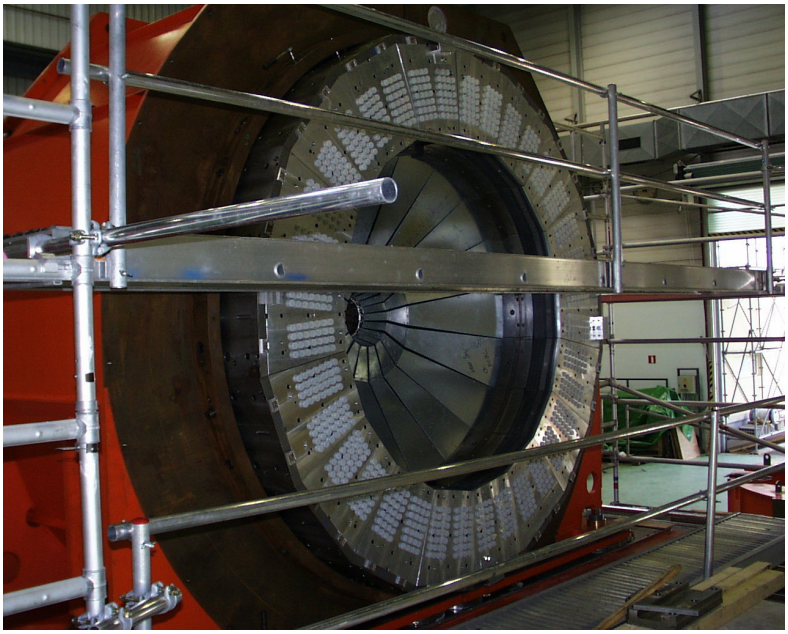

Figure 2.7: Half of the CMS Forward Hadronic (HF) Calorimeter.

2.2.2 Tracker

Closest to the interaction point (IP) are the two systems that make up the CMS tracker, the silicon pixel tracker and the silicon strip tracker. The silicon pixels measure the location and trajectory of the particles as they leave the collision area and are as close as they can be to the IP because that region has the highest particle density immediately after the collision. The inner tracker measures the particle's trajectory by the ionization of the silicon in the channels. The ionization of the silicon channels allow the loose electrons to travel into a read out via an electric potential gradient. Each readout channel reads the amount of arriving charge which is converted to voltage and determines whether a particle was present in that channel. At the time of the LHC's conception there were expected to be around 1000 particles produced within the tracker per bunch crossing, where on

average 20 pp collisions would occur. This is not too dissimilar from the number of produced particles produced in a single PbPb collision at $\sqrt{s_{NN}}$ =2.76 TeV, which was measured to be 1612 ± 55 per unit pseudorapidity at $\eta = 0$ [23].

The tracker is a cylindrical volume centered at the nominal interaction point of CMS with a length of 5.8 m and a radius of 1.26 m. The solenoid magnet of CMS is designed to provide a nearly uniform 4 Tesla magnetic filed throughout the tracker. During the runs between 2009 and 2013 the actual field strength was 3.8 Tesla. In order to handle the high flux of particles per collision and brief time between each bunch crossing, the system needs fine granularity and a very fast response time. All of this required the designs for the tracker to have on-detector electronics and subsequently a highly efficient cooling system. These demands are always balanced with the concern of photon conversion, multiple scattering and nuclear interactions that could degrade the precision of the measurements of the tracks and surrounding calorimeter systems.

The tracker is comprised of two major subsystems, the silicon pixel detector, and the silicon strip detector. The pixel detector is closest to the beampipe and is made of three concentric cylindrical barrel layers at midrapidity, and two disc-shaped endcap layers at positive and negative forward pseudorapidity. Just outside of the pixel detector, the silicon strip detector is comprise of 10 barrel layers called the Tracker Inner Barrel (TIB) and Tracker Outer Barrel (TOB). In the forward regions the silicon strip detector has 3 smaller disc layers called the Tracker Inner Disc (TID) and 9 larger disc layers called the (TEC). A schematic cross section of the inner tracker is shown in Fig 2.8.

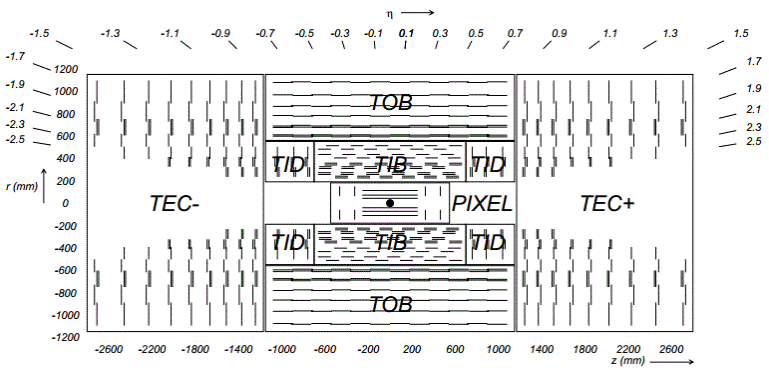

Figure 2.8: Schematic cross section of the CMS silicon inner tracker [27]. Each short line represents a detector module, with double lines indicating back-to-back modules that deliver stereo hits.

2.2.2.1 The Silicon Pixel Detector

The silicon pixel detector consists of three 53-cm long barrel layers at a distance of 4.4, 7.3 and 10.2 cm from the nominal interaction point, and four endcap layers at $z = \pm 34.5$ cm and $z = \pm 46.5$ cm at a distance of 6-15 cm from the beam axis. This gives complete azimuthal coverage over the pseudorapidity range of $|\eta| < 2.5$, ensuring that nearly every possible trajectory will intersect the detector on some combination of three layers. At low η the three barrel layers will provide the three hits needed to reconstruct a helical trajectory, and at high η the innermost barrel layer combined with the two endcap layers likewise provides three hits.

The detector is comprised of pixel cells with an area of 100×150 μm^2. This allows for precise resolution of track trajectories in both the $r - \phi$ and z directions, which in turn allows for a precise reconstruction of a secondary vertex position in 3D space. In total, the system contains over 66 million pixel cells, covering a total

area of 1.06 m^2.

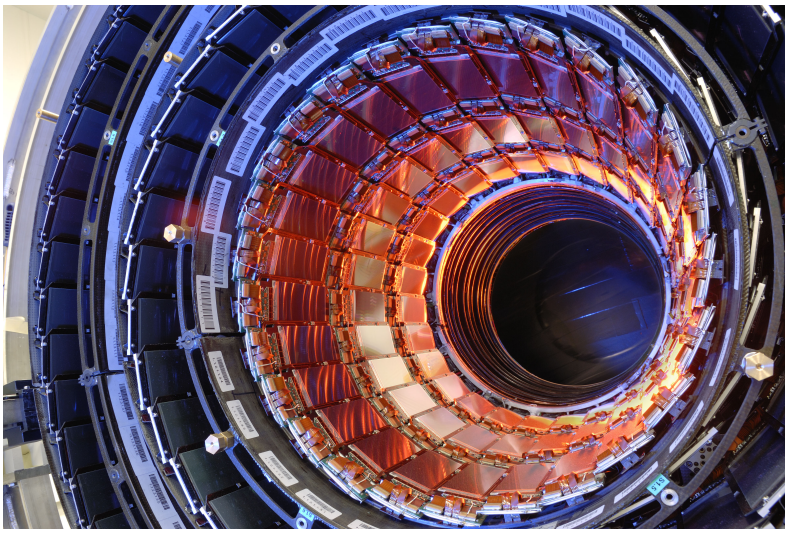

Figure 2.9: Picture of a section of the CMS pixel tracking system.

2.2.2.2 The Silicon Strip Detector

Outside of the pixel detector, the increased distance from the IP allows for larger cell size while keeping overall occupancy low. Assuming an average of 1000 charged particles per bunch crossing, the hit density of the innermost pixel barrel layer at 4 cm from the collision point is about 0.025 particles per mm^2. At 22 cm from the collision point, where the innermost TIB layer resides, the hit density falls to 0.0015 particles per mm^2. Finally, at 115 cm, at the outermost layer of the TOB, the hit density has reduced to 7.5×10^{-5} particles per mm^2. It is therefore possible to achieve 2-3% occupancy on the innermost TIB layer with the silicon microstrips with a typical cell size of 10 cm $\times 80$ μm, and in the outer TOB region with a cell size of 25 cm $\times 180$ μm. The silicon strip detector contains a total of 9.3 million strips and covers an area of 198 m^2.

Chapter 3: **Tracking**

3.1 Overview of Charged-Particle Reconstruction in the CMS Detector

A charged particle in a uniform magnetic field follows a helical trajectory that can be completely described by five parameters. For the reconstruction of charged particles in the CMS tracker, the following five parameters are used [2]:

- p_T, the transverse momentum
- $\lambda = \cot(\theta)$, where θ is the polar angle
- ϕ, the azimuthal angle
- $d_0 = y_0 \cos(\phi - x_0) \sin(\phi)$, where x_0 and y_0 are the transverse coordinates of the helix and point of closest approach to the z-axis.
- z_0, the longitudinal coordinate of the helix at the point of closest approach to the z-axis

A reconstructed charged-particle trajectory is referred to as a track. As a charged particle traverses a layer of tracker, it will strike the silicon at some angle,

resulting in a signal in multiple pixels or strips. The signals that are thought to originate from a single charged particle are combined to form a cluster, which is then analysed and corrected for the alignment of the detector to give a precise estimate of the charged-particle position as it traversed the detector, which is called a hit. Tracks are reconstructed by applying a pattern recognition algorithm to a sequence of hits on various layers of the silicon pixel and strip detectors.

Track reconstruction begins with the estimate of a helical trajectory called a seed which is formed from a set of three hits on different layers, or in some circumstances, hits on two layers and a measurement of where the collision specifically occurred. A Kalman Filter algorithm [19] is used to propagate this trajectory outward through additional layers, finding hits that are compatible with the trajectory estimate and updating the statistical fit. Tracks may then be selected based on quality criteria, such as the number of hits on the track or the χ^2 goodness of fit.

By analysing the tracks from many events, one can determine the position of the beamspot, which is the position of the beam in the collision region. This is a very precise region in the transverse plane, with a typical radius on the order of 16 μm. The track-based beamspot measurement algorithm can, in ideal situations, provide a measurement accurate to 2 μm [38]. The interaction region covers a much longer distance along the z-axis, in which collisions follow a Gaussian distribution centered around some point z_0, with a typical spread on the order of σ_{z_0} $\tilde{7}$ cm. Additionally, the beamspot will typically have some small gradient $^{dy}/_{dz}$ and $^{dx}/_{dz}$. All of these parameters are measured in an initial reconstruction of a subset of the total data sample and stored for subsequent use in the reconstruction of the full sample.

After tracks have been reconstructed for an event, the tracks and beamspot information may then be used to estimate the precise positions of the inelastic collisions, which are called primary vertices. Vertex information may then be used to perform additional, more precise track reconstruction, which in turn may be used to better estimate the positions of the primary vertices.

3.1.1 Pixel and Strip Hit Reconstruction

The signals from the silicon strip detector are corrected for known offsets and common mode noise, and are zero-suppressed for pp and pPb collision runs previous to recording the event in RAW format. However, the non-zero suppressed silicon strip data were recorded in PbPb collision events where the increased particle flux creates a non-trivial amount of highly-ionizing particles (HIPs) that can create large signals in the silicon strips through hadronic interactions. This can create a distortion in the common mode noise baseline affecting each 128-strip readout, which must be calculated for each event and subtracted. This distortion can take the form of a slope or sag in the baseline across the 128 coupled strips. An example of this is shown in Fig. 3.1. For such a case, a specialized baseline restoration algorithm is run that attempts to discern the signal peaks from the sloped baseline. The results of this algorithm in one instance is also shown in Fig. 3.1.

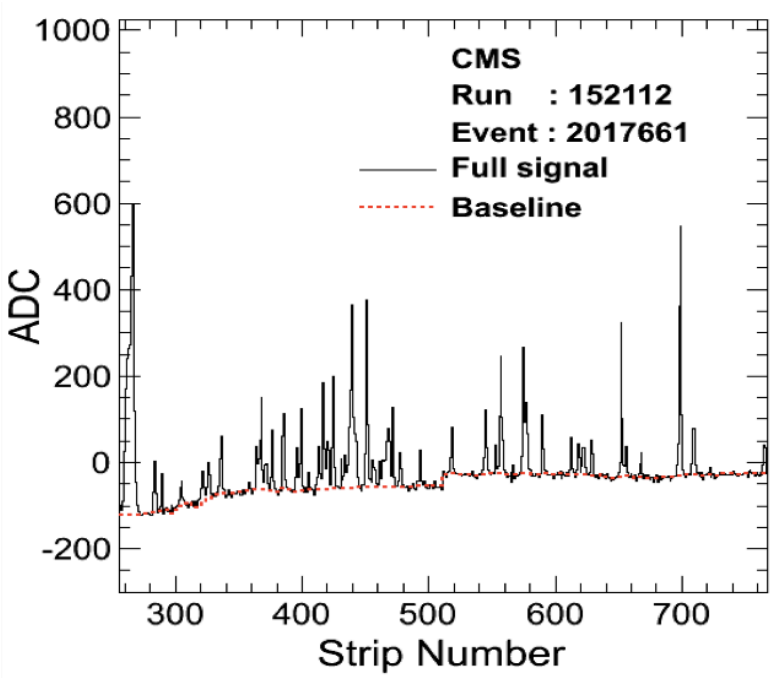

Figure 3.1: Pedestal-subtracted readouts from silicon strips as a function of strip number, where strips are numbered sequentially along the module. Four groups of 128 strips each corresponding to an APV25 readout chip are shown. The spikes are signals from charged particles, and the density of spikes indicates that the module has been affected by a HIP. The red dotted line indicates the reconstructed common-mode-noise baseline.

Silicon strip clusters are then reconstructed using a three-threshold algorithm. First, a seed strip is selected with a higher signal than neighboring strips, with a threshold of at least 3 times the signal-to-noise (S/N) ratio. Then the strips are added to the cluster on either side of the seed if their signal exceeds a second threshold of at least 2 times the S/N ratio. The cluster grows outward until the next strip is below threshold. Once the cluster is complete, it is accepted only if the total

signal size of the cluster excceeds a threshold of 5 times the quadratic sum of the noises of all the associated strips. The geometric center of the cluster in the local coordinate system of the module is determined by taking the centroid of the signal heights in the strips. This is corrected for the Lorentz shift of the charge carriers traversing the silicon due to the 3.8 Tesla magnetic field.

Pixel clusters are constructed by starting with a seed pixel containing a readout above a threshold more than 6 times the S/N ratio, and expanded outward by including adjacent pixels including corners that are above threshold. An example of a pixel cluster from a barrel module at high pseudorapidity is shown in Fig. 3.2.

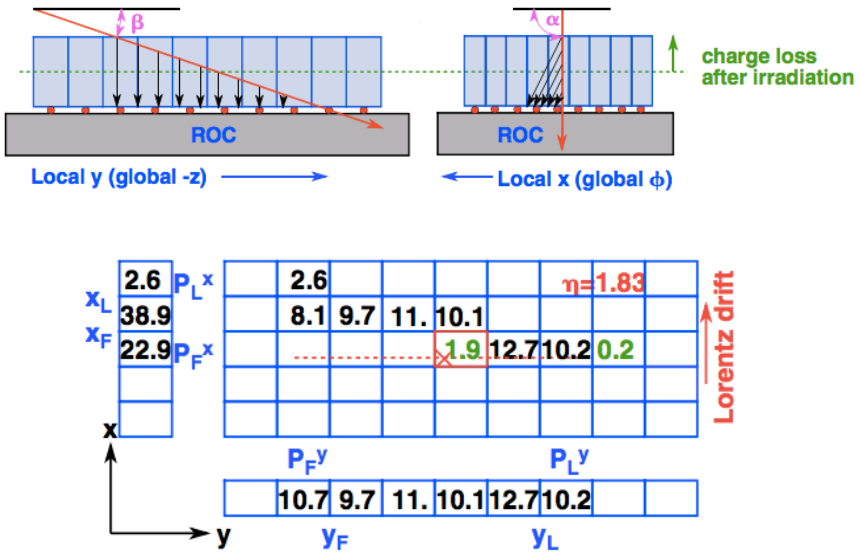

Figure 3.2: (Top) Cartoon of a charged particle (red arrow) traversing a barrel pixel detector module. The motion of deposited charge is indicated with the black arrows, with charge sharing between adjacent pixels along the global ϕ axis resulting from Lorentz-drift from the 3.8 Tesla magnetic field. (Bottom) Charge deposits from the same particle traversal as shown above in each pixel. The numbers represent thousands of electrons. Pixels shown in the green are below threshold and are not added to the cluster. The corrected position of the hit, accounting for Lorentz-drift, is shown by the red 'X'[47] (See text for further description)

The coordinates of the pixel hit in the local (x, y) coordinate system of the pixel module may be determined separately for x and y using the following expressions[30]

$$x_{rec} = \frac{x_F + x_L}{2} + \frac{P_L^x - P_F^x}{P_L^x + P_F^x} \cdot \frac{W_{eff}^x\left(cot\left(\alpha\right)\right)}{2} - \frac{\Delta_x}{2}, \tag{3.1}$$

and

$$y_{rec} = \frac{y_F + y_L}{2} + \frac{P_L^y - P_F^y}{P_L^y + P_F^y} \cdot \frac{W_{eff}^y \left(cot\left(\beta\right)\right)}{2} - \frac{\Delta_y}{2}, \tag{3.2}$$

where the $P_{F/L}^{x/y}$ are the signals in the first and last clustered pixels along the x or y axis; $x_{F/L}$ and $y_{F/L}$ are the x or y coordinates of the boundaries of the first and second or last and next-to-last pixels, respectively; α and β are the angles of the charged-particle trajectory along the x or y axis, respectively (see Fig. 3.2). The $\Delta_{x/y}$ are the maximum expected Lorentz-drift of the charge carriers along each axis due to the 3.8 Tesla magnetic field. The $W_{eff}^{x/y}$ are the effective charge widths in each direction given by

$$W_{eff}^x \left(\cot\left(\alpha\right)\right) = \left|T \cot\left(\alpha\right) + \Delta_x\right| - \left(x_L - x_F\right), \tag{3.3}$$

and

$$W_{eff}^y \left(\cot\left(\beta\right)\right) = \left|T \cot\left(\beta\right) + \Delta_y\right| - \left(y_L - y_F\right), \tag{3.4}$$

where T is the sensor thickness. The angles α and β may be estimated from a previously reconstructed track trajectory in a second-pass reconstruction, or approximated using the assumption of a particle originating from the nominal interaction point. To further correct and account for radiation damaged pixel sensors, a template fitting algorithm has been developed and is described in [47].

Once a silicon strip or pixel cluster is determined and the geometric center of the cluster is identified in the local coordinate system of the detector module, this

position must be translated to the global coordinate system of the CMS detector. For tracking resolution on the order if $10 - 20$ μm, this requires an equally precise knowledge of the alignment of the detector module within the CMS apparatus.

Determination of the tracker alignment proceeds from analysing reconstructed tracks using prior estimates of the alignment starting from optical surveys of the tracker during commissioning, muon tracks from cosmic ray events taken prior to LHC collisions [32], and continuing as additional collision data is taken. The components of the tracker system may shift over time, so the alignment is recalculated and recorded for each separate time CMS ends recording collisions for a specified amount of time (a run).

The problem of alignment determination can be expressed in terms of a vector $\mathbf{p}$ representing the position of all tracker modules, and a collection of track trajectory vectors $\mathbf{q_j}$. For the ith hit on the jth track, the track residual is defined $\mathbf{r_{ij}} = \mathbf{m_{ij}} - \mathbf{f_{ij}}(\mathbf{p}, \mathbf{q_j})$, where $\mathbf{m_{ij}}$ is the measured hit position on the module, and $\mathbf{f_{ij}}(\mathbf{p}, \mathbf{q_{ij}})$ is the trajectory impact point given the alignment $\mathbf{p}$. In the case of a pixel module, $\mathbf{r_{ij}}$ is a 2-component vector, and in the case of a strip module it is a scalar as the position measurement is only 1-dimensional. The alignment problem can then be expressed in terms of minimizing the objective function

$$\chi^2(\mathbf{p}) = \sum_{j}^{tracks} \sum_{i}^{hits} \mathbf{f}_{ij}^T(\mathbf{p}, \mathbf{q}_j)\, \mathbf{V}_{ij} \mathbf{f}_{ij}(\mathbf{p}, \mathbf{q}_j), \tag{3.5}$$

where $\mathbf{V}_{ij}$ is a covariance matrix in the case of a pixel module, and a squared error in the case of a strip module. As there are tens of thousands of modules, each with six

degrees of freedom, translational, rotational, $\mathbf{p}$ has on the order of 10^5 components. This complex minimization problem is approached using two algorithms. The MILLIPEDEII [21, 32] algorithm uses a global approach to minimize χ^2, and the "Hits and Impact Points" algorithm [35] applies a local approach. From the results of the two algorithms, the final alignment is determined.

With the predetermined alignment of the tracker modules, the position determination in the local coordinate frame of the module can then be reliably translated to the global coordinate frame of the CMS detector. This corrected position based on the signal cluster is the reconstructed hit which may now serve as an input to the pattern recognition algorithms described in Section 3.1.2.

3.1.2 Seed Generation, Pixel Tracking, and Pixel Vertexing

Track reconstruction begins with the generation of a seed that should provide an initial constraint on the five parameters of the helical trajectory with small enough uncertainties for the Kalman Filtering algorithm to continue refining the measurement by adding subsequent layers.

Seeds may be generated from hits on three tracker layers called a triplet or from a pair of hits on two layers. A set of layers used to generate the seeds is first chosen, along with some constraint for the origin of the helical trajectory, and minimum p_T of the reconstructed trajectory. This origin constraint may simply be a cylindrical region around the nominal interaction point aligned with the z-axis. The beamspot may be used to provide a tighter constraint in the transverse plane,

but only a very loose constraint along the z-axis. If one or more primary vertices have been previously reconstructed, these may be used to provide a tight constraint in all directions.

The three layers of the pixel detector are the most accurate predictors of the helical trajectory, but some particles may not produce reconstructed hits on each layer of the detector that they traverse. These particles may be reconstructed either by seeding from pixel pair layers or using one or more layers of the strip detector as seeding layers.

In the case of triplet seeds from the pixel layers, the helical fit from these hits alone may be sufficiently precise as to accurately reconstruct a track. Such a track is called a pixel track. However, for high-p_T charged particles, the momentum resolution is not very good, owing to the small lever arm of the pixel detector. For a particle with $p_T = 10\ GeV/c$, the uncertainty of the reconstructed momentum may be as high as 22%.

Pixel tracks may be of use in cases where the Kalman filtering algorithm is not feasible or not desired due to CPU time constraints. One such application is as a preliminary reconstruction pass in pp or pPb collisions. These tracks are then used to reconstruct primary pixel vertices, which in turn provide seeding constraints for layer track reconstruction from pair seeds. Another application is for low-p_T tracking in the high occupancy environment of central PbPb collisions, where the occupancy of the strip detector prevents its use in better constraining the trajectory of the track. The algorithms used to constrain the helical parameters of pixel tracks and reconstruct pixel vertices are described in [29].

3.1.3 Combinatorial Kalman Filter

Kalman Filter algorithms have been used in charged-particle reconstruction in high energy and nuclear physics for over 20 years [18, 33]. The approach is fast as there is a linear rise in the number of computations with the number of measurements in the track, and it is robust in the presence of multiple scattering. At a given detector layer k, the state of a particle can be modeled as a vector x_k that encodes the position and momentum of the particle. The propagation of the particle to the next outward layer of the detector may be modeled by the linear equation

$$x_{k+1} = \mathbf{F}(k)\, x_k + \mathbf{G}(k)\, u_k + w(k), \tag{3.6}$$

where $\mathbf{F}(k)$ encodes the free propagation of the particle, $\mathbf{G}(k)\, w(k)$ encodes the known physics input, in this case the response to the magnetic field, and $w(k)$ is a random source of Gaussian noise with a known variance, in this case multiple scattering. The measurement of the particle trajectory at layer k is modeled as

$$z(k) = \mathbf{H} x_k + v(k), \tag{3.7}$$

where $\mathbf{H}x_k$ represents the measurement process, and $v(k)$ is a source of Gaussian noise in the measurement determination. At each stage, the state and covariance matrix of the particle trajectory is updated to include the new measurement information.

The algorithm used here is called a Combinatorial Kalman Filter (CKF), as

in many cases there are multiple hits on the next layer, which are compatible with the current trajectory measurement within the error estimate. Beginning with a trajectory and a position given from a seed, at each layer, the CKF will select all hits compatible with the trajectory, and subdivide them into a filter for each compatible hit. In addition, another filter will be initiated with the hypothesis that none of the compatible hits belong to the trajectory. These filters are propagated to the next layer where further subdivisions occur with each hit compatible with each trajectory estimate. To avoid a combinatorial explosion of filters as the algorithm propagates outward through several layers, the filters are pruned at each layer by removing trajectories with the highest χ^2 statistic.

In order to remove any biases introduced during the seeding state, after the track has been built out of hits determined from the first pass of the CKF, the filter is re-initialized at the innermost hit with the trajectory estimate from the seeding, and propagated outward using only the hits determined from the first pass. During this second pass the positions of the hits can be re-evaluated using the angles determined from the first pass, resulting in a more accurate measurement.

Finally, the track is evaluated with a smoothing stage where the filter algorithm is initialized using the results of the previous stage at the outermost detector hit, with the covariance matrix scaled by a large value. The filter is then run inward to the innermost hit, at each layer combining the estimates from the previous outward filter to form a combined final estimate. This procedure yields optimal estimates at each layer. The CKF filter approach to track reconstruction is described in more detail in [6].

3.2 Charged-Particle Reconstruction in pp and pPb Collisions

The reconstruction process in pPb collisions is the same as in pp collisions. As the occupancy of the tracker in a 2013 pPb collision event is similar to a 2012 pp collision event where there may be up to 20 individual collisions in the event, no special adjustment to the tracking algorithm is required. This process is important to understand as Pb-Pb track reconstruction is built on top of the already existing code made for pp collisions.

Three general stages of the pp and pPb reconstruction process are of interest to the measurement of low-p_T tracks. First, a set of pixel tracks are quickly reconstructed to then reconstruct pixel vertices as described in Sec. 3.1.2. These vertices are used in the seeding process for a robust, multi-stage algorithm described in Section 3.2.1. Finally, these tracks are used for the precise reconstruction of primary vertex positions.

3.2.1 Iterative Tracking

The pp track reconstruction strategy follows an iterative approach consisting of several repetitions of the CKF tracking algorithm on increasingly smaller subsets of the tracker hits. At the time of the pPb data taking, this procedure had expanded into seven iterations. Because the multiplicity of pPb collisions is similar to high-pileup pp events, this procedure could be applied to the pPb data without

modification.

Each iteration differs in terms of the layers used to seed the trajectory reconstruction, the minimum p_T of the particle being reconstructed, and the spatial region from which the trajectory may originate. Between iterations, hits that belong to reconstructed tracks of good quality (designated *highPurity*) are removed from the collection of hits used in the next iteration.

In the first two iterations, combinations of three pixel layers from the barrel and/or endcap (pixel triplets) are used as seeds. In both these iterations, the trajectory origin is constrained to a narrow region in the transverse plane around the beamspot. The third iteration utilizes seeds from pairs of pixel hits (pixel pairs) and further constrains the trajectory origin to be very close to a reconstructed pixel vertex along the z-axis. The fourth iteration again uses pixel triplets, but relaxes the origin constraint to search for tracks that may be displaced from the primary vertex, such as weak decay products of D or B mesons. The fifth iteration seeds from a mix of layers from both the pixel and strip detectors to find further displaced tracks or tracks that failed to leave a sufficient number of hits in the pixel detector to be reconstructed in the pixel detector. The final two iterations seed from the strip detector layers, and may reconstruct further displaced tracks. The seeding layers and trajectory origin constraints of the seven iterations are summarized in Table 3.1. The p_T cut refers to the minimum allowed p_T of the trajectory, and the d_0 and z_0 are the maximum transverse and longitudinal distances from the beamspot center, respectively. The (*) indicates that the maximum distance is with respect to the nearest reconstructed pixel track rather than the beamspot.

Table 3.1: Parameters for the seeding of each tracking iteration used for pp and pPb collisions.

Iteration	**Seeding Layers**	**p_T cut (GeV/c)**	**d_0 cut (cm)**	**z_0 cut**
Initial Step (0)	pixel triplets	0.6	0.02	4.0σ
Low-p_T Triplet Step (1)	pixel triplets	0.2	0.02	4.0σ
Pixel Pair Step (2)	pixel pairs	0.6	0.015	0.09 cm(*)
Detached Triplet Step (3)	pixel triplets	0.3	1.5	15 cm
Mixed Triplet Step (4)	pixel, TIB, TEC triplets	0.4-0.6	1.5	10 cm
Pixel-less Step (5)	TIB, TID/TEC pairs	0.7	2.0	10 cm
TOB-TEC Step (6)	TOB, TEC pairs	0.6	6.0	30 cm

Following each iteration, tracks are filtered to remove tracks that are likely spurious or misreconstructed. Many such reconstructed tracks can be removed by simply selecting tracks with a good χ^2 or primary vertex compatibility. In order to construct a collection of tracks with minimal contamination of misreconstructed trajectories (i.e. *high purity*) while maintaining a high efficiency, a more sophisticated set of selections can be applied in which the selection criteria are varied for each track, depending on the p_T, η, and number of layers in which a hit is found. Tracks containing hits on many layers are less likely to be misreconstructed, so the selection criteria may therefore be loosened for those tracks. As described in [2], the

following eight quantities are used to select *highPurity* tracks:

- normalized χ^2 of the trajectory fit
- transverse impact parameter d_{xy} with respect to the beamspot
- longitudinal impact parameter d_z with respect to the nearest reconstructed pixel vertex
- significance of the transverse impact parameter $\frac{d_{xy}}{\delta_{d_{xy}}}$, where $\delta_{d_{xy}}$ is the uncertainty on d_{xy} from the track fit
- significance of the longitudinal impact parameter $\frac{d_z}{\delta_{d_z}}$, where δ_{d_z} is the uncertainty on d_z from the track fit
- number of track layers with a hit on the track, n_{layers}
- number of tracker "3D" layers with a hit on the track, specifically pixel layers or matched strip layers, $n_{3Dlayers}$
- number of layers missing hits between the first and last hit on the track, $n_{lostlayers}$

These selections were optimized for each iteration in simulation, and the following formulas were determined as selection criteria with parameters α_i and β that may be adjusted for each iteration:

- Normalized $\chi^2 < \alpha_0 \cdot n_{layers}$
- $|d_{xy}| < (\alpha_1 \cdot n_{layers})^{\beta} \cdot \sigma_{d_{xy}}$

- $|d_z| < (\alpha_2 \cdot n_{layers})^{\beta} \cdot \sigma_{d_z}$
- $\frac{d_{xy}}{\delta_{d_{xy}}} < (\alpha_3 \cdot n_{layers})^{\beta}$
- $\frac{d_z}{\delta_{d_z}} < (\alpha_4 \cdot n_{layers})^{\beta}$

Table 3.2: Parameter values used for selecting *highPurity* tracks for each tracking iteration.

Iteration	n_{layers}^{min}	$n_{3Dlayers}^{min}$	$n_{lostlayers}^{max}$	β	α_0	α_1	α_2	α_3	α_4
0	3	3	2	4	0.70	0.30	0.35	0.40	0.40
1	3	3	2	4	0.70	0.30	0.35	0.40	0.40
2	3	3	2	4	0.70	0.30	0.35	0.40	0.40
3_{VTX}	3	3	1	3	0.70	0.85	0.80	0.90	0.90
3_{TRK}	5	4	1	4	0.40	1.00	1.00	1.00	1.00
4_{VTX}	3	3	1	3	0.40	1.10	1.10	1.20	1.20
4_{TRK}	5	4	0	4	0.30	0.90	0.90	0.90	0.90
5	4	3	0	4	0.20	0.90	0.90	0.90	0.90
6	5	2	0	4	0.20	1.40	1.30	1.40	1.30

In iterations 3 and 4, there are two sets of cuts applied, one focusing on track quality and the other focusing on vertex compatibility.

Here $\sigma_{d_{xy}}$ and σ_{d_z} are resolutions on d_z and d_{xy}, which are parameterized as $\sigma_{d_{xy}} = \sqrt{a^2 + \frac{b}{p_T}^2}$ and $\sigma_{d_z} = cosh(\eta) \cdot \sigma_{d_{xy}}$, where a=30 μm and b=10 μm $\cdot GeV/c$ Additionally, iteration-dependent selections on the minimum $n_{layers}, n_{3Dlayers}$, and

maximum $n_{lostlayers}$ are applied. The values of the parameters α_i and β and the minimum or maximum layer restrictions for each iteration are given in Table 3.2.

After each iteration, the tracks produced in the new iteration are merged with the tracks from previous iterations. This may result in the duplicate reconstruction of the same charged-particle trajectory. To remove these duplicates, tracks are checked for shared hits, and determined to be duplicate if they share more than 19% of the hits on the track with the least hits. In this case, the tracks are ranked by χ^2. The track with the lower χ^2 is retained in the final collection before moving to the next iteration.

Note that the seeding layers parameters in Table 3.1, the *highPurity* selection parameters listed in Table 3.2, and even the total number of iterations are adjusted with new software revisions. The values presented here are those used for the reconstruction of the 2013 pPb collision events. Earlier CMS measurements of pp collisions that are referenced may use a different set of iterations and cuts. In the future, these parameters may continue to be adjusted.

3.2.2 Primary Vertex Reconstruction

After iterative tracking is performed, an additional primary vertex reconstruction is performed using the collection of iterative tracks. This process begins with a clustering algorithm that assigns tracks to vertex prototypes based on their z coordinate at the point of closest approach to the beamspot. The algorithm proceeds using a simulated annealing technique [36, 31] to avoid local minima. The specific

algorithm employed is a "mass constrained clustering" described in [43].

The z positions of each track at their distances of closest approach to the beamspot is designated z_t, with a measurement uncertainty of σ_t. The number of vertex prototypes is a variable, and the z coordinate of each prototype may be given as z_v. Let c_{tv} represent a matrix element of the assignment of tracks to vertices, with $c_{tv} = 1$ if track t is assigned to vertex v, and 0 otherwise. To account for the fit quality and displacement of each track, an additional weight, p_t, may be assigned to each track. Additionally, a variable weight is given to each vertex, ρ_v, constrained so that $\sum_v \rho_v$=1. The figure of merit is then

$$\chi^2 = \sum_{t,v} p_t \rho_v c_{tv} \frac{(z_t - z_v)^2}{\sigma_t^2}. \tag{3.8}$$

Finding the minimum χ^2 by exhaustively searching all possible combinations of c_{tv} is not feasible given that both the number and values of the z_v can change. Instead the system is reinterpreted as an analogous thermodynamic system, with an energy $E_{tv} = \frac{(z_t - z_v)^2}{\sigma_t^2}$ associated with each pairing. Then χ^2 represents the total energy of the system. One may then look at a statistical ensemble of such systems, replacing the c_{tv} with probabilities p_{tv} that vary from 0 to 1, constrained so that $\sum_v \rho_v p_{tv} = 1$. Then the average energy of the ensemble is

$$\left\langle \chi^2 \right\rangle = \langle E \rangle = \sum_{t,v} p_t \rho_v p_{tv} E_{tv}. \tag{3.9}$$

Then at thermal equilibrium at some temperature $T = \frac{1}{\beta}$, the p_{tv} are given by the

Boltzmann factor,

$$p_{tv} = \frac{e^{-\beta E_{tv}}}{\sum_{v'} \rho_{v'} e^{-\beta E_{tv'}}}. \tag{3.10}$$

At a given temperature, the p_{tv} is determined for the current vertex positions, z_v, and weights, ρ_v, are updated as

$$z_v \to \frac{\sum_t p_t \rho_v z_t / \sigma_t^2}{\sum_t p_t p_{tv} / \sigma_t^2}, \rho_v \to \rho_v \frac{\sum_t p_t p_{tv}}{\sum_t p_t}. \tag{3.11}$$

This process proceeds iteratively until the change in the z_v and ρ_v is below some threshold, and equilibrium is then said to be established.

The algorithm proceeds in three phases. In the first, the initial condition is set with a very high temperature, equal p_{tv} values, and two vertices at some $z_0 \pm \delta$. Equilibrium is established and the temperature is reduced by a small step value, and the process of finding equilibrium repeats.

At any point during this first phase, if the temperature of a vertex drops below a critical temperature, T_c, defined as

$$T_c = 2 \frac{\sum_t \frac{p_t p_{tv}}{\sigma_t^2} \left(\frac{z_t - zv}{\sigma_t} \right)^2}{\sum_t \frac{p_t p_{tv}}{\sigma_t^2}} \tag{3.12}$$

the vertex is then split into two new vertices at $z_k \pm \delta$, and the algorithm continues.

If this splitting phase is allowed to continue to $T = 0$, the final result will be a large collection of vertices, each matched with a single track. The spatial resolution of the algorithm increases as temperature decreases, so at some point it is advantageous to halt splitting but continue to anneal to optimize the vertex

positions. At some minimum temperature, chosen here as $T_{min} = 4$, the algorithm enters a second phase where no further vertex splitting is allowed.

In the second phase, all vertex weights are set to be equal as they are only required for splitting determination, the position of the vertices is updated as before, and the Boltzmann factor for the p_{tv} is modified to include a "noise cluster" with an energy of assigning a track to the cluster being set at a fixed $E = \mu_0^2$, with no dependence on z_t. This serves to remove tracks that cannot be well associated with any vertex determined so far. The algorithm now proceeds down to $T = 0$.

The second phase makes the algorithm robust against noise from poorly reconstructed or displaced tracks, but does not prevent poorly determined vertices themselves. In the final assignment phase, each vertex is required to contain at least two tracks with an assignment weight of at least $p_{tv} = 0.9$. After removal of the poor vertices, the system is re-thermalized with the remaining vertices. Final track clusters are selected by associating tracks with $p_{tv} > 0.5$ to the prototype vertex v, with normalization of the p_{Tv} ensuring that tracks are not associated with multiple prototypes.

Once the track clustering algorithm is complete, a set of approximate vertex positions are determined longitudinally along the beamspot, each with a set of associated tracks. To better refine the position of these prototype vertices, an Adaptive Vertex Fitter (AVF) algorithm is employed, as described in detail in [45].

The AVF employs an iterative re-weighted least squares approach that down weights tracks according to their standardized distance from the vertex. In order to avoid local minima, the weight function is determined with a "temperature"

according to a geometric annealing schedule, with a Kalman filter formalism used to determine the vertex position at each iteration.

The result of this final algorithm is a set of primary vertices with a precise 3D estimate of the position of the collision. While this algorithm generally performs well in determining each primary collision vertex in an event, the clustering scheme will reconstruct a single collision vertex as a split pair of vertices about 10% of the time in pPb collisions.

3.3 Charged-Particle Reconstruction in PbPb Collisions

Track reconstruction in central PbPb collisions is a challenge due to the extremely high occupancy of the tracker pixels and especially strips. In Fig. 3.3, an event display of a central PbPb collision event taken in November 2010 is shown, which provides a sense of the sheer number of charged-particle trajectories that must be unambiguously reconstructed.

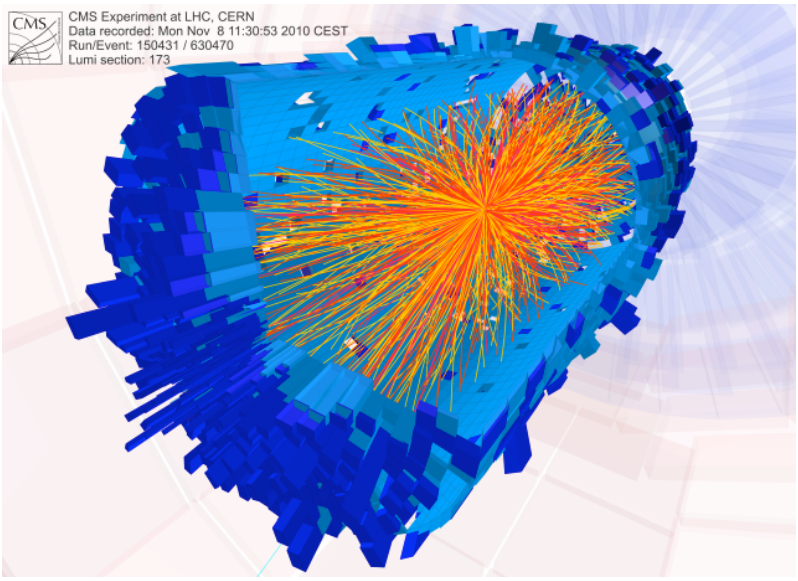

Figure 3.3: Event display of a central PbPb collision event taken in November of 2010. The red and orange lines represent reconstructed tracks with $p_T > 0.9$ GeV/c and the blue boxes represent calorimeter towers. Note that the bulk of the charged-particle production occurs with $p_T < 0.9$ GeV/c, so that only a small fraction of all charged-particle trajectories are actually shown[25]

As shown in Fig.3.4, early simulations of central PbPb collisions predicted that the channel occupancy, defined as the fraction of pixels or strips above threshold in each layer, could reach as high as 1% in the inner pixel layer and 30% in the inner strip layer. This presents a challenge for the seeding of track reconstruction, as the number of potential triplet seeds from the pixel layer may easily number in the millions even given a reasonable beamspot constraint and minimum p_T threshold. The high occupancy in the inner layers of the strip detector presents a challenge for the CKF algorithm, as the number of compatible hits on the inner strip layer may be very large for a given trajectory estimate.

The iterative reconstruction algorithm used in pp and pPb collisions is not feasible for central PbPb events due to the CPU and memory limitations of the currently available hardware. A different algorithm has been developed in order to overcome the issue of seeding, and for low-p_T reconstruction, the issue of strip occupancy.

In order to begin tracking with a reasonably small number of seeds, pixel triplet layers are used in conjunction with an estimate of the primary vertex position along the z-axis. This estimate must be determined without the use of a full set of reconstructed tracks, using a procedure described in Sec. 3.3.1. The minimum trajectory p_T is set to 0.9 GeV/c. These constraints result in a small enough number of seeds with a small enough window of compatible hits on the first strip layer to be propagated successfully using the CKF algorithm.

To reconstruct tracks with $p_T < 0.9$ GeV/c, a second tracking iteration is performed with pixel triplet seeds. These tracks are not propagated with the CKF filter, but fitted as pixel tracks as described in Sec. 3.1.2. These two iterations are then merged into a final collection described in Sec. 3.3.4.

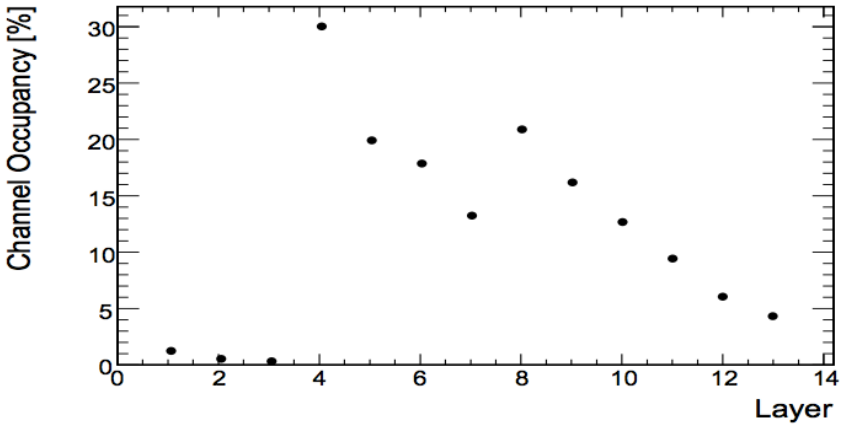

Figure 3.4: The expected occupancy in the barrel pixel detector (layers 1-3), TIB (layers 4-7) and TOB (layers 8-13) expressed as the percent of pixels or strips above threshold for central PbPb collision events[42]. Note that this result is from an early simulation used for the initial determination of a PbPb tracking procedure where particle multiplicities of $^{dN}/_{dy}$ ~3000-3500 were expected. Analysis of the 2010 collision data at $\sqrt{s_{NN}}$ = 2.76 TeV revealed that at midrapidity $^{dN}/_{d\eta}$ ~1600 for central events [23]. Particle multiplicities may be higher in the future when PbPb collision data is taken at the design energy of $\sqrt{s_{NN}}$=5.5 TeV.

As of this writing, the tracking reconstruction sequence for PbPb collisions is still undergoing development. The specific two-iteration sequence described here is not common to all published CMS PbPb collision results, but was developed specifically for the measurement of the charged-particle spectra at low-p_T. Other measurements performed over the same time frame used different sequences to match their physics goals. The following description should not be taken as a general reference for all CMS measurements of the 2010 PbPb collision data.

3.3.1 Primary Vertex Reconstruction

The primary vertex in PbPb collision events is reconstructed assuming that only one PbPb collision is present in each event, which is reasonable given the bunch intensity for the PbPb data taken in 2010 and 2011. Before any track reconstruction can begin, which is typically required for any vertex reconstruction, an approximate estimate of the vertex position must be determined to limit the origin radius of the seeds along the z-axis.

The first rough approximation is performed by reconstructing a cluster vertex using only the information from the first layer of the pixel barrel detector. The cluster vertex is estimated using a simple algorithm that looks at the length of each pixel cluster along the detector z-axis (see Fig 3.2 for an example of cluster length), and determining if the length of the cluster is compatible with the angle of a charged particle originating from some point z_0 along the z-axis. Starting at $z_0 = -30$ cm from the nominal interaction point, and incrementing by 0.1 cm up to $z_0 = 30$ cm, the algorithm calculates the number of pixel clusters with a length compatible with a particle originating at z_0. The value of z_0 with the most compatible clusters is taken as the initial estimate of the primary vertex position.

Once the cluster vertex is produced, an origin region for pixel triplet seeds is created with a loose constraint around the z-position of the cluster vertex, and a minimum p_T of 0.7 GeV/c. Even with the longitudinal constraint, the number of possible seeds is very large. The number of compatible trajectory seeds is estimated based on the number of pixel barrel hits, and the kinematic region for reconstruction

of these first pixel triplet seeds is accordingly narrowed in η around midrapidity in order to keep the number of resulting trajectories small. These trajectory seeds are reconstructed and called proto-tracks.

Proto-tracks are only used in order to obtain a better estimate of the primary vertex position and are then discarded. Even with the prior constraints, in a central event there may be many proto-tracks of poor quality that will adversely affect the AVF algorithm described in Sec. 3.2.2. In order to get a more refined estimate of the vertex position, a simple median vertex is reconstructed by taking the median of the z coordinates of all proto-tracks at their distance of closest approach to the z-axis. A subset of the proto-tracks are then selected for compatibility with the median vertex.

These selected proto-tracks are then used as inputs to the AVG algorithm. If the AVF algorithm returns more than one vertex, the "best" vertex is selected based on the sum of the p_T^2 of the proto-tracks associated with the vertex. If the AVF algorithm failed to produce a vertex with reasonable statistical errors, the median vertex is used instead. If both the AVF and median algorithms fail, the beamspot position is taken as the collision vertex. In this manner, every reconstructed PbPb collision event is guaranteed to have exactly one reconstructed primary vertex. Once this primary vertex is selected, track seeding can begin in a tightly defined region around the vertex.

3.3.2 First Iteration CKF Tracking

Trajectory seeds for the first iteration are built from pixel triplets, and are constrained to trajectories with $p_T > 0.9$ GeV/c. The transverse distance of closest approach to the beamspot must be within 0.1 cm, and the longitudinal distance of closest approach to the selected primary vertex must be within 0.6 cm.

Before initiating the CKF algorithm, trajectory seeds with a transverse displacement from the selected primary vertex with a statistical significance of more than 6 σ, and a longitudinal distance of closest approach with an absolute value of more than 0.2 cm are removed.

The selection of good quality tracks was determined as part of the analysis effort for the measurement of charged-particle spectra and is discussed in Sec. 4.3.

3.3.3 Second Iteration Pixel Tracking

The second iteration of tracking reconstruction is also built from pixel triplets, except that the constraint is relaxed to include trajectories with p_T as low as $p_T = 0.2$ GeV/c. As with the first iteration, the transverse distance of closest approach to the beamspot must be within 0.1 cm, and the longitudinal distance of closest approach to the selected primary vertex must be within 0.6 cm.

Unlike the iterative approach in pp and pPb collisions, the hits associated with the high-quality tracks from the previous iteration are not removed. This is not done as the highly occupied detector may contain merged hits from multiple charged particles, and also because this removal did not result in appreciably improved

performance, as the majority of hits are not associated with quality tracks from the first iteration.

These trajectories are not propagated through the strip layers using the CKF algorithm, as the low momentum of the trajectories corresponds to a wide area of compatible hits in a highly occupied detector. As a result, the momentum of these trajectories is poorly determined at high-p_T.

To better constrain the momentum of the trajectory, it is refitted using the transverse position of the beamspot as a fourth constraint along with the three pixel hits. This over-determines the path of a helix, so one can meaningfully discuss a χ^2 goodness of fit for the trajectory along the three hits and the beamspot.

As before, the selection of good quality tracks was determined as part of the analysis effort for the measurement of directed flow and is discussed in Sec. 4.3

3.3.4 Merging Procedure for Track Collections

The merging of the track collections from the two iterations is performed as with the pp and pPb iterative tracking, where tracks are considered duplicated if they share more than 19% of their hits. In this case the resolution between duplicates is trivial - a first iteration CKF track is always preferred to a pixel track.

Another important difference is that at high-p_T it is difficult or impossible to distinguish between poor and good quality tracks. For this reason, pixel tracks with $p_T > 1.5$ GeV/c are removed from the final collection. Similarly the first iteration CKF tracks with $p_T < 1.2$ GeV/c are also removed.

Chapter 4: **Analysis**

4.1 **Flow Theory and Analysis Techniques**

Anisotropic flow is a measurement of the particle azimuthal correlation with respect to the reaction plane in a heavy ion collision. The true reaction plane, which is defined as the impact parameter b and the collision direction, however, is not known experimentally. In addition, there exists other sources of correlations in azimuth, for instance, the correlations from resonance decay, jets, and quantum effects. These correlations, which are not related to the reaction plane, are called non-flow correlations. The various methods proposed to estimate the magnitude of anisotropic flow have different sensitivities to the non-flow correlations and flow fluctuations, thus allowing the systematic checks on the flow measurements [39, 49].

In this section, the different methods that were used to measure anisotropic flow in this analysis are described.

4.1.1 **Event Plane Method**

The Event Plane (EP) method uses estimates of the true Reaction Plane to quantify the azimuthal anisotropy or flow. The magnitude of the anisotropy is what

determines the EP as well as the flow signal, so it is important to avoid autocorrelation effects whenever possible. This means that a particle used to measure an EP should not be included in the calculation of the anisotropy with respect to the EP.

The azimuthal dependence of particle yield can be described by a Fourier expansion [40]

$$\frac{dN}{d\left(\phi - \Psi_R\right)} = \frac{1}{2\pi}\left(1 + \sum_{n=1}^{\infty} 2v_n \cos\left(n\left(\phi - \Psi_R\right)\right)\right), \tag{4.1}$$

where N is the number of particles, ϕ is the azimuthal angle of the emitted particle and Ψ_R is the "true" RP, not the experimental observable. The magnitude of the flow, represented in Equation 4.1 by v_n is defined as:

$$\boxed{v_n^{obs} = \langle cos\left(n\left(\phi_i - \Psi_R\right)\right)\rangle} \tag{4.2}$$

Directed flow is the n=1 term in this expansion.

In practice there are different EP's that correspond to the different harmonics [40]:

$$X_n = \sum_i w_i cos\left(n\phi_i\right), \tag{4.3}$$

$$Y_n = \sum_i w_i sin\left(n\phi_i\right), \tag{4.4}$$

where X_n and Y_n are know as the *flow vectors*, and w_i are different weights. If for example number of particles is the weight, $w_i = 1$. For transverse momentum flow $w_i = p_T(i)$ and for transverse energy flow $w_i = E_T(i)$. The different weights that

were used in the analysis will be discussed in Sec. 4.4. With the flow vectors in hand the event plane can be ascertained by

$$\Psi_n = \frac{1}{n}\tan^{-1}\left(\frac{Y_n}{X_n}\right) = \frac{1}{n}\tan^{-1}\left(\frac{\sum_i w_i sin\left(n\phi_i\right)}{\sum_i w_i cos\left(n\phi_i\right)}\right). \tag{4.5}$$

Also notice that for the n^{th} harmonic the EP angle is restricted between,

$$-\frac{\pi}{n} \leq \Psi_n < \frac{\pi}{n}. \tag{4.6}$$

Because the orientation of the colliding system is different for each collision and is random, you would expect a flat Event Plane distribution. However, imperfections in detector response, dead channels and other laboratory based effects can lead to a non-uniform distribution and will thereby affect the flow analysis. There are three commonly used methods for flattening an Event Plane. The first step is to apply detector specific calibrations such as gain corrections; thus ensuring that if two particles of the same energy hit different channels in azimuth, that they will be weighted the same in the EP calculation. The second step involves the recentering of the event flow vectors to zero with a width of unity by [40]

$$X_n^{corr} = \frac{X_n - \langle X_n \rangle}{\sigma_{X_n}}, Y_n^{corr} = \frac{Y_n - \langle Y_n \rangle}{\sigma_{Y_n}}, \tag{4.7}$$

where X_n^{corr} and Y_n^{corr} are the corrected flow vectors and σ_{X_n} and σ_{Y_n} are the uncorrected distribution widths. These corrected vectors are then inserted into Eq. 4.5 yielding a new EP distribution. The final step involves an event-by-event shifting

of the angles [15]

$$\Psi_n^{corr} = \Psi_n + \frac{1}{n}\sum_i \frac{2}{i}\left[-\langle \sin\left(in\Psi_n\right)\rangle \cos\left(in\Psi_n\right) + \langle \cos\left(in\Psi_n\right)\rangle \sin\left(in\Psi_n\right)\right], \quad (4.8)$$

where Ψ_n^{corr} is the final corrected EP angle.

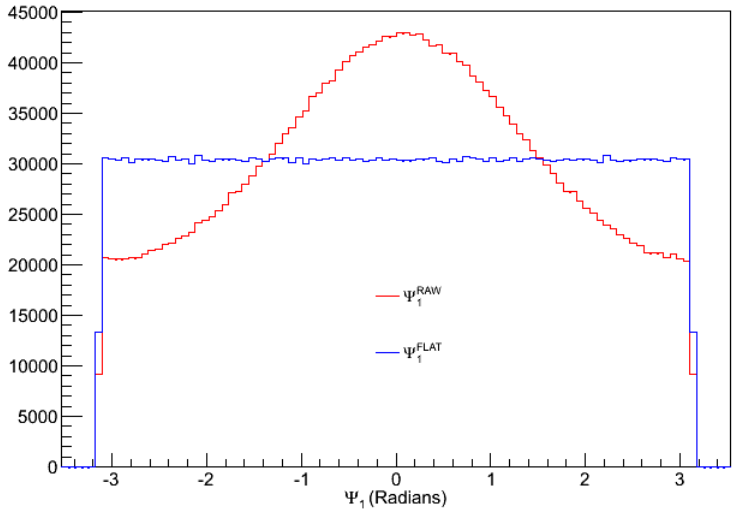

Figure 4.1: Flattened versus Unflattened Event Plane for the dataset used in this analysis.

Finally the EP resolution is a way to correct for non-flow correlations, finite detector segmentation and the finite number of particles. The EP resolution is defined as

$$\boxed{\sigma_{EP} = \sqrt{\langle \cos\left[n\left(\Psi_n - \Psi_R\right)\right]\rangle}} \quad (4.9)$$

However, as stated before Ψ_R is unknowable; in practice an EP angle is often calculated in two distinct subevent regions, a and b, in every event. These two regions are

most commonly chosen to be symmetric about the collision point, this ensures that each subevent will have the same detector acceptance, segmentation and particle multiplicity as the other subevent. In order to get to Eq. 4.9 then, one starts with the assumption that each particle in a subevent is correlated with the RP.

$$\cos\left[n\left(\Psi_a - \Psi_b\right)\right] = \cos\left[n\left(\Psi_a - \Psi_R\right)\right]\cos\left[n\left(\Psi_b - \Psi_R\right)\right] \tag{4.10a}$$

If one then assumes that the **only** correlation between Ψ_a and Ψ_b arises from their correlation with the RP then the product of the averages becomes the average of the product

$$\langle\cos\left[n\left(\Psi_a - \Psi_R\right)\right]\cos\left[n\left(\Psi_b - \Psi_R\right)\right]\rangle = \langle\cos\left[n\left(\Psi_a - \Psi_R\right)\right]\rangle\langle\cos\left[n\left(\Psi_b - \Psi_R\right)\right]\rangle. \tag{4.10b}$$

Now lastly, if the subdetectors used to measure sub-events a,b are symmetric then sub-events a and b are equal

$$\langle\cos\left[n\left(\Psi_a - \Psi_R\right)\right]\rangle\langle\cos\left[n\left(\Psi_b - \Psi_R\right)\right]\rangle = \langle\cos\left[n\left(\Psi_a - \Psi_R\right)\right]\rangle^2. \tag{4.10c}$$

so...

$$\langle\cos\left[n\left(\Psi_a - \Psi_R\right)\right]\rangle = \sqrt{\langle\cos\left[n\left(\Psi_a - \Psi_b\right)\right]\rangle}. \tag{4.10d}$$

The other commonly used EP resolution is calculated by using 3 non-equal multi-

plicity subevents, a,b,c with the following formula [40]

$$\langle \cos\left[n\left(\Psi_n^a - \Psi_R\right)\right]\rangle = \sqrt{\frac{\langle \cos\left[n\left(\Psi_n^a - \Psi_n^b\right)\right]\rangle \langle \cos\left[n\left(\Psi_n^a - \Psi_n^c\right)\right]\rangle}{\langle \cos\left[n\left(\Psi_n^b - \Psi_n^c\right)\right]\rangle}} \tag{4.11}$$

Once the EP resolution is determined, the observed flow signal is then calculated by Eq. 4.2. Since the EP is only an approximation of the RP, the true flow coefficient v_n in the Event Plane method is evaluated by dividing the observed flow v_n^{obs} by the resolution correction factor (σ_{EP})

$$\boxed{v_n\{EP\} = \frac{v_n^{obs}}{\sigma_{EP}}}. \tag{4.12}$$

4.2 Event Selection

The final data set used in this analysis contained 26,282,453 minimum-bias events taken from runs 181611 to 183013 during the 2011 Heavy Ion run. The number of events removed by the various cuts are shown in Table 4.1. The remaining events left after all cuts were found to have a flat centrality distribution for all but the most peripheral bins, as shown in Fig. 4.2.

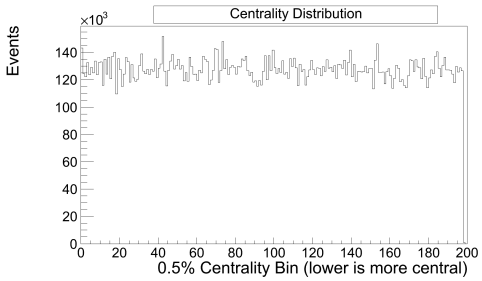

Figure 4.2: Centrality distribution for the 2011 Re-Reco MinBias dataset after all event selection and vertex cuts are applied. The centrality is given in 0.5% bins, where 0 refers to the most central events, and 200 to the most peripheral. The distribution is flat except for the most peripheral bins where trigger efficiency uncertainty plays a role. These most peripheral events were not a part of this analysis. Data selection cuts can be found in Tab. 4.1.

Data was reconstructed with CMSSW software version 5_3_16, as well as Global Tag GR_R_53_LV6.

Monte Carlo simulations were made with Global Tag START39_V7HI and CMSSW software version 5_3_16, as well as Global Tag STARTHI53_LV1.

In the following sections, the overall trigger strategy, trigger selection, and additional cuts for event selection are described in detail. Following the description of the event selection, a discussion of the centrality calculation is given.

4.2.1 Trigger strategy and constraints

The trigger strategy of CMS for PbPb collisions was constrained by the long (100–300 microseconds - depending on the run/date) holdoff time imposed by the

Table 4.1: The effects of various cuts on the data sample. % values are always with respect to to the line above (the cuts are applied in sequence).

Cut	events remaining	% of events remaining
AllPhysics events	77,436,924	100.00
HLT_HIMinBiasHfOrBSC trigger	28,085,577	36.26
no BSC halo	27,778,139	98.91
HF offline coincidence	26,863,533	96.71
reconstructed vertex	26,319,847	97.98
Beam-gas removal	26,283,993	99.86
HCAL timing	26,282,607	99.99
HCAL noise	26,282,453	99.99

pixel detector, issued after all accepted Level-1 (L1) trigger signals, and by the overall rate limitations of about 150 Hz (physics) for recording events, constrained mainly by the volume of data produced due to the Virgin Raw operating mode of the Silicon Strip Tracker and bandwidth and storage limitations downstream. The hadronic collision rate varied between 1 Hz and 210 Hz, depending on the number of colliding bunches (between 1×1 and 113×113) and on the varying bunch intensities.

For these reasons, the L1 trigger system had to provide a very efficient and clean trigger on hadronic collisions, with no or moderate (2 or 3) prescale for minimum bias events, and no prescale for high-p_T jets, muons, or photons, combined with a High Level Trigger (HLT) using L1 pass-through paths in many cases. HLT also prescaled certain triggers for various data streams to separate the most interesting events and the bulk of minimum bias collisions (in the interest of quick subsequent access to that "Core" physics dataset), and filtering and refining some of the L1 decisions, reconstructing jets, and so on.

4.2.2 Types of collisions and available L1 triggers

The CMS apparatus has various ways to trigger on PbPb collisions. The expected cross section for hadronic inelastic collisions is 7.65 barns, while ultra-peripheral collisions (UPC) with large impact parameters lead to the breakup of one, or both, Pb nuclei with a much larger probability (more than 200 barns for one or more neutrons in one ZDC and the cross section for ZDC coincidences is almost twice the hadronic interaction rate). Collisions in which the Pb nuclei interact

hadronically can produce anywhere from just a few up to to about 1600 particles per unit pseudorapidity, depending on the impact parameter. As a result, more than 97% of these collisions produce double-sided (coincidence) trigger signals in the BSC (Beam Scintillator Counters), and in the HF calorimeters (see the Centrality Sec. 4.2.4 for details). In addition, most of them are also detected by coincidences in the ZDC and in the BRAN scintillators (with scintillators placed behind the ZDC electromagnetic section). In order to suppress non-collision related noise, cosmics, radioactivity, trigger afterglow and beam background, all of these triggers were protected by the BPTX coincidence, i.e. two colliding ion bunches were required to be present in coincidence with each of these triggers.

The collision rate was 1–1.85 Hz per colliding bunch pair during the PbPb data taking period. Therefore (taking into account the 11245 Hz orbit frequency) the average number of collisions per bunch crossing was $0.9 - 1.6 \times 10^{-4}$.

In contrast to nuclear interactions, UPC collisions were found to be unable to activate the HF and BSC coincidence triggers. However, they contribute significantly to coincidence and singles triggers in the ZDC and in the BRAN scintillators. The additional trigger rate for these coincidence triggers from UPC collisions is comparable to that from hadronic collisions, while the single sided rates (which have very low or no noise) are more than an order of magnitude higher than the hadronic collision rate.

For these reasons, we have used the BSC and HF coincidence triggers to select hadronic PbPb collisions. These triggers have low noise (fake) rate (less than 1 Hz with two non-colliding beams at full intensity with 121 bunches), but very high

efficiency (about 97% even after an additional reconstructed vertex requirement).

4.2.3 Selecting minimum bias collisions

4.2.3.1 Triggering

Minimum bias (hadronic inelastic) collisions were selected by the L1 trigger system. Two clean and highly efficient triggers were used. One of them was the BSC coincidence "threshold 1", which requires at least one segment firing on each side of the interaction point. The BSC has 16 segments on each side (a total of 32 segments), out of which 31 were operational. Most (75% of) the collisions illuminate all 31 segments, thus the effect of one dead channel on the overall trigger efficiency (and bias) is negligible. This trigger is the bit "L1 Algorithm 4", named "L1_BscMinBiasThreshold1_BptxAND". The minimum bias trigger is changed to "L1 Algorithm 126", named "L1_HcalHfCoincPmORBscMinBiasThresh1_BptxAND", which is the Level-1 OR combination of the above L1_BscMinBiasThreshold1_BptxAND, and the "L1 Algorithm 94" named "L1_HcalHfCoincidencePm_BptxAND". The latter trigger bit is based on HF, and requires at least two HF towers to have deposited energies that exceed the threshold set by the firmware. It has similar efficiency as the BSC coincidence, and is also noise-free, but adds some small additional rate (efficiency) to detect minimum bias collisions. It is also more in line with (but less strict than) the offline event selection, which uses HF as well. Finally, in case either the BSC or the HF detector develops a problem (for example,possible massive BSC damage, or HF High Voltage turn-off, neither of which ever happened), the use of

an OR allows L1_HcalHfCoincPmORBscMinBiasThresh1_BptxAND to continue to record minimum bias collisions.

The minimum bias trigger was unprescaled at L1 level before reaching about 60 Hz collision rate, and then it was prescaled by 2 or 3, depending on the collision rate, to fit into the 150 Hz total HLT physics trigger limitation.

The HLT passed all of these (prescaled) minimum bias events through to the All Physics data stream, while prescaling them by a further factor of 10 before passing them to the Core Physics data stream, together with the unprescaled jet, muon, UPC. etc. triggers.

4.2.3.2 Offline event selection

In order to clean background, beam gas, PKAM (Previously Known As "Monster") events and UPC events from the minimum bias events, a few more cuts have been applied to select events off-line. These cleaning cuts have only a small effect on the number of selected events.

1. **BSC halo filter**: Events where any of the BSC halo bits fired (L1 Technical Trigger bits 36, 37, 38 or 39) were excluded from the analysis. Figure 4.3 shows a correlation between the number of hits in the first pixel layer and the total HF energy. Collisions passing all offline event selections (colored points) have a very tight correlation between the two quantities. However, events that fire the BSC beam halo bits have very small HF energy and quite a large number of pixel hits (black points near vertical axis). These are excluded from the analysis.

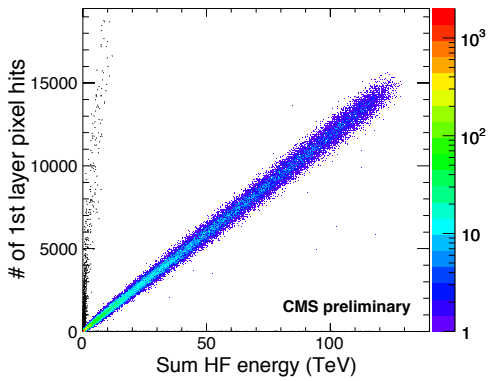

Figure 4.3: Correlation for minimum bias events between the number of pixel hits and the total energy deposited by the HF. Good collisions (colored points) have a tight correlation, while events firing the BSC halo bits, displaying PKAM-like features, or lacking a valid reconstructed vertex are off-diagonal. See text for details.

2. **Requirement of a reconstructed 2-track primary vertex was imposed.** In peripheral events, all tracks above 75 MeV/c transverse momentum were used to reconstruct the vertex. In central events, the minimum p_T requirement was increased, and the tracking region was narrowed down, to keep the maximum number of fitted tracks stable around 40–60, ensuring time-efficient reconstruction. This requirement removes non-inelastic-collision events (e.g. beam-gas, UPC) with large HF energy deposits but very few pixel hits (black points along horizontal axis in Fig. 4.3).

3. **A cut to remove PKAM events, which is a requirement of pixel cluster-length compatibility with the vertex.** This cut is the same as it was for the first 7 TeV pp paper on $\mathrm{dN/d}\eta$ and $\mathrm{dN/d}p_T$ [26]. In Fig. 4.3, most background

events with an excess of pixel hits compared to HF energy are removed by this selection. Some are already removed by the BSC beam halo filter alone, but all are eliminated by the combination of these two cuts. Figure 4.4 shows the cluster-vertex compatibility as a function of pixel hit multiplicity. The compatibility variable is the number of clusters that have a length (in the global z direction, i.e. along the beam) that is compatible with the reconstructed vertex, divided by the number of hits that are compatible with an artificially displaced vertex position (offset by $\pm$ 10 cm). If this ratio is high, that indicates a well defined vertex and a valid collision. If the ratio is about unity, that indicates that the vertex is ill-defined; a characteristic feature of PKAM events. At very low pixel multiplicity values, the compatibility is allowed to be low, in order to keep events that have a little larger background hit fluctuation but otherwise good collisions. Therefore a cut is applied, shown by the red line in Fig. 4.4, to remove events with high number of pixel hits and yet with a low value of the compatibility variable. The (b) panel is the same as (a), but zoomed in to the low pixel multiplicity region.

4. **A requirement of an off-line HF coincidence, which is requiring at least 3 towers on each side of the interaction point in the HF with at least 3 GeV total deposited energy.**

4.2.3.3 Additional Offline Event Selection

Two additional cuts were applied to the set of events, and cut away under 0.01 percent of the total sample and have a negligible effect on analysis. These cuts

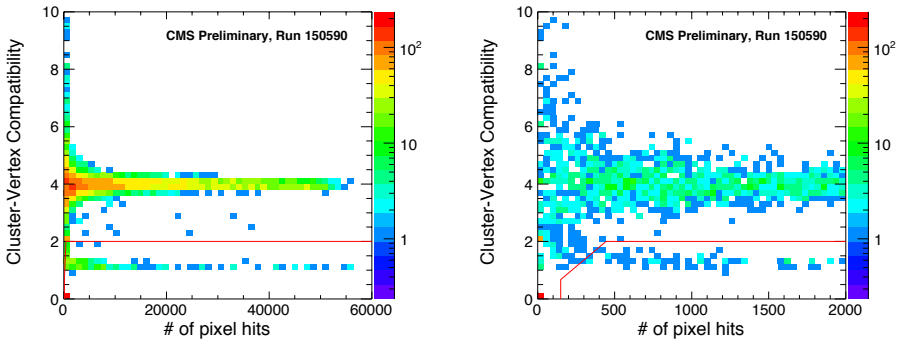

(a) (b)

Figure 4.4: The so called "monster" (or PKAM) cut. Events with a large number of pixel hits (horizontal axis) but a small value of the calculated measure of compatibility between the vertex position and the cluster lengths (vertical axis) are eliminated from the analysis (i.e. those events that fall below the cut shown by the red line.). (b) is an expanded version of the bottom left of (a).

involved the removal of events in which detector noise or incorrectly timed signals were detected in the HCAL that could lead to jet misreconstruction. This was done in order to facilitate future analysis in which the effect of identified jets on measured v_2 will be studied.

4.2.3.4 **Vertex Position Cut**

Events occurring far away from the center of the detector resulted in an asymmetry in reconstructed tracks in positive and negative pseudorapidity that systematically biased results. This asymmetry can be quantified as the number of tracks in forward rapidity minus the number of tracks in negative rapidity divided by the total number of tracks. This asymmetry is displayed for various $|\eta|$ ranges used in the analysis versus vertex position in Fig. 4.5.

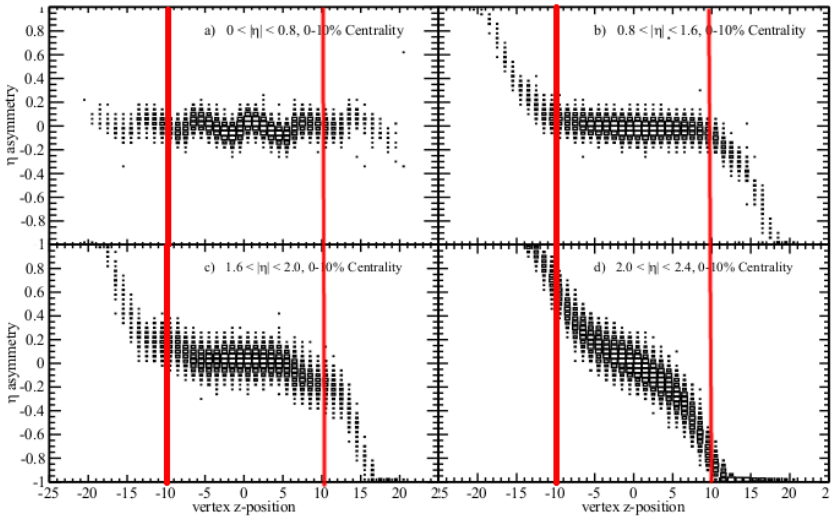

Figure 4.5: The z-position of the reconstructed vertex in cm versus the reconstructed tracking asymmetry in η. Eta asymmetry is defined as the number of reconstructed tracks in positive pseudorapidity minus those in negative pseudorapiditiy, all divided by the total number of reconstructed tracks.

To remove this effect, only events with a vertex within $\pm$ 10 cm of the center of the detector were used in the final analysis. The vertex position distribution is shown in Fig. 4.6

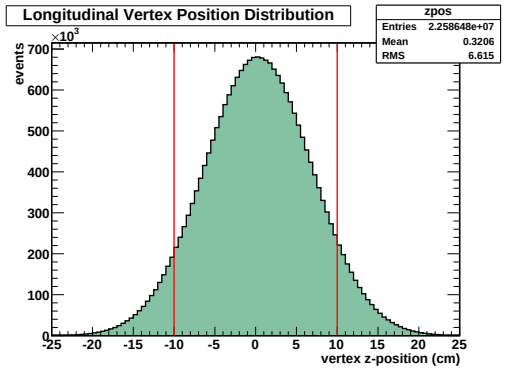

Figure 4.6: Distribution of the z-position of the reconstructed vertex, or position along the beam line for all selected events in the sample. Only events with a vertex within 10 cm of the center of the detector were included in the final analysis.

4.2.4 Centrality Description

For analysis of heavy ion events, it is important to be able to select events based on the impact parameter or the overlap fraction of the two colliding nuclei, something usually called simply "centrality". For this analysis, centrality is determined using the total sum of energy signals (HFRecHit) from both positive and negative Forward Hadronic (HF) calorimetry signals (covering $2.9 < |\eta| < 5.2$). The quantity used is total energy in both calorimeters, not E_T, and the resulting distribution is divided into 40 equal centrality bins, each corresponding to a selection that would contain 0.5% of the total inelastic nuclear cross section. A monotonic relationship between the HF energy signal and the centrality of the colliding nuclei allows the largest HF energy signals to be correlated with the most central collisions. This monotonicity is born out by simulation and correlation with other detectors, in particular the

Zero Degree Calorimeter. For the flow analysis, these fine-grained centrality bins of 0.5% "width" were combined into larger bins depending on the analysis done, as described in Sec. 4.4. The 50% most peripheral events were not analyzed as signal extraction is difficult due to low particle multiplicity.

4.2.5 Calculation of Centrality

In assigning percentages of total interaction cross section to specific ranges of HF sum energy, it is necessary to estimate the total number of actual interaction events from which the triggered sample was obtained. Minimum bias triggered data was utilized in generating the HF distributions for the centrality determination, and reconstructed events from this trigger were also required to pass the L1 beam halo rejection and to have a valid vertex with more than one track. Through Monte Carlo calculations, the efficiency of both the online and offline event selection for minimum bias Pb+Pb nuclear inelastic events is estimated as $\approx 97\%$. The high overall efficiency to Pb+Pb inelastic collisions enables a robust determination of the centrality bin limits, in particular for the flow analysis, as the uncertainties on the triggering efficiency plays an increasing role as one moves to the most peripheral events, which were not utilized in the flow analysis. For additional details, see [1].

4.3 Track Selection

To maximize the purity of the track sample, the tight cuts were applied to the collection of tracks given in Table 4.2.

Table 4.2: Various track quality selection cuts for the full tracks (the cuts are applied in sequence).

Cut	hiGeneralTracks
Number of Valid Hits (nHit)	≥ 13
dz/σ_{dz}	<10
dxy/σ_{dxy}	<3
p_T^{error}/p_T	<0.01
χ^2/ndof/nHit	<0.15

The pixel tracks that will be merged into the final tracking collection.

Table 4.3: Various track quality selection cuts for the pixel tracks (the cuts are applied in sequence).

Cut	hiLowPtPixelTracks
dz/σ_{dz}	<10
χ^2/ndof/nHit	<36

Pixel tracks are reconstructed down to p_T =0.2 GeV/c and fitted using the conformal map and line filter. In this technique the transverse position of the beamspot is used as an additional constraint to the fit of the three, or possibly four to six hits in the various pixel detector layers. This fitter has a much lower fake rate

in the high psuedorapidity region than a conventional helical fit of the three pixel hits. Additionally, the momentum resolution of the pixel tracks produced with the conformal fitter is superior to that produced by a helical fit. Only the two kinematic cuts shown in Table 4.3 are used to reduce the fake rate to near or under 5% in as wide of an η and p_T range as possible. Note that a cut on dxy/σ_{dxy} is not useful here as the pixel tracks are constrained to have dxy=0 in the fitting procedure.

4.4 Directed Flow Analysis

Unlike the other Fourier coeffcients, v_1 has to worry about conservation of momentum, the effects of which are seen primarily in the odd component of v_1 in more central collisions. Also unlike the other harmonics, v_1 is actually a combination of two different components [34]

$$v_1(y)\, e^{i\Psi_1(y)} = v_1^{even}(y)\, e^{i\Psi_1^{even}(y)} + v_1^{odd}(y)\, e^{i\Psi_1^{odd}(y)}, \tag{4.13}$$

where $v_1^{even}(y)$, $\Psi_1^{even}(y)$, and $\Psi_1^{odd}(y)$ are even functions of rapidity, while $v_1^{odd}(-y) = -v_1^{odd}(y)$. "Typical" directed flow is the odd component [9, 12, 10, 13]. The v_1 analysis done in this thesis is both the even and odd components and done using the Event Plane method.

4.4.1 $\mathbf{v_1^{odd}}$

The odd contribution of v_1 is calculated using the EP method. $v_1^{odd}(\eta)$ and $v_1^{odd}(p_T)$ are found for inclusive charged hadrons near mid-rapidity, $|\eta| \leq 1.5$, $p_T \geq$

0.2 GeV/c. For this analysis the HF is used to calculate the EP using Eq. 4.5. In the EP method, in order to calculate Ψ_1 it is necessary to multiply the flow vectors from one of the HF's by -1 in order to make sure that the back-to-back characteristics of v_1 are respected [13]. Centrality classes are chosen to most easily compare to other experiments, so for the EP method five different classes were used: 0%-10%, 10%-20%,20%-30%,30%-40%, and 40%-50%.

4.4.2 $\mathbf{v_1^{even}}$

The even component of v_1 is calculated using the EP method as well. Using a specific selection of weights [34], the EP is measured using the outer parts of tracker $|\eta| > 1.4$ using the following:

$$w_i = p_T - \frac{\langle p_T^2 \rangle}{\langle p_T \rangle}, \tag{4.14}$$

where the average p_T and p_T^2 are measured seperately for each centrality bin. The boon gained by using these weights is the immediate cancellation of conservation of momentum effects while simultaneously removing the odd component of v_1. As with the rapidity-odd v_1, there are five centrality classes :0%-10%, 10%-20%, 20%-30%, 30%-40%,40%-50%.

Chapter 5: **Systematics**

5.1 **Tracking Efficiency**

An important step in any analysis that uses charged particle information is a systematic study of the performance of the tracking subsystem. For CMS this is done in two steps. First, for efficiency, simulated particles are matched to reconstructed tracks. For a perfectly efficient detector, every charged particle would be reconstructed as a track. The ratio $\frac{N_{charged}}{N_{track}}$ is what is defined as tracking efficiency. This is usually displayed as a function of p_T and η, as seen in Figure 5.1.(a).

The second step in understanding the tracking performance is to look at the fake rate. This is done by looking at the Reconstructed tracks first and trying to match them to simulated charged particles. If a certain number of hits that were associated with a track do not belong to a simulated charged particle the two are not deemed to be associated. The tightness of the cut can be varied. If the χ^2 of the fit is set at a very high number, tracks will more easily be associated with simulated particles. For CMS, a standard [26] χ^2 value is 15. For this analysis we set a tighter cut of 8. This ensures that we are cutting down our fake rate as much as possible. The drawback with a tight cut is that the lower p_T tracks are often called fake by the system. This is seen in the lower corners of Figure 5.1.(b).

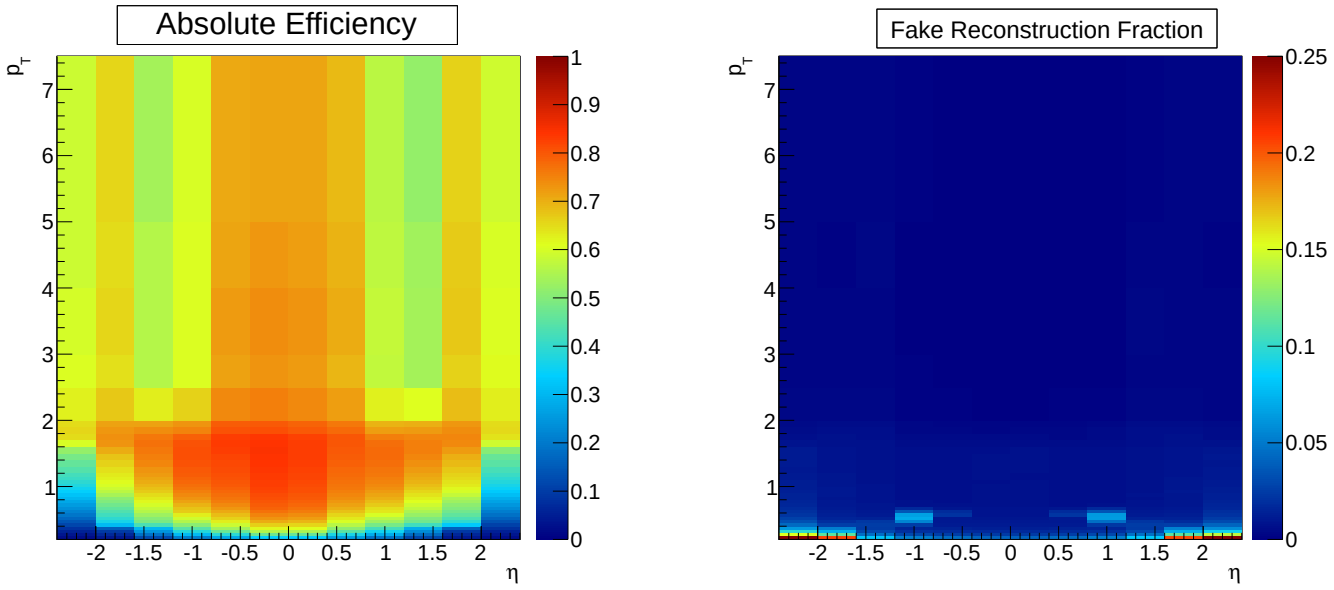

(a) (b)

Figure 5.1: A two dimensional look at both the tracking efficiency (a) and fake rate (b) for the 2011 MinBias data set.

During the summer and winter months of 2014 a large amount of time was spent optimizing the CMS Heavy-Ion track reconstruction code in order to reach even lower p_T tracks than ever before, $300 MeV/c$. In the track reconstruction process there are two routines at work. One process reconstructs tracks that are in the pixel system, this is the inner most 7 layers of the CMS tracker. The other process is made for tracks that go through almost all of the 13 layers of the CMS tracker.

The issue arises when both processes reconstruct the same track. In the end, when both tracking collections are merged together in order to make a single collec-

tion with all tracks, if the code does not notice that it has the same track twice it will lead to double counting. So a lot of time was spent trying to find the right balance of "priority" of a process depending on the p_T of the track. For instance, a lower p_T track is less likely to make it out of the pixel system, so if the pixel reconstruction identifies a track, its reconstruction is done and if the momentum is low enough, the "global" track reconstruction process will never kick in. The momentum ranges where either process, "global" or "pixel-only" reconstruction takes place was a topic of much study in 2014. The final cuts were decided upon (discussed in Sec. 4.3) and the tracking efficiencies and fake rates for the merged track collection, dubbed "*hiGeneralAndPixelTracks*" are shown in Fig. 5.2 and Fig. 5.3.

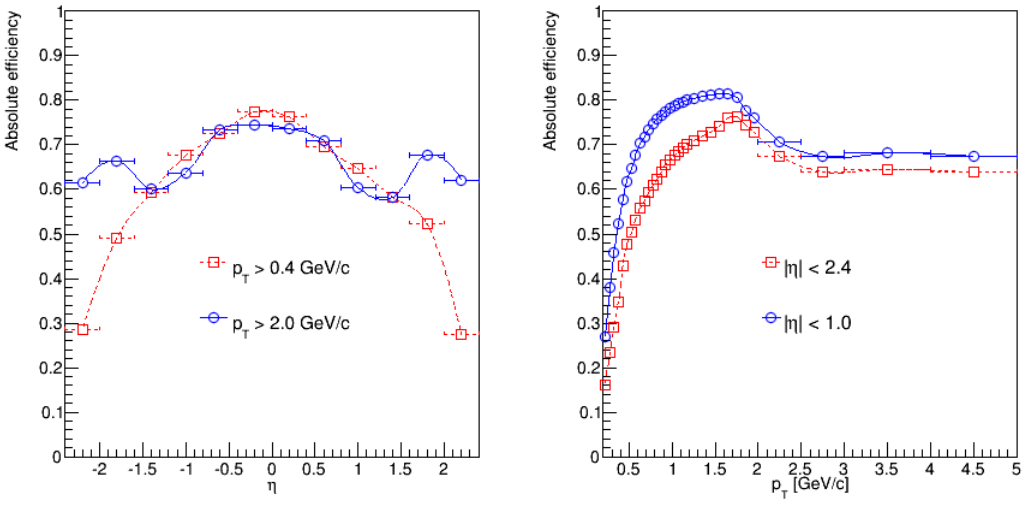

Figure 5.2: Tracking efficiency as functions of η and p_T for the new "hiGeneralAndPixelTracks" in the 2011 dataset.

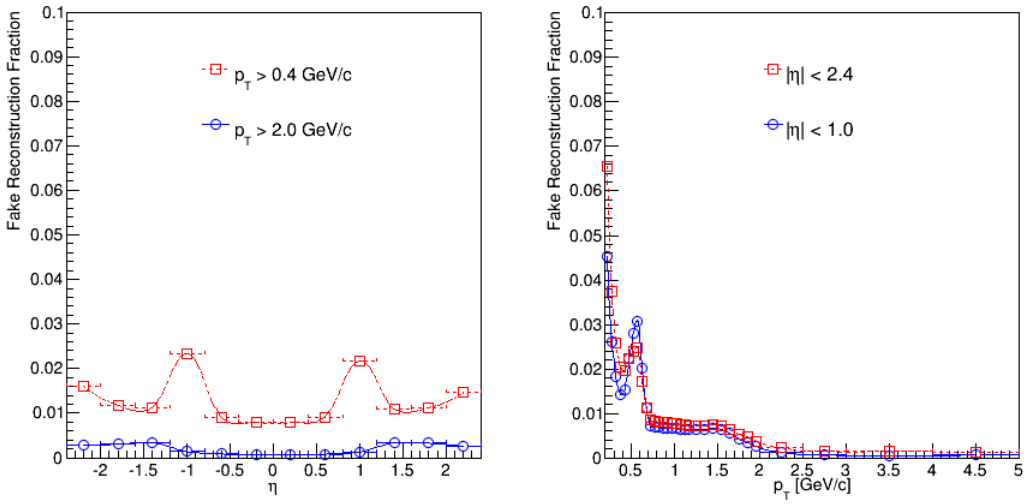

Figure 5.3: Fake rate as functions of η and p_T for the new "hiGeneralAndPixelTracks" in the 2011 dataset.

These efficiency correction factors will be used at the end of each flow analysis in order to correct the extracted flow value at each p_T or η bin by the appropriate amount.

5.2 Event Plane Method Systematics

5.2.1 Contribution of Fake Tracks

There is an innate trade off in between tracking efficiency and fake rate. If one accepts every track regardless of its χ^2 value of course there will be a 100% tracking efficiency, however the fake rate will explode. To compensate, an optimal balance between the tightness of cuts and the trade off with efficiency must be sought. The end result in every CMS analysis thus far has been that there are still remaining

reconstructed fake tracks.

A resultant systematic error that one can estimate using a simulation is how much those fake tracks contribute to your measured signal. In Fig. 5.4 this is exactly what has been done for the $v_1^{odd}(\eta)$ measured using the CMS HF. It should be noted that as of the writing of this thesis no simulation has a v_1 signal built into it.

$\mathbf{v_1}(\eta)$

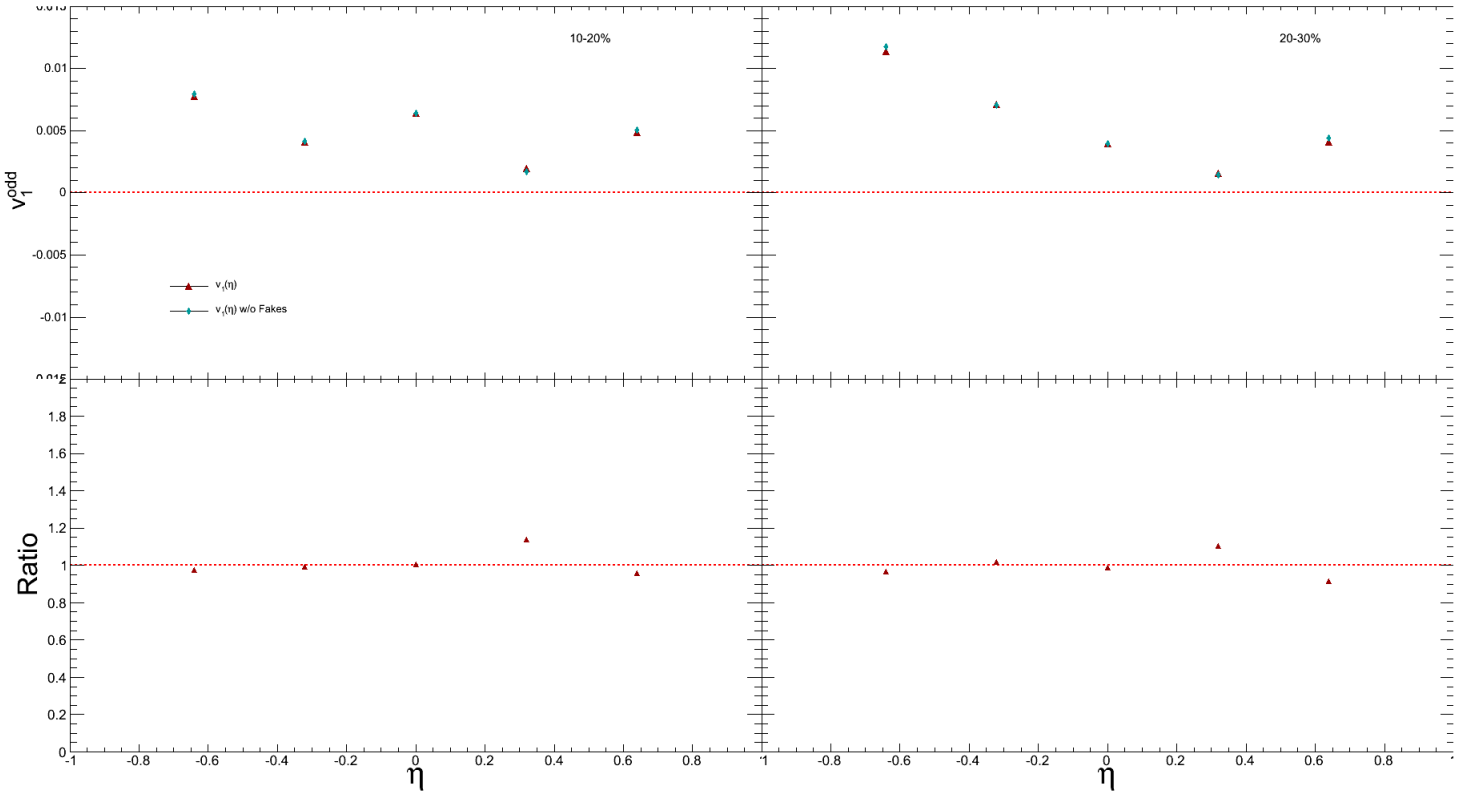

Figure 5.4: The results of measuring $v_1(\eta)$ using an Event Plane calculated with the HF. The red triangles represent the v_1 that is measured when the fake tracks are still in the sample. The blue diamonds are the same measurement but when the sample has the fake tracks identified and removed.

This plot shows that for this specific measurement of $v_1^{odd}(\eta)$ there is very little effect on the measurement from the contribution of fake tracks. This is likely because the EP is calculated without using any track information. The fakes, representing less than 5% of the total tracks are randomly distributed in ϕ, which would yield a net zero contribution to the signal.

In Fig. 5.5, however, the ratio plot reveals a much stronger influence on the measured signal from the contribution of fake tracks for the v_1^{even} measurement.

$\mathbf{v_1^{even}\,(p_T)}$

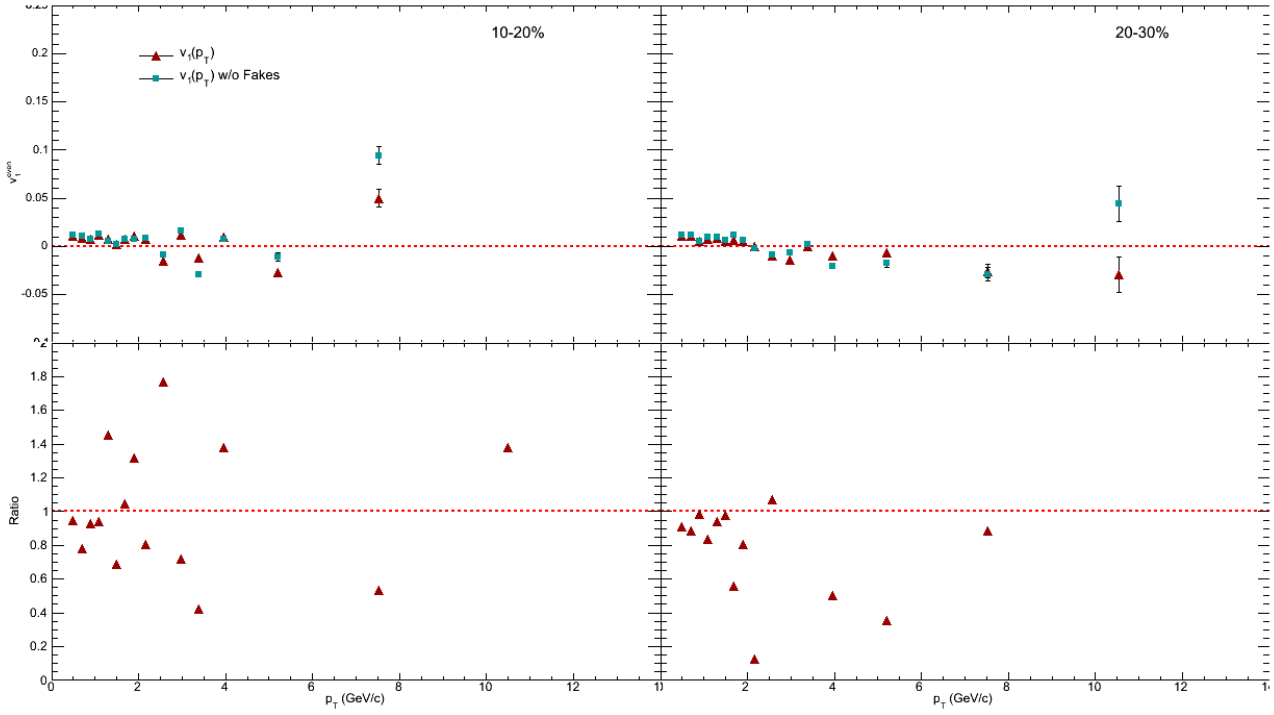

Figure 5.5: The results of measuring $v_1^{even}\,(p_T)$ using an Event Plane calculated with the tracker. The red triangles represent the v_1 that is measured when the fake tracks are still in the sample. The blue diamonds are the same measurement but when the sample has the fake tracks identified and removed.

When the tracker is used for the EP, the plot reveals to us that while still relatively small, there is a non-negligible difference between the v_1^{even} measured with and without the fake tracks. A likely explanation for this can be seen in Fig 5.3. In the left panel one can see that for particles located on the outer regions of the tracker there is a higher fake rate than for those located near the center of the barrel. The EP for this measurement is located in the region $1.4 < |\eta| < 2.4$. Combined with the

fake rates for low p_T tracks around the edges of our measurement $|\eta| < 0.6$ this is a likely cause for the high fake rates. This discrepancy is a main source of systematic error that will be shown in the Sec 5.3.

5.2.2 EP Resolution

In Eq. 4.9 it was described how EP resolutions are a key component to any measurement that uses the Event Plane method. Figure 5.6, shows the Event Plane resolution for the HF measurement of Ψ_1^{odd}.

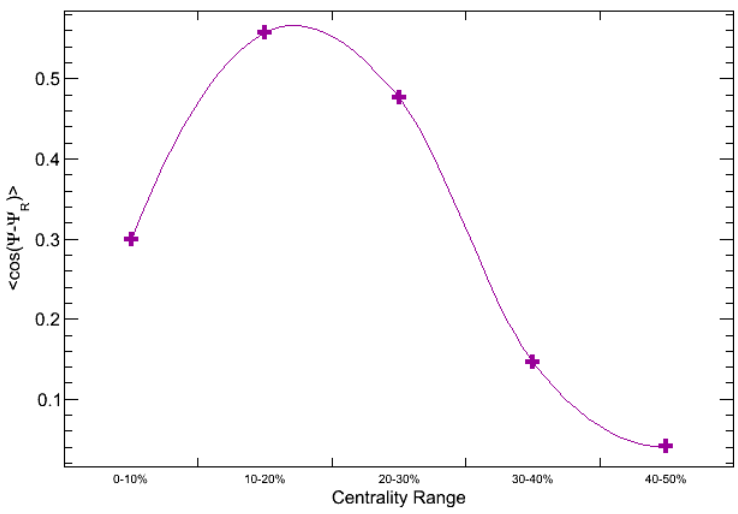

Figure 5.6: The Event Plane Resolution of Ψ_1^{odd} using the Forward Hadronic Calorimeter. A clear centrality dependence can be seen and has been applied to the corresponding v_1 measurement.

The EP resolution centrality dependence is likely due to detector asymmetry for the more central bins. In the more peripheral bins the low resolution is more likely caused by low occupancy. It should also be noted that the HF EP resolution had improved between 2010 and 2011, likely due to improved reconstruction of hits.

Tracker Event Plane Resolution

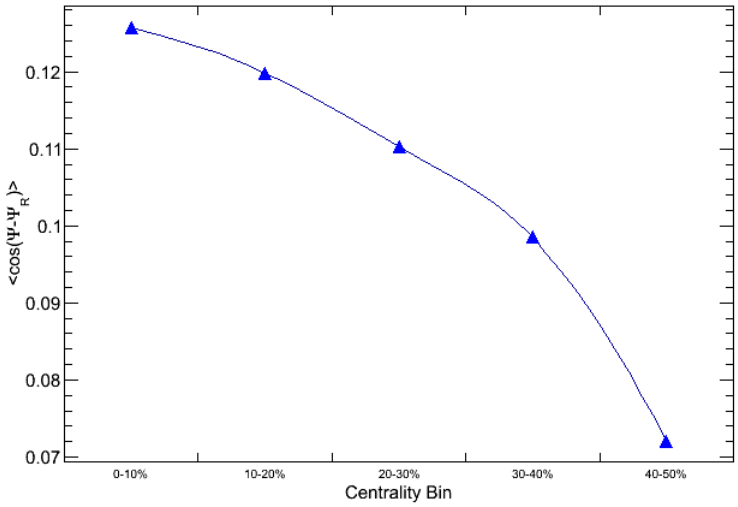

Figure 5.7: The Event Plane Resolution of Ψ_1^{even} using the outer regions of the tracker $|\eta| > 1.4$. The various values shown have been applied to the corresponding v_1.

In the tracker the resolution is more predictable with respect to centrality. In the more central bins there are more tracks, which means more information for the measurement. The resolution decrease as the number of tracks decreases along with the percent overlap of the colliding nuclei. There was a noted decrease in

EP resolution between 2010 and 2011 running due to the deterioration of various segments of the CMS tracker.

5.2.3 Primary Vertex Position z± 5cm

Another potential source of error in the measurement is the shifting of the primary vertex. It was discussed above that only events with a primary vertex position of $|z| < 10$ cm with respect to the nominal center of CMS were selected. The results of two subsets of the data showing the effect of selecting different vertex positions, $|z| < 5$ cm and $|z| < 7$ cm are shown in Fig. 5.8 and Fig. 5.10 respectively.

$\mathbf{v_1^{odd}}\,(\eta)$

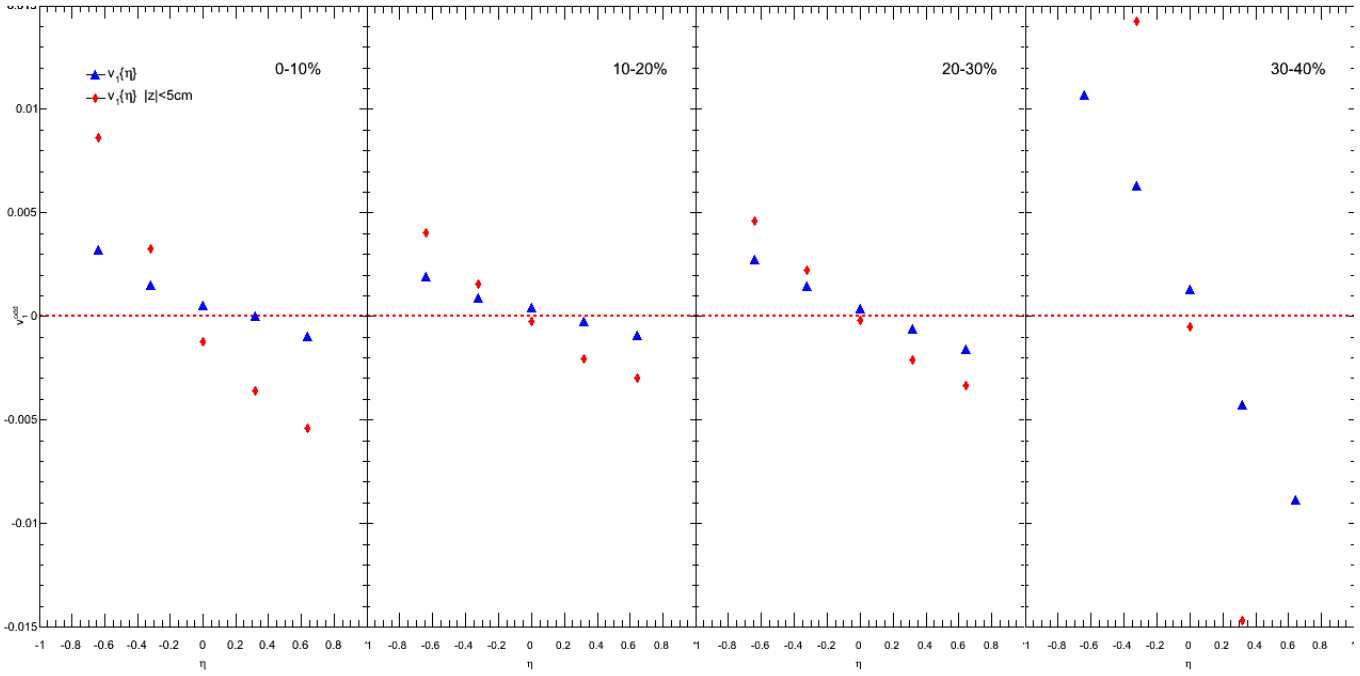

Figure 5.8: v_1^{odd} measured with the HF Event Plane. The blue triangles show the measurement accepting all primary vertex positions ($\pm$ 10 cm) in the dataset. The red diamonds show the result when only events with a primary vertex position inside of 5 cm are analyzed.

Figure 5.8 shows a relatively large effect when the primary vertex is constrained to be tighter to the nominal zero position of the CMS detector. Also while constrained, the resulting v_1 shows a much more drastic dependence on centrality. These errors proved to be the primary source of systematic error for the measurement of v_1^{odd} and will be represented below in the results.

$\mathbf{v_1^{even}\,(p_T)}$

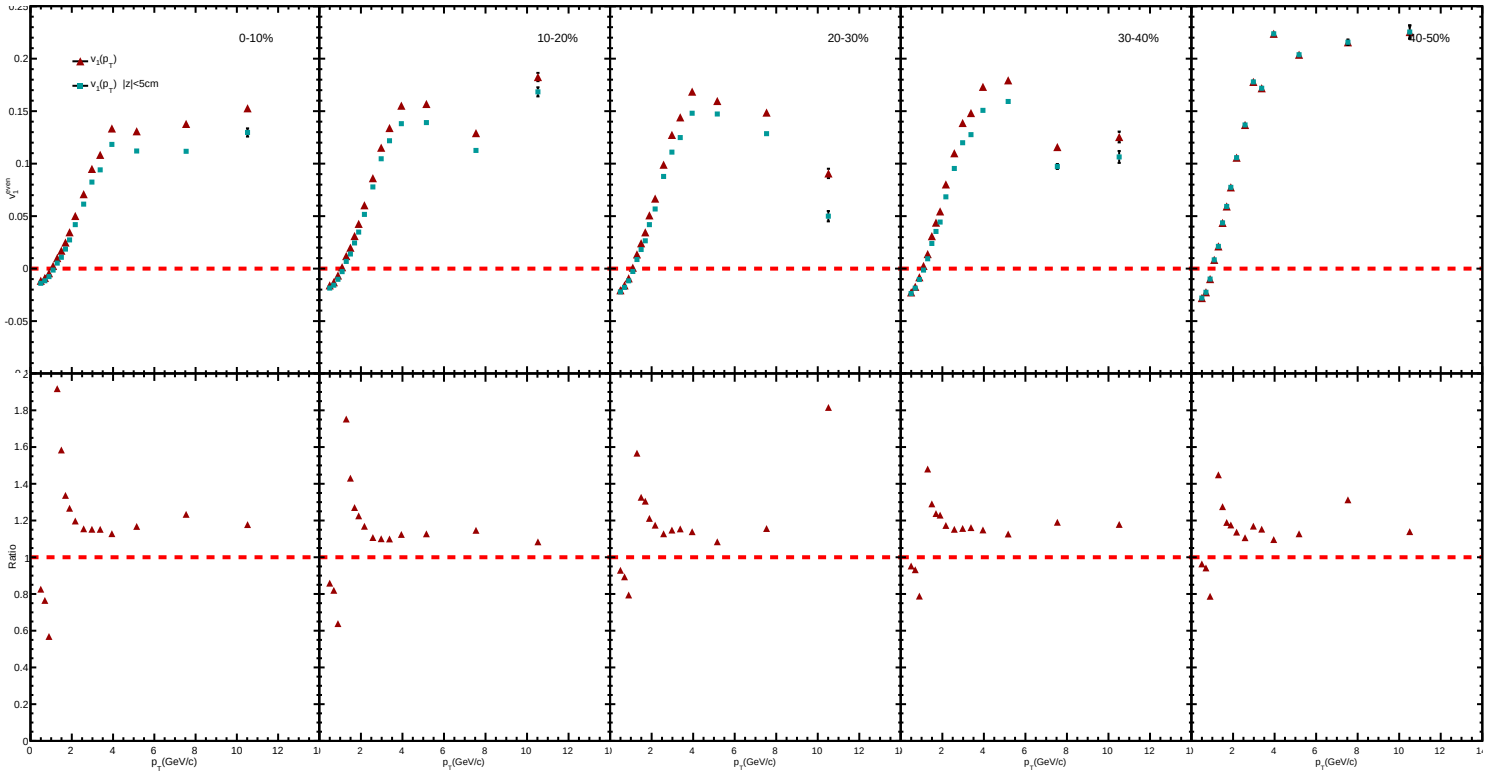

Figure 5.9: v_1^{even} measured with the tracker Event Plane. (upper panel) The red triangles show the results of using all of the events in the dataset. The blue squares are the measured v_1 using only events with a primary vertex position of $\pm$ 5 cm to the nominal center of CMS. (lower panel) The red triangles represent the ratio.

In Figure 5.9 the centrality dependence is a lot less noticeable than for the measurement of v_1^{odd}. The larger ratio values at the lower p_T ranges are probably due to the better tracking abilities found the closer to the center of CMS.

5.2.4 Primary Vertex Position z± 7cm

$\mathbf{v_1^{odd}}(\eta)$

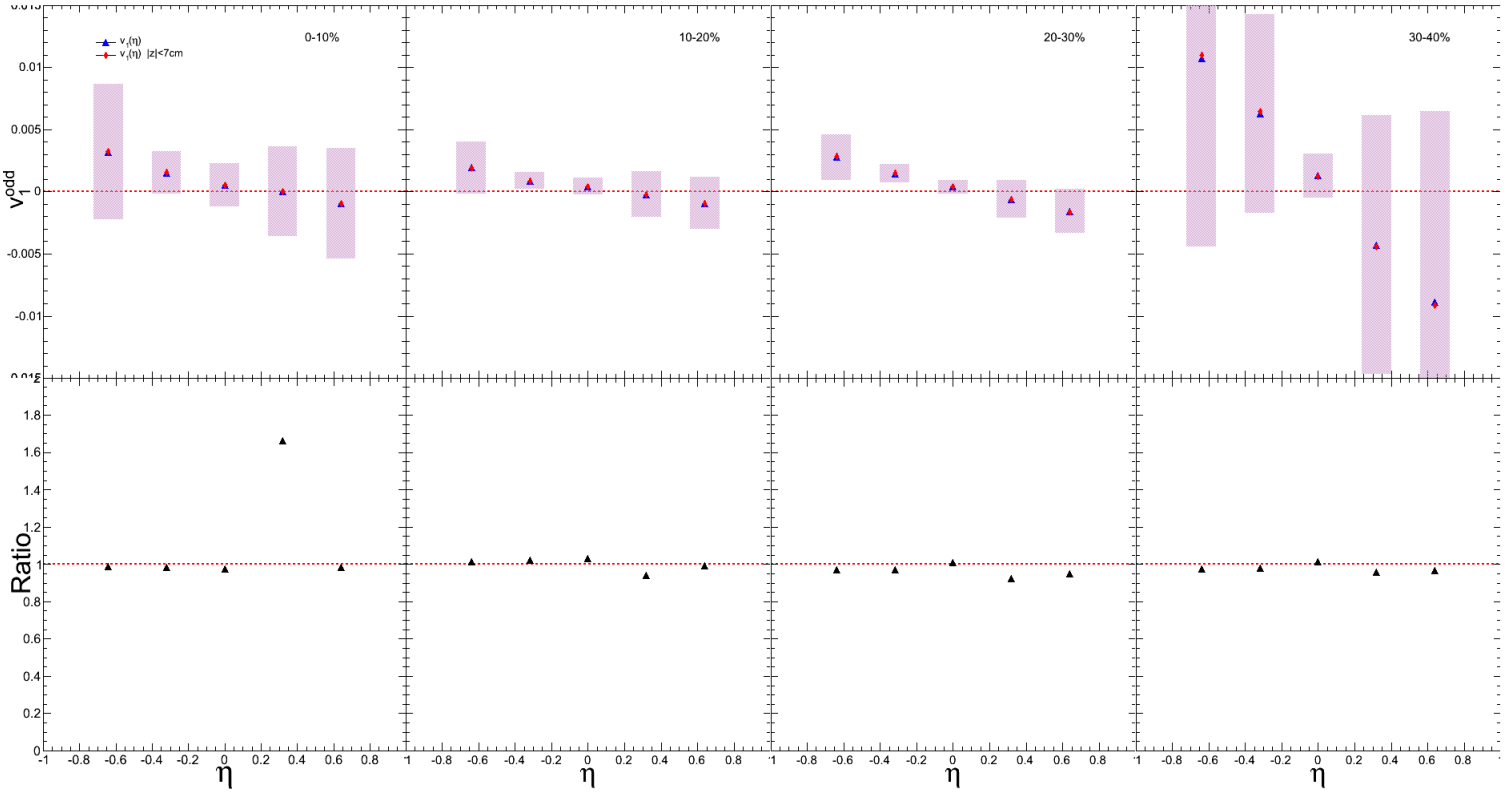

Figure 5.10: (upper panel)The blue triangles represent the v_1^{odd} measured with respect to the HF EP using the entire dataset. The red diamonds show the measurement repeated on only events that have a primary vertex position closer (± 7 cm) to the nominal center of CMS. The ratio of the two is shown in the lower panels.

In Figure 5.10 the agreement across centrality ranges is not overly surprising as the cuts are approaching using the entire dataset again. However this also suggests that there is a strong dependence of E_{total} deposited in the various HF's depending

on position of the primary vertex. This discrepancy is understood as only detector efficiency which is highlighted by Fig. 5.24.

$\mathbf{v_1^{even}\,(p_T)}$

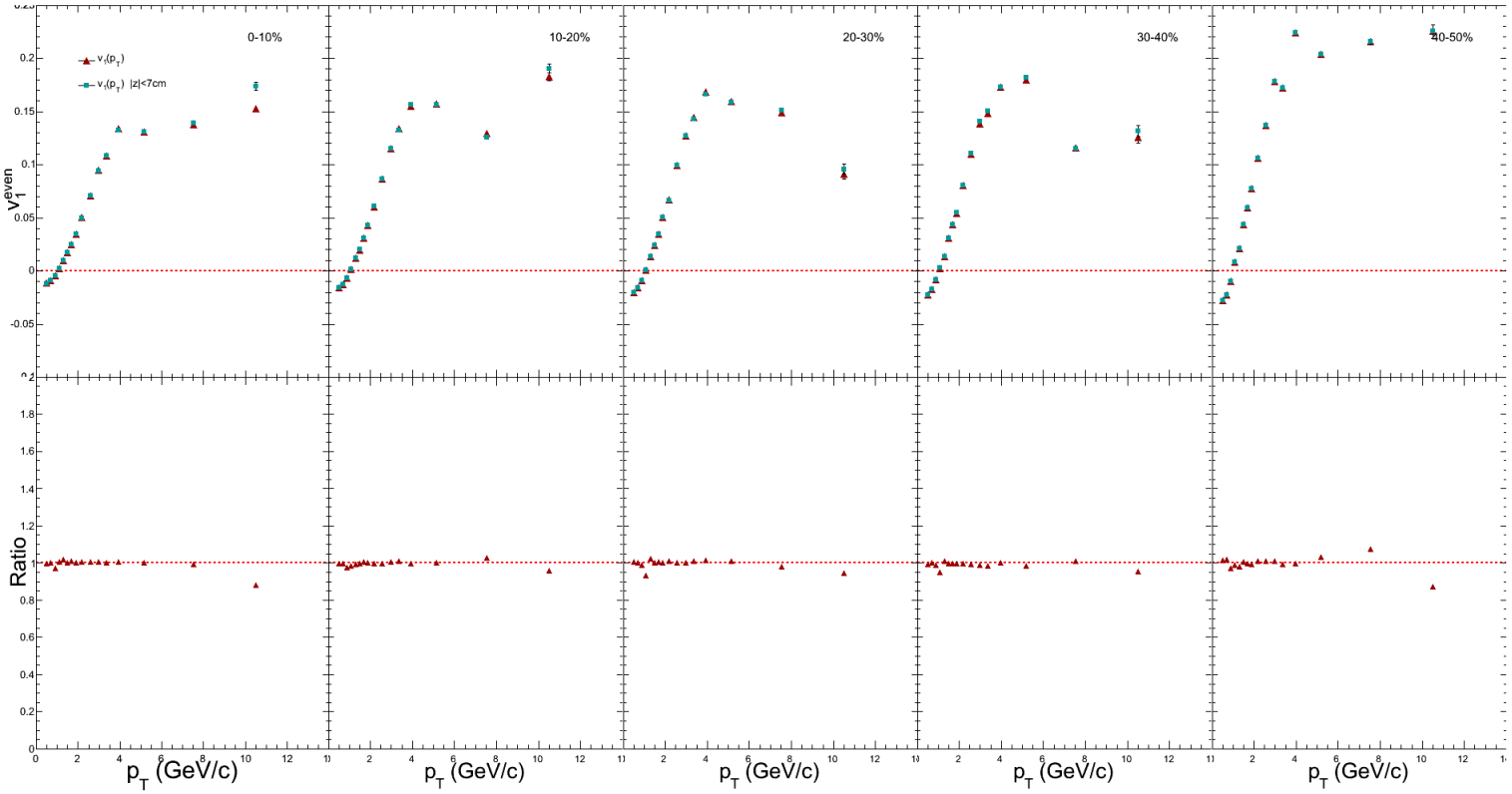

Figure 5.11: (upper panel) The red triangles represent the v_1^{even} measured using the entire dataset. The blue squares represent the same measurement repeated on only the events whose primary vertex is less than 7cm away from the nominal center of CMS. (lower panel) The ratio of the two datasets is shown for reference.

Figure 5.11 shows a near perfect agreement across all p_T ranges and centrality ranges. This agreement reveals that there is indeed a tracking discrepancy between

collisions very close to the middle of CMS and those that are not. These differences however are not as drastic as the differences seen in the v_1^{odd} measurements.

5.2.5 $\rho\pm$ 0.09 cm

The last systematic check preformed for this analysis to date has been to make a cut on the transverse distance from the primary vertex to the beam line. This parameter denoted ρ is defined as:

$$\rho = \sqrt{(x_{vertex} - x_0)^2 + (y_{vertex} - y_0)^2}, \tag{5.1}$$

where x_{vertex}, y_{vertex} are the reconstructed x and y positions of the primary vertex, and x_0, y_0 are the center of the CMS detector. This parameter seems to be of special significance for this analysis because if the primary vertex is located more to one side of the CMS tracker in azimuth this could lead to an anisotropy of reconstructed charged particles without it meaning anything useful to the physics trying to be measured.

$\mathbf{v_1^{odd}}(\eta)$

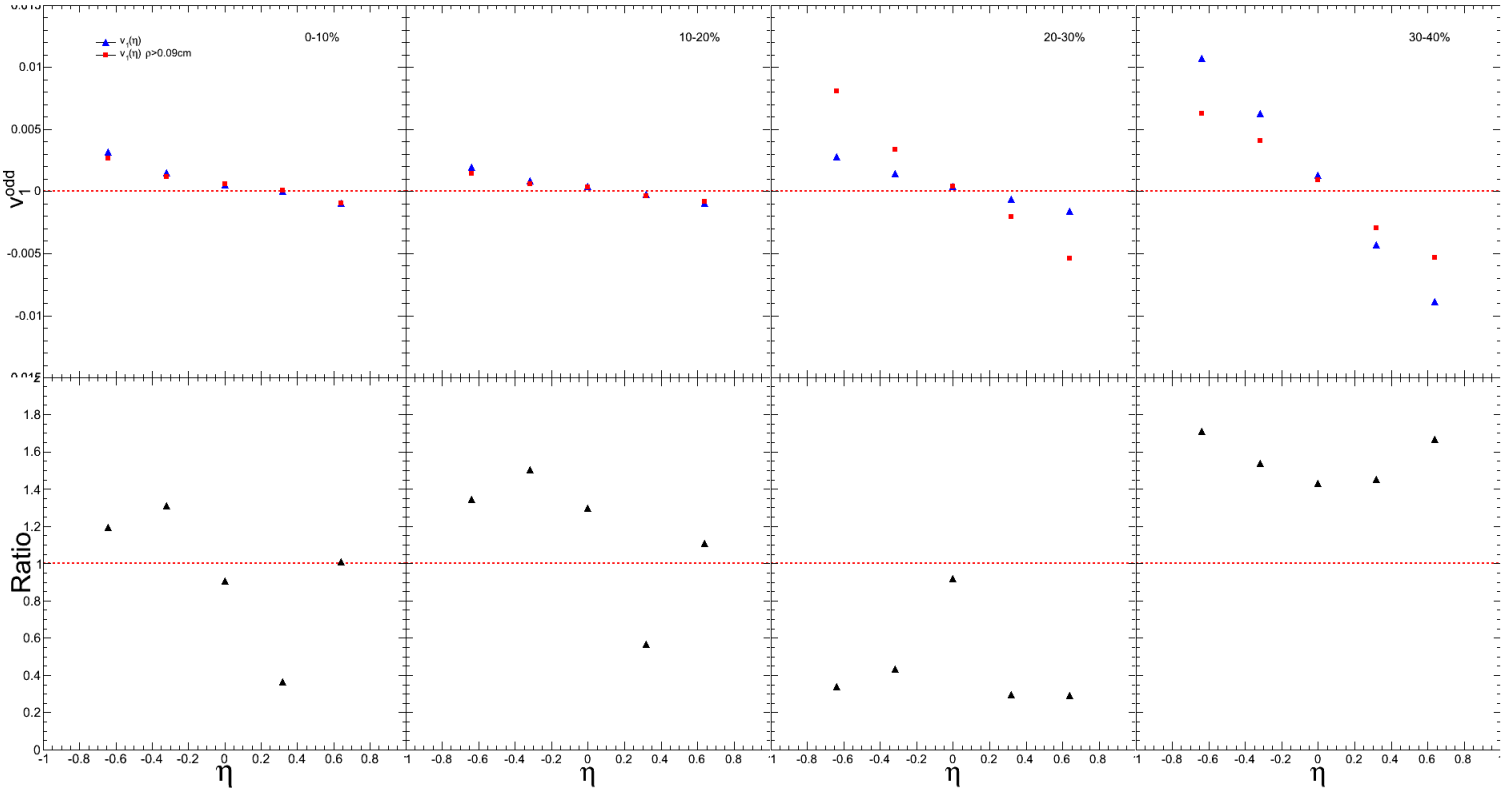

Figure 5.12: (upper panel) The blue triangles represent the v_1^{odd} measurement using all events. The red squares are the same measurement repeated only on events whose primary vertex is $\rho > 0.09$ cm away form the nominal center of CMS. (lower panel) The ratio of the two plots is shown for reference

In Figure 5.12 the effect of a transversely displaced primary vertex is shown. A similar random effect can be seen in the more central bins, but no general conclusions are drawn about the source of this. The results are noted as another source of systematic error for the v_1^{odd} measurement in the subsequent chapter.

$\mathbf{v_1^{even}\,(p_T)}$

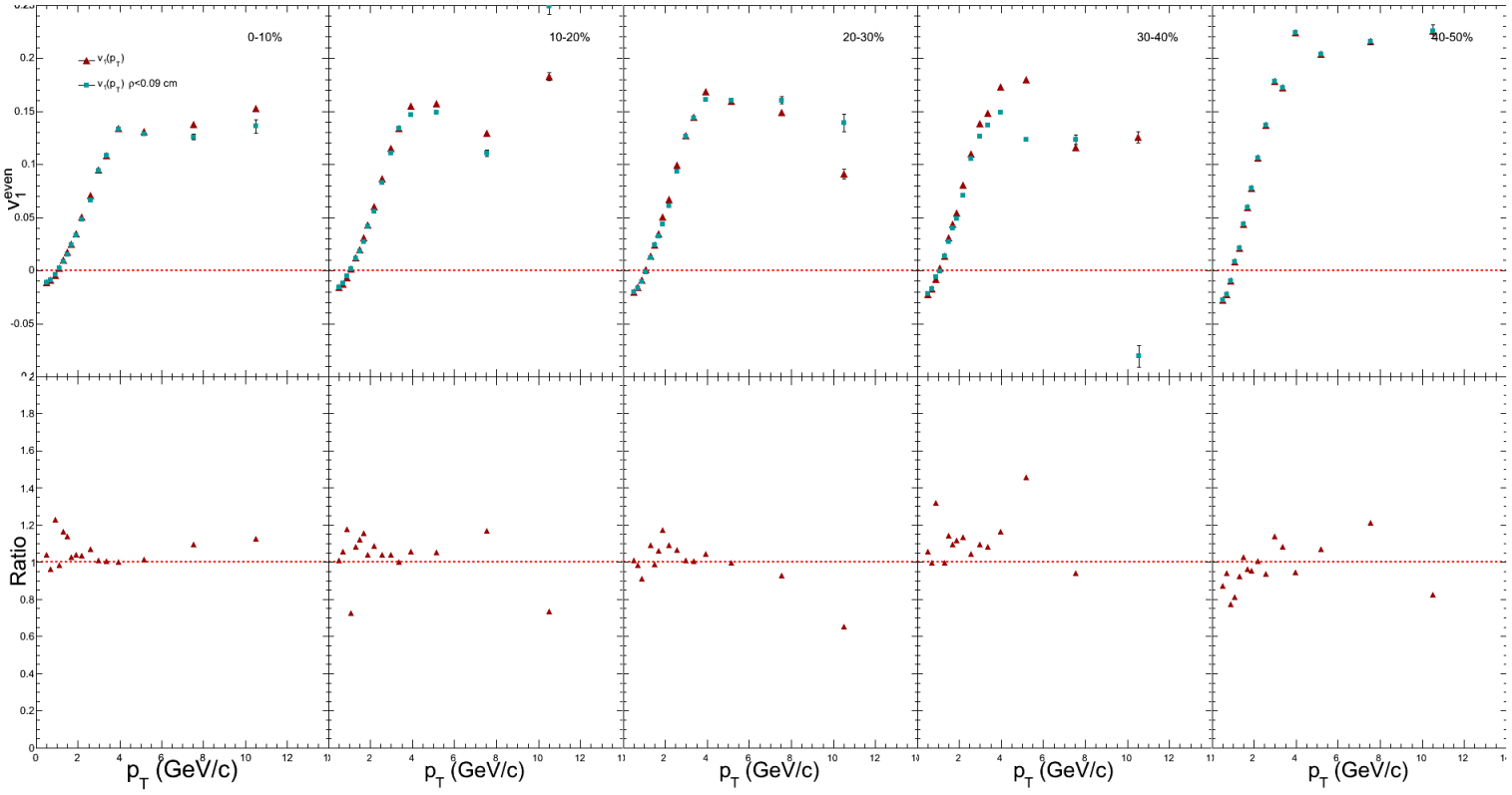

Figure 5.13: (upper panel) The red triangles represent the measurement of v_1^{even} using the entire dataset. The blue squares represent the same measurement repeated on only events whose transverse distance are **closer** to the nominal center of CMS than 0.09 cm. (lower panel) The ratio of the two results are shown for reference

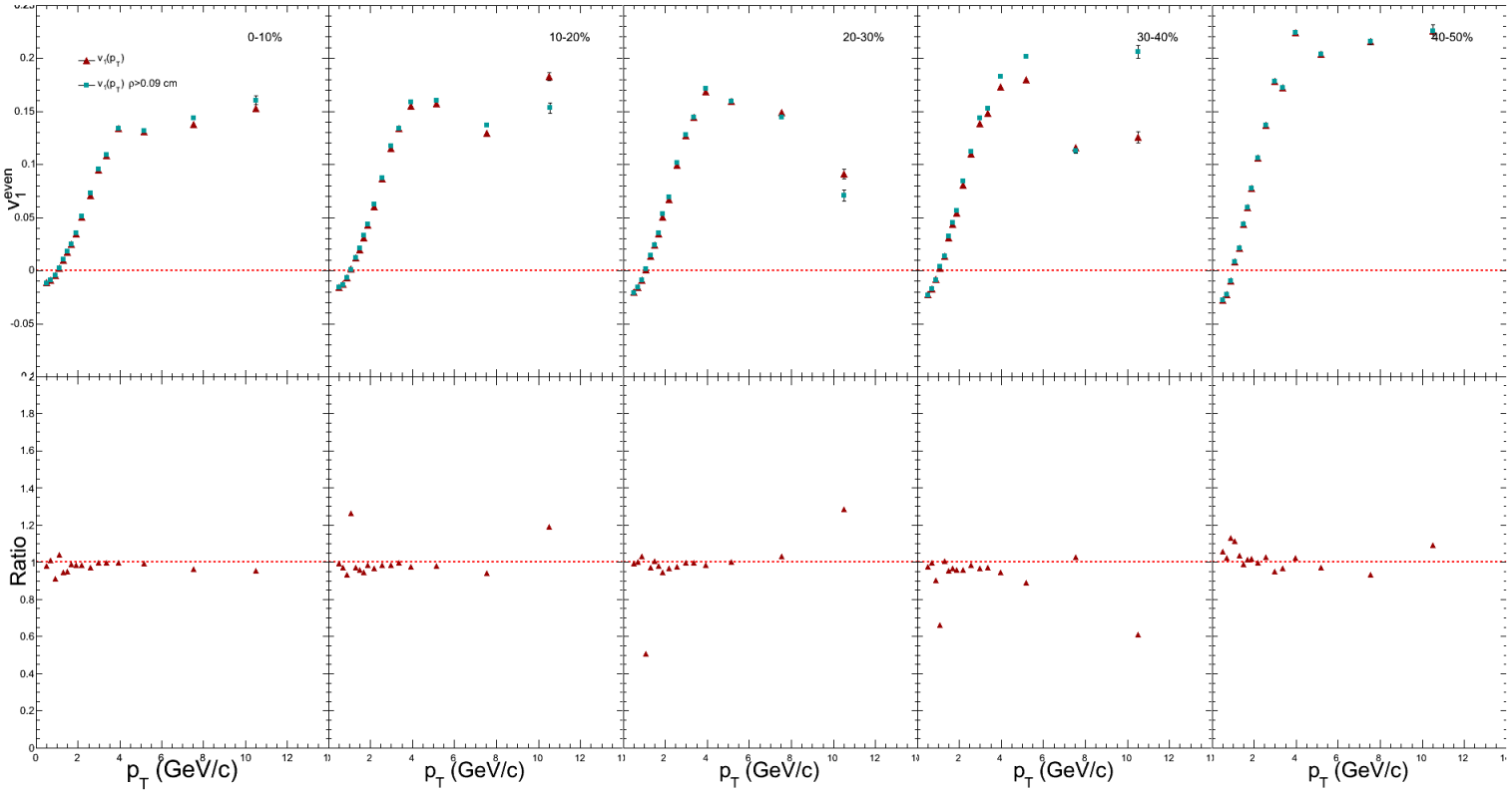

Figure 5.14: (upper panel) The red triangles represent the measurement of v_1^{even} using the entire dataset. The blue squares represent the same measurement repeated on only events whose transverse distance are **farther** from the nominal center of CMS than 0.09 cm. (lower panel) The ratio of the two results are shown for reference.

In Fig. 5.13 and in Fig. 5.14 there is not a strong dependence of v_1^{even} on the transverse position of the primary vertex. The effect is slightly greater for events that are closer to the nominal center of CMS, likely due to more low-p_T charged particles being reconstructed isotropically in the detector.

5.3 Results

5.3.1 $\mathbf{v_1^{odd}}(\eta)$

5.3.1.1 Special Weights for HF Event Plane

The weights for v_1^{even} put forward by J.Y. Ollitrault [34] claim to remove effects from conservation of momentum and also non-flow effects. However, HF being a calorimeter, p_T information is not available. In oder to try and replicate this a naive attempt was made at constructing modified weights for Ψ_1^{odd} in the following way

$$X_n = \sum_i \left(E_T^i - \frac{\langle E_T^2 \rangle}{\langle E_T \rangle} \right) cos\left(n\phi_i\right), \tag{5.2}$$

$$Y_n = \sum_i \left(E_T^i - \frac{\langle E_T^2 \rangle}{\langle E_T \rangle} \right) sin\left(n\phi_i\right), \tag{5.3}$$

where $\langle E_T^2 \rangle, \langle E_T \rangle$ are the average transverse energy squared and average transverse energy deposited in the HF, respectively. These are calculated separately for the different centrality values presented in the analysis. Figure 5.15 shows the effect of using the modified weights on the creation of the event plane.

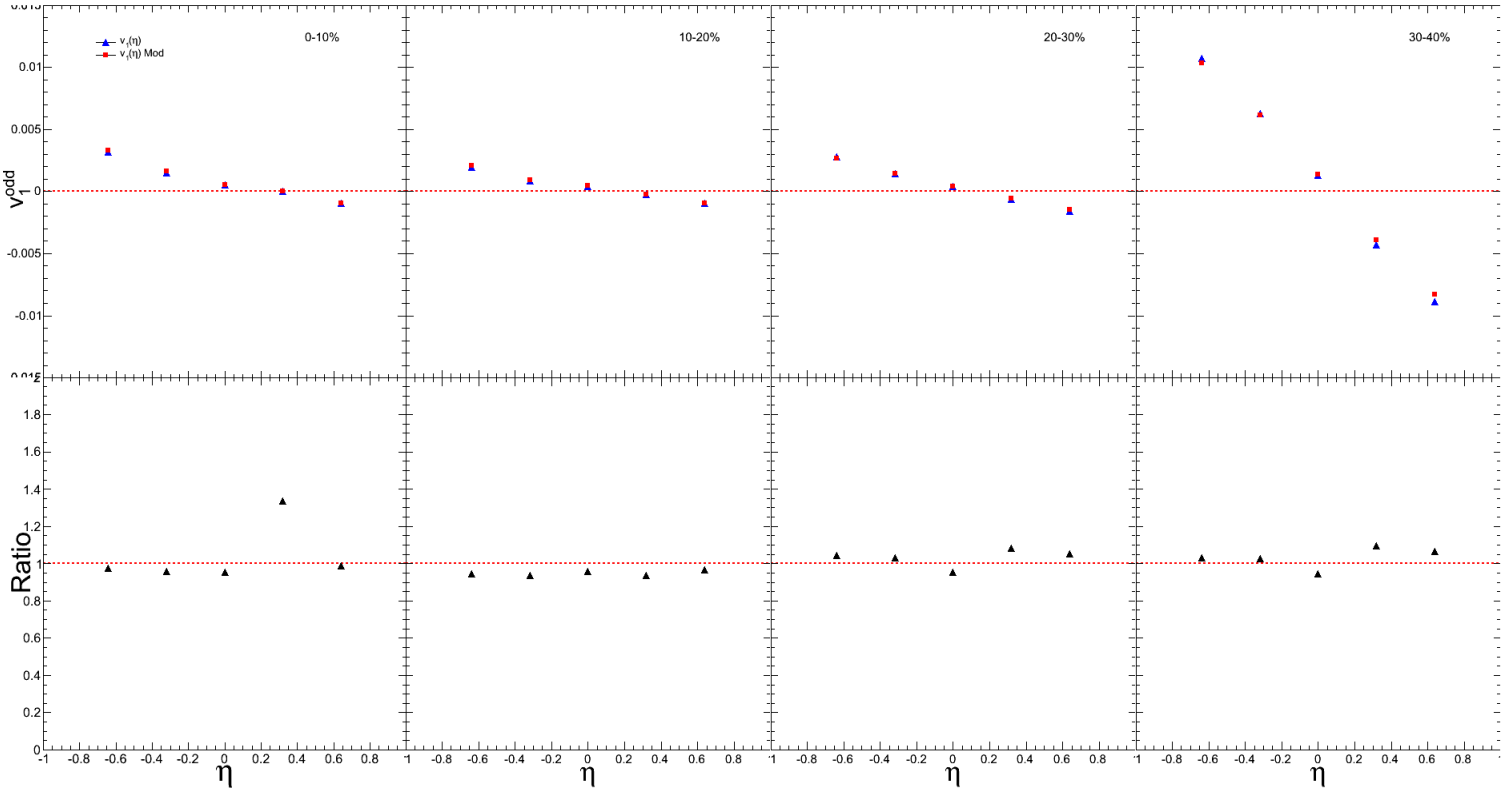

Figure 5.15: (upper panel) The blue triangles represent the standard v_1^{odd} using the HF event plane. The red squares represent the same analysis being done with the modified weights described in Eq. 5.2 and Eq. 5.3. (lower panel) The ratio of the two is shown for reference.

5.3.1.2 w/ Vertex Shifting Tests

As was done for the systematic uncertainties Figures 5.8 and 5.17 show the measured v_1^{odd} for events whose primary vertex are less than 5 cm and 7 cm away from the center of CMS respectively. The ratio shown is between the un-modified weights in blue triangles, and the modified weights in red squares.

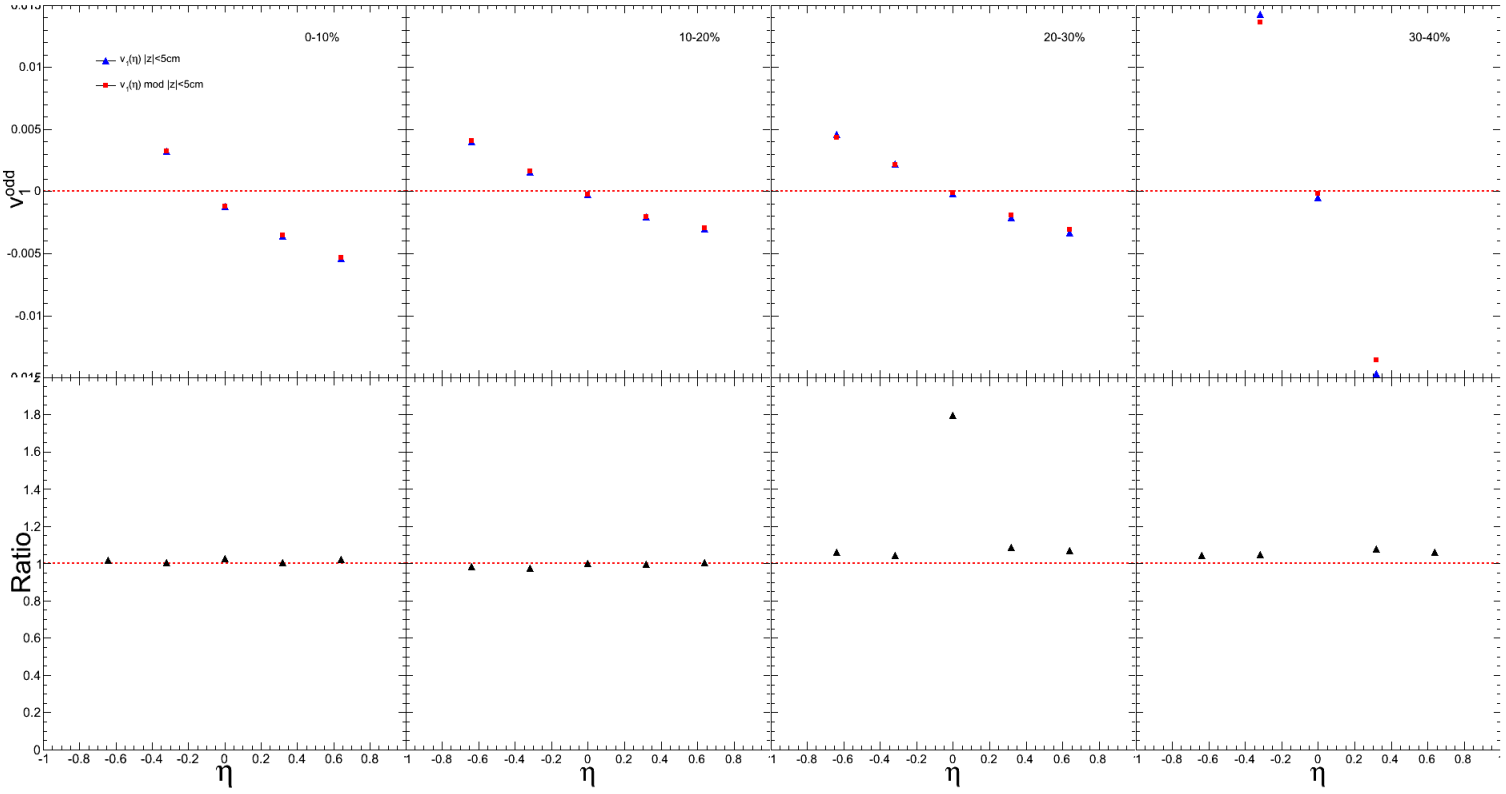

Figure 5.16: (upper panel) The blue triangles represent the standard v_1^{odd} using the HF event plane but only analyzing events where the primary vertex is less than 5 cm away from the nominal center of CMS. The red squares represents the same analysis being done with the modified weights described in Eq. 5.2 and Eq. 5.3. (lower panel) The ratio of the two is shown for reference.

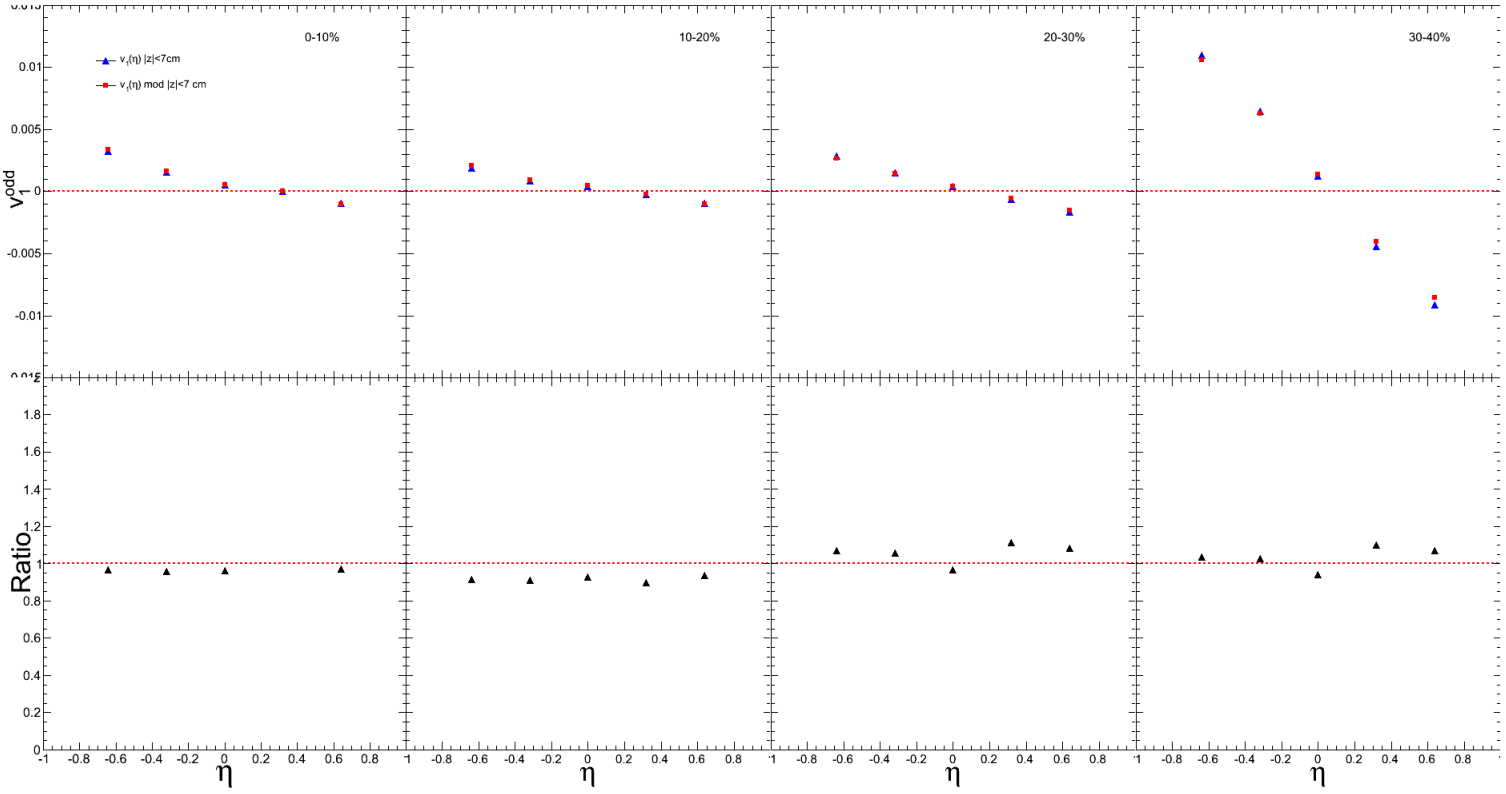

Figure 5.17: (upper panel) The blue triangles represent the standard v_1^{odd} using the HF event plane but only analyzing events where the primary vertex is less than 7 cm away from the nominal center of CMS. The red squares represents the same analysis being done with the modified weights described in Eq. 5.2 and Eq. 5.3. (lower panel) The ratio of the two is shown for reference.

Final $\mathbf{v_1^{odd}}$

The final measured v_1^{odd} with respect to pseudorapidity for the 2011 Heavy Ion run is shown in Figure 5.18. The systematic error shown is due to the beamspot tightness. The line shown is just to guide the eye and does not take into account the errors. Figure 5.19 shows the **magnitude** of the slopes from Fig. 5.18, the

centrality dependence of which is elaborated upon in the discussion section. Lastly, as a point of reference, in Figure 5.20, one can see the comparison between the v_1^{odd} measured in 2010 and 2011 Heavy Ion data taking. There are no systematic errors plotted for either year's data.

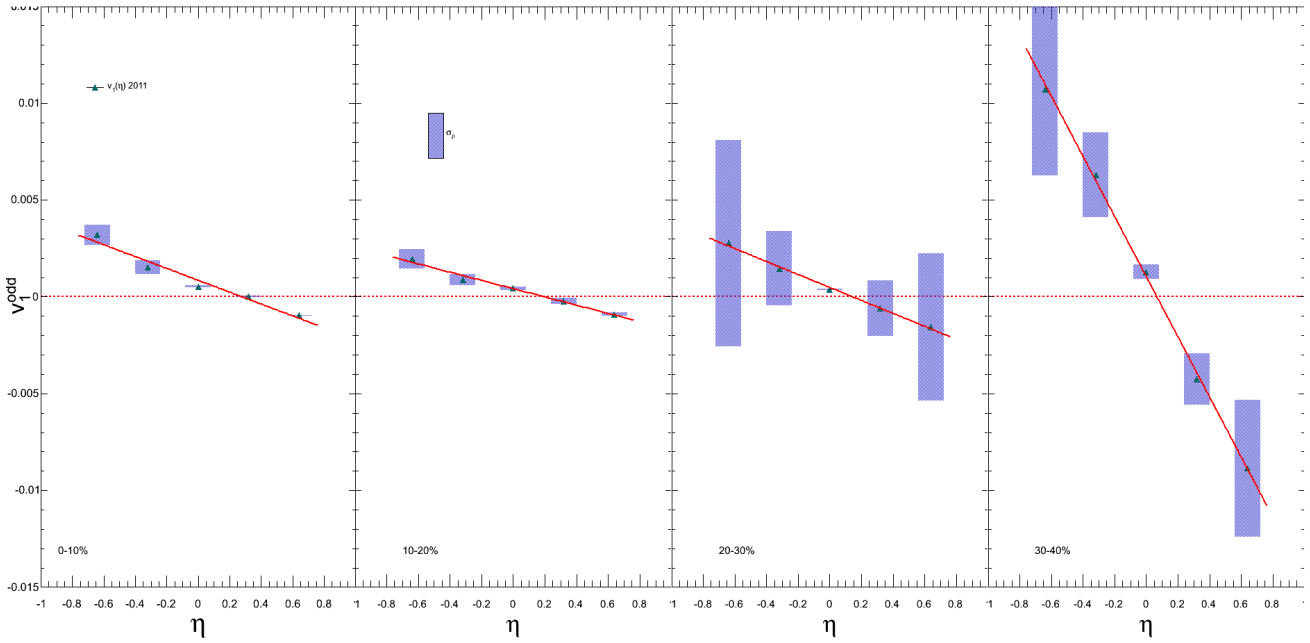

Figure 5.18: The final $v_1^{odd}(\eta)$ as measured by the HF Event Plane with both systematic errors and statistical errors shown. The red line is a simple linear fit used to both guide the eye and extract the magnitude of the directed flow.

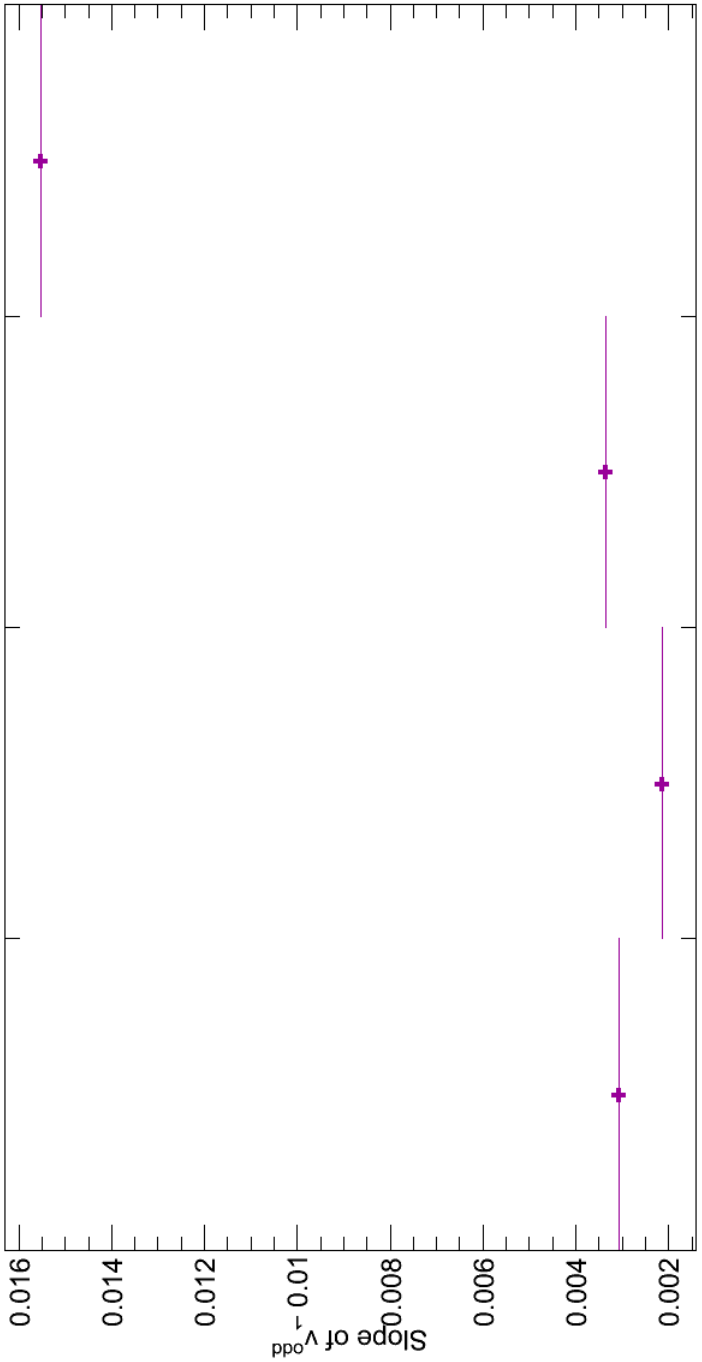

Figure 5.19: The extracted slopes from Figure 5.18 as a function of centrality.

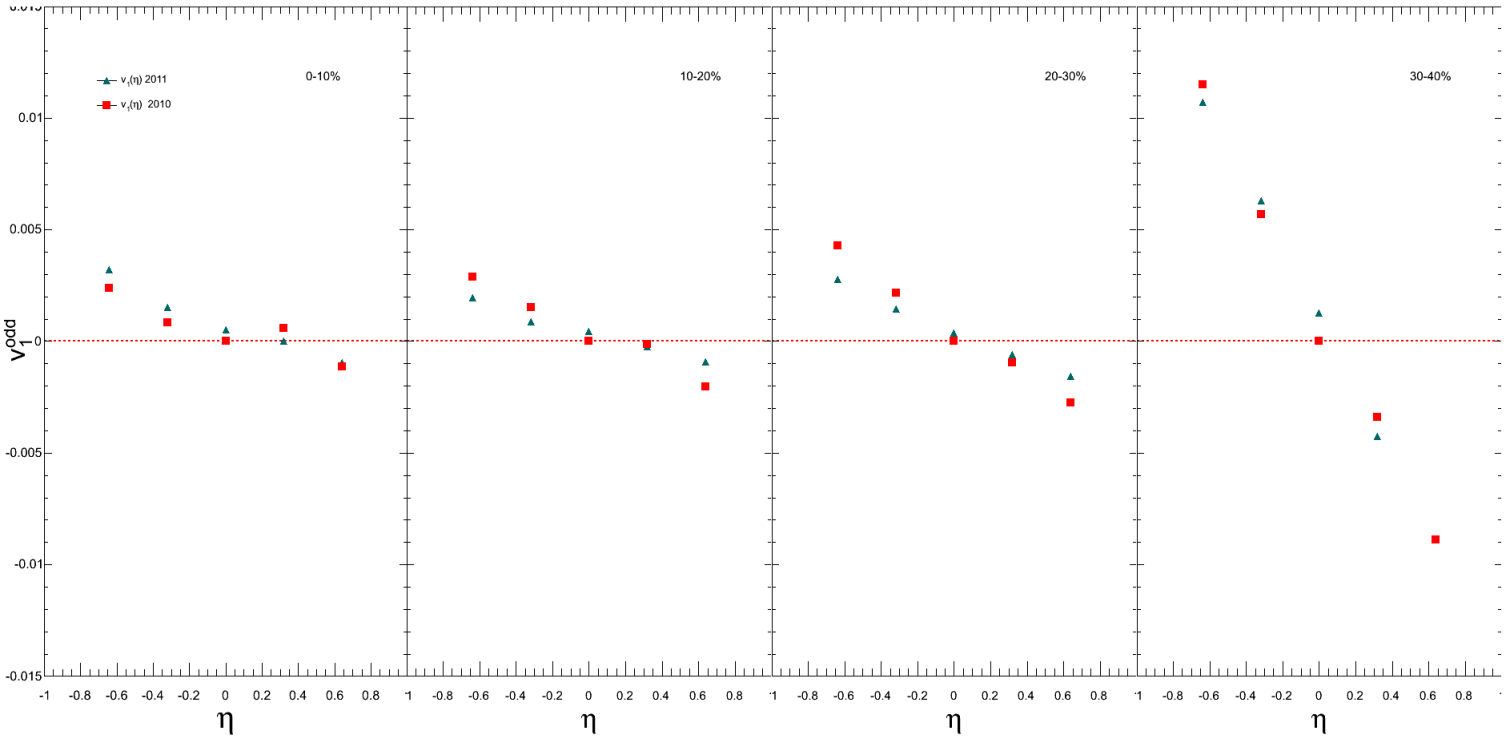

Figure 5.20: The blue triangles represent the v_1^{odd} measured using the 2011 MinBias data set. The red squares are the same analysis done on the 2010 MinBias dataset. Only statistical errors are shown.

5.3.2 $\mathbf{v_1^{even}(p_T)}$

Figure 5.21 is a histogram showing the v_1^{even} for the 2010 (red triangles) and 2011 (green squares) datasets. Their ratio is shown in the lower panel for reference, it should also be noted that no systematic errors are shown. Figure 5.22 is the final 2011 v_1^{even} measurement with all relevant systematic errors shown. Lastly, Figure 5.23 shows the 2010 v_1^{even} results as measured by the CMS experiment and the ATLAS experiment. The green and purple bands show the systematic errors for CMS, while the black band is the systematic error for the ATLAS measurement.

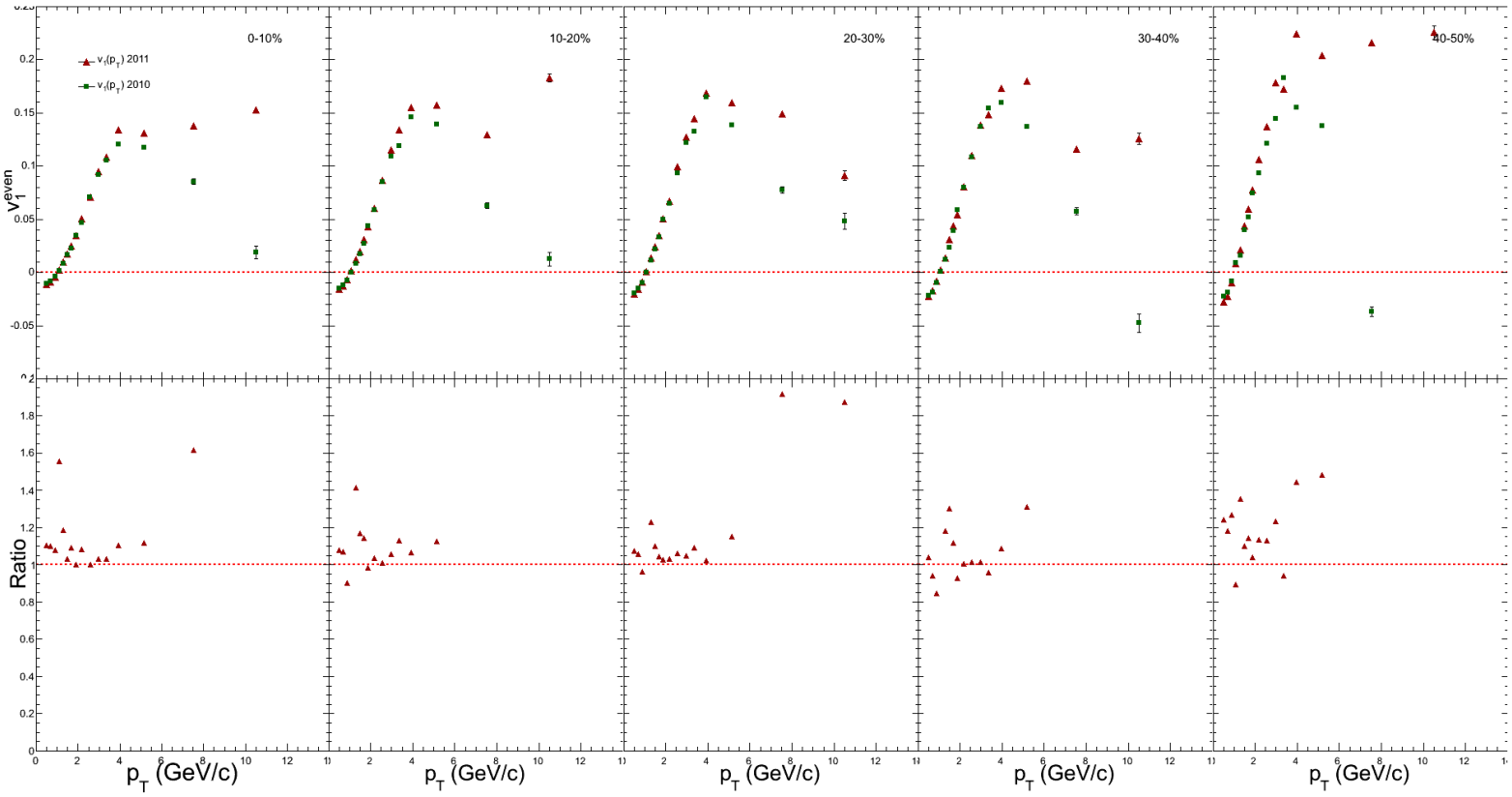

Figure 5.21: (upper panel) The red triangles are a measurement of v_1^{even} as a function of transverse momentum using the 2011 MinBias dataset. The green squares are the same analysis performed on the 2010 MinBias dataset. (lower panel) A ratio of the two measurements for reference. Only statistical errors are shown.

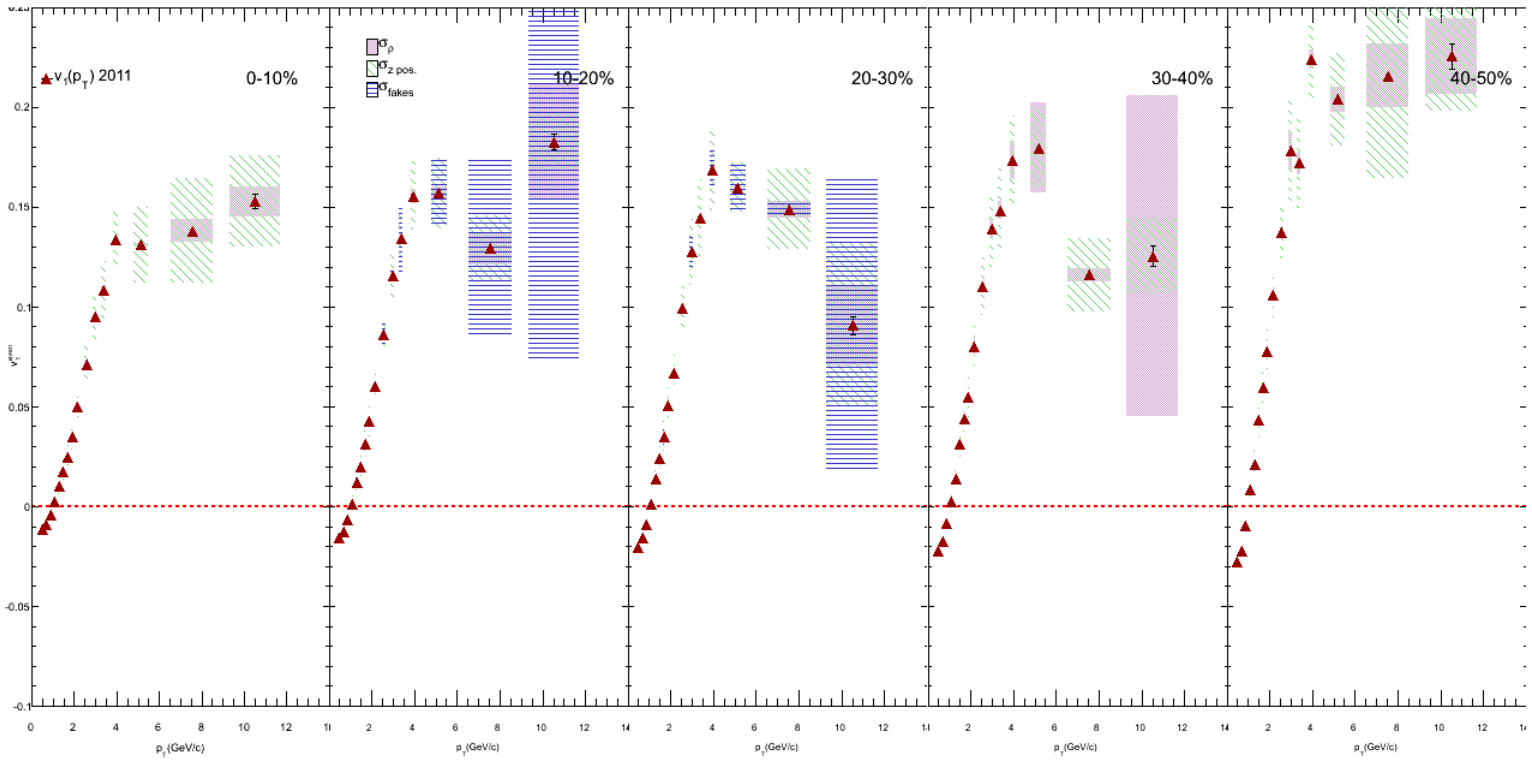

Figure 5.22: The final measurement of v_1^{even} as a function of transverse momentum with the three primary sources of systematic errors plotted.

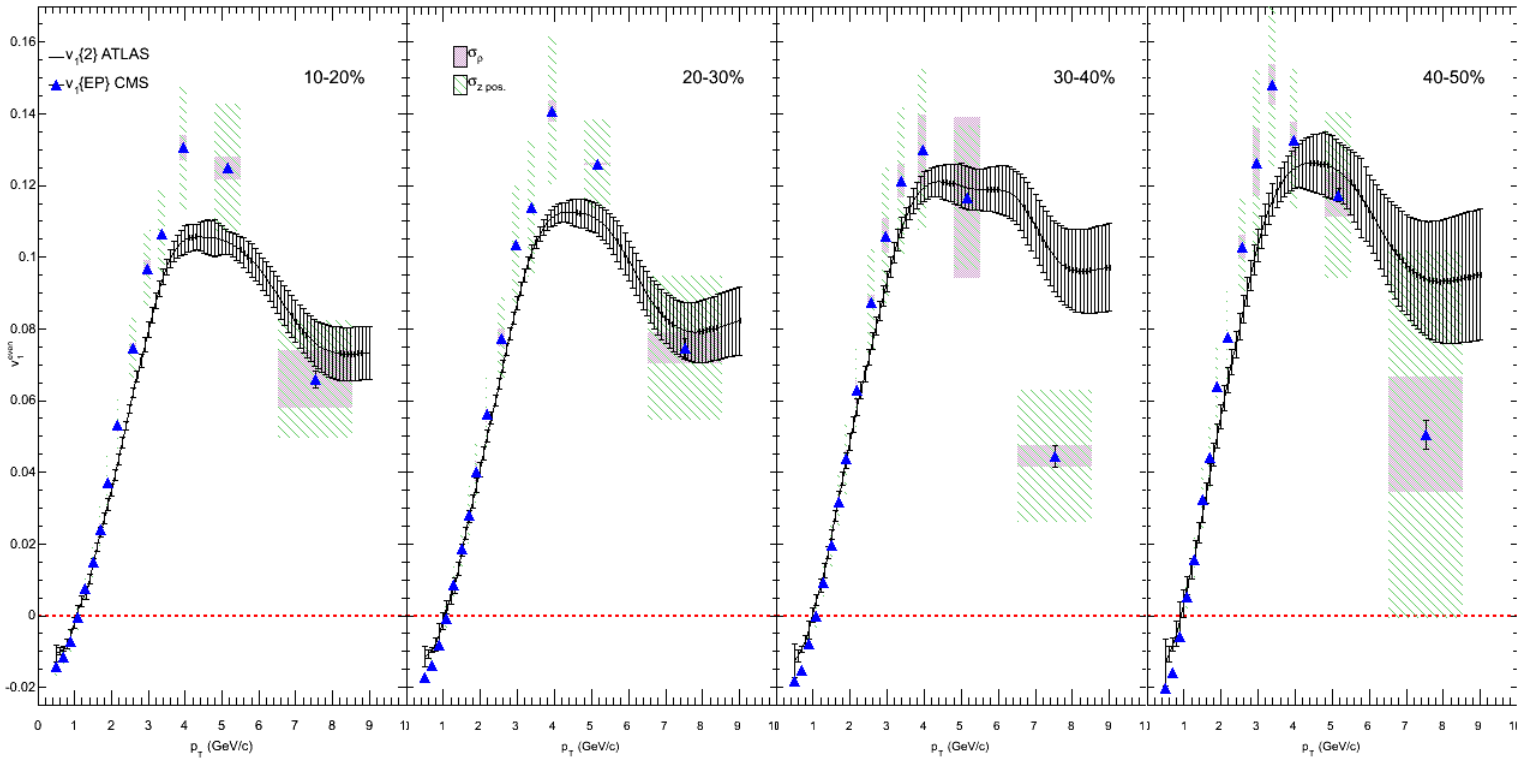

Figure 5.23: The blue triangles are the results (with systematic errors plotted) of the directed flow as a function of transverse momentum from CMS using the Event Plane method for the 2010 MinBias dataset. The line drawn with the error bars is the result from the ATLAS experiment [3] using the 2-particle cumulant method.

5.4 Discussion

A confounding result is seen by the discrepancy in Fig. 5.8. One might expect based on symmetry that the closer to the absolute middle of CMS the collision occurs, the more even the energy will be dispersed between the two sides of HF. This would yield a better EP resolution and subsequently a better v_1^{odd} measurement. However, in Figure 5.24, we see that for most centrality bins, the EP resolution is substantially worse.

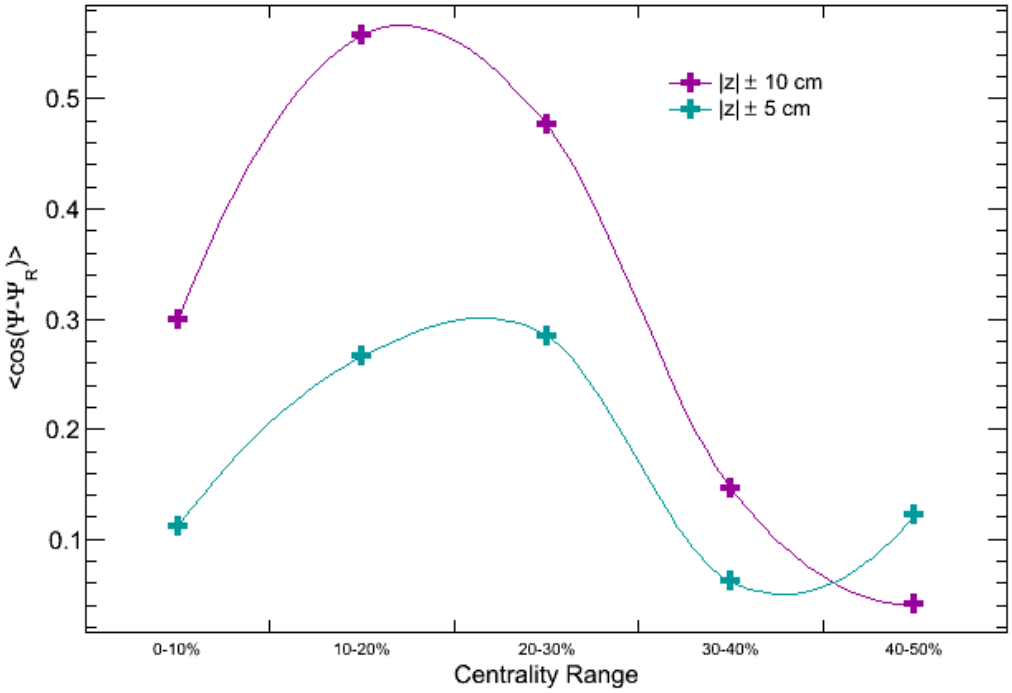

Figure 5.24: The purple circles correspond to the EP resolution seen in Fig. 5.6. While the blue data points and line correspond to only events that had a primary vertex position less than 5 cm away from the center of CMS.

This suggests that matter is primarily being created on one side of the collision leading to an energy asymmetry in the HF calorimeters in positive and negative pseudorapidity. Or more likely, there are dead channels in each HF which would lead to Event Plane information being lost in collisions. As a means to counteract this one could mask dead channels and replace them with the average of the neighboring channels.

In the results put forward in this thesis a clear centrality dependence is shown in Fig. 5.18 and Fig. 5.19. The most central bin from 0-10% is thought to be dominated, like v_1^{even} is, by dipole-like initial energy fluctuations [4]. As the collisions become more and more peripheral the sideward collective motion of the particles at non-zero pseudorapidity arises in part due to the initial tilt of the source, as shown in Fig. 1.8. Another interesting effect can be hinted at from this centrality dependence, and that is of a spinning medium. To confirm this, the measurement of v_1 must be made using a second order Event Plane, Ψ_2.

Figure 5.25 is a measurement of v_1^{odd} from the ALICE experiment.

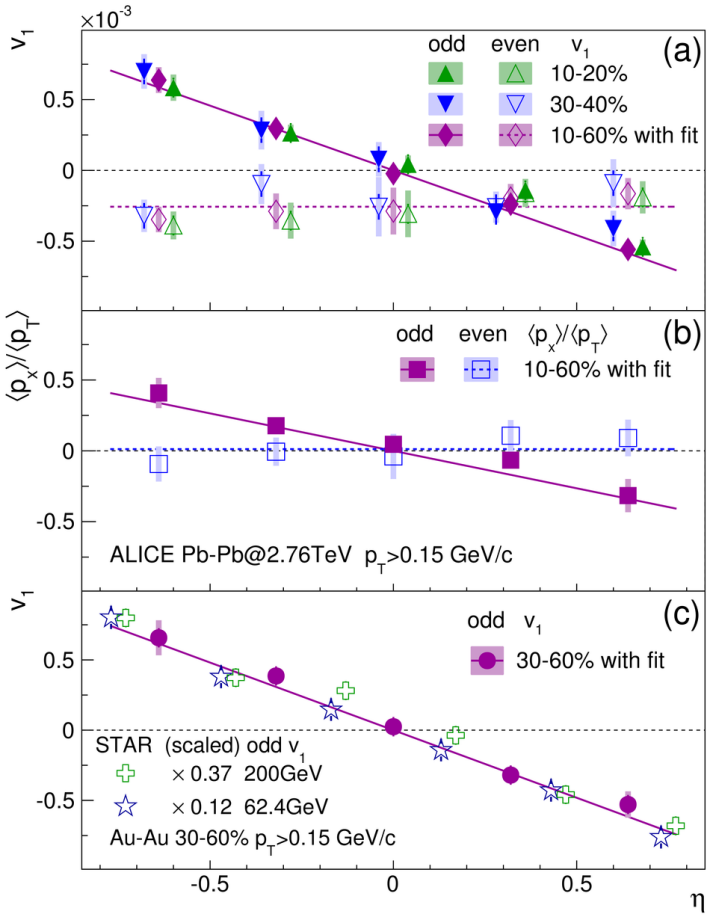

Figure 5.25: (a) v_1 and (b) $\langle p_x \rangle / \langle p_T \rangle$ versus psuedorapidity in Pb-Pb collisions at $\sqrt{s_{NN}} = 2.76$ TeV. (c) v_1^{odd} compared to the STAR data for Au-Au collisions at $\sqrt{s_{NN}} = 200(62.4)$ [5] GeV downscaled by a factor of 0.37 (0.12). The statistical (systematic) uncertainties are indicated by the error bars (shaded bands). Lines (to guide the eye) represent fits with a linear (constant) function for v_1^{odd} (v_1^{even}) [4].

In their result, the odd component of directed flow is about 1/6 of those measured by the CMS experiment. The reduced magnitude of v_1^{odd} was predicted to be smaller at the LHC because of the reduction of the aforementioned tilt in the x-z plane. However, the smaller tilt seen in the participant region near midrapidity did not

change the slope of $v_1^{odd}(\eta)$ as predicted in [20, 28].

Something worth noting, however, is the disagreement found between the ALICE result and other experiments in the past such as NA49 and STAR. In Figs. 5.26 and 5.27 there is a clear increase in the slope of $v_1^{odd}(\eta)$ found as one progresses from more central to more peripheral events.

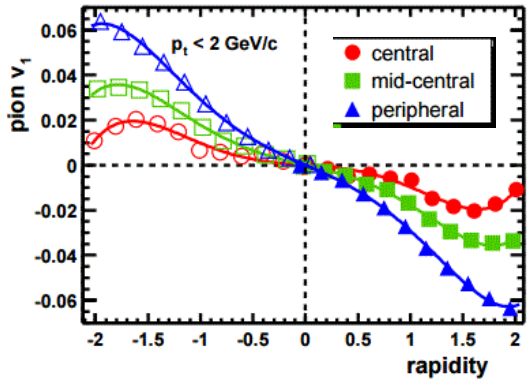

Figure 5.26: Standard directed flow as a function of rapidity for charged pions from 158A GeV Pb+Pb. three centrality bins shown. The open points in the graph have been reflected about midrapidity. Solid lines are polynomial fits. [12]

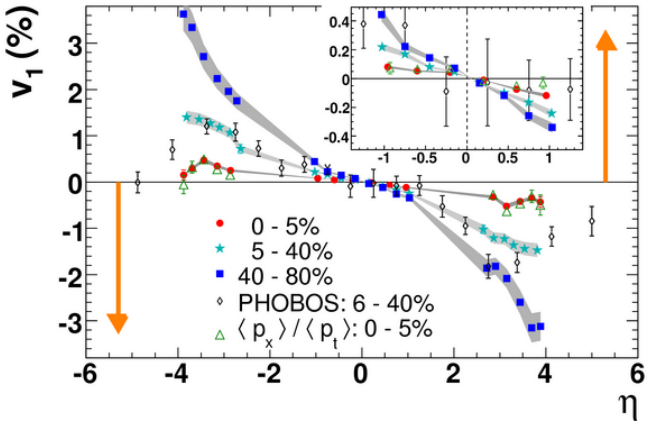

Figure 5.27: Charged particle $v_1\,(\eta)$ for three centralities in Au+Au collisions at 200 GeV as measured by the STAR collaboration. The arrows indicate the algebraic sign of v_1 for spectator neutrons, and their positions on the η axis correspond to beam rapidity. The inset shows the mid-η region in more detail. The error bars are statistical, and the shaded bands show systematic errors. PHOBOS results [13] are also shown for midcentral collisions.[5]

The other fact to take away from the discrepancy between ALICE's result and that of CMS is the magnitude being appreciably off. As they contend in their paper, ALICE believes that any measurement made using an EP in the participant zone of the collision has very little correlation to any v_1 measurement made using an EP from the region of spectator matter, their difference is shown in Fig. 5.28.

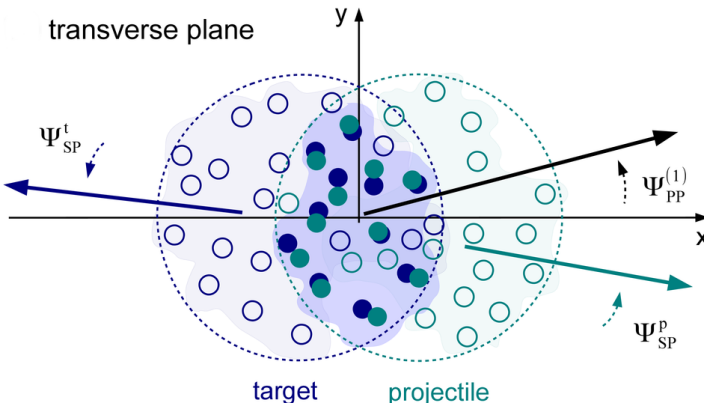

Figure 5.28: Cartoon of a non-central heavy ion collision[4].

However, STAR has shown that, at least at RHIC energies, the measurement of v_1^{odd} is the same regardless if you use a spectator plane (ZDC-SMD), a participant plane (EP_1, EP_2) or a three particle cumulant (3), as shown in Fig. 5.29. As of the writing of this thesis there is no result that can be directly compared to the ALICE measurement to confirm or refute the findings this is because ATLAS nor CMS has the capabilities to make an EP estimation using spectator neutrons.

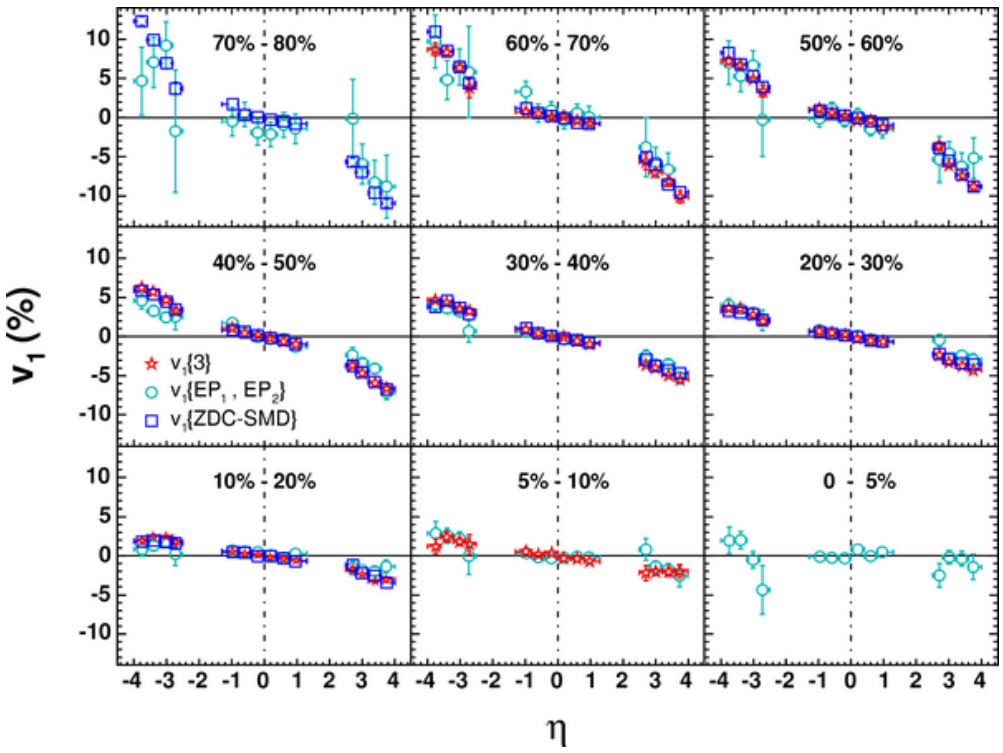

Figure 5.29: Directed flow of charged particles as a function of pseudorapidity for different centralities. The plotted errors are statistical only, and systematic effects are discussed in [10]

The v_1^{even} measured by both ATLAS and CMS in Fig. 5.23 shows a very weak dependence on centrality. For the low luminosity runs in 2010 and 2011 this is consistent with dipole-like fluctuations of the initial energy in the participant zone. CMS' result is also the first v_1 measurement ever made using the methods prescibed in [34]. The discrepancies at higher values of transverse momenta are likely due to the limitations of CMS' tracking reconstruction in 2010 during Heavy Ion running, and any impact in track reconstruction not only limits the v_1 measurement but also the accuracy of Ψ_1 in this specific analysis. As of the writing of this thesis,

the analysis has not been re-performed using all of the final track reconstruction development made during the winter of 2014.

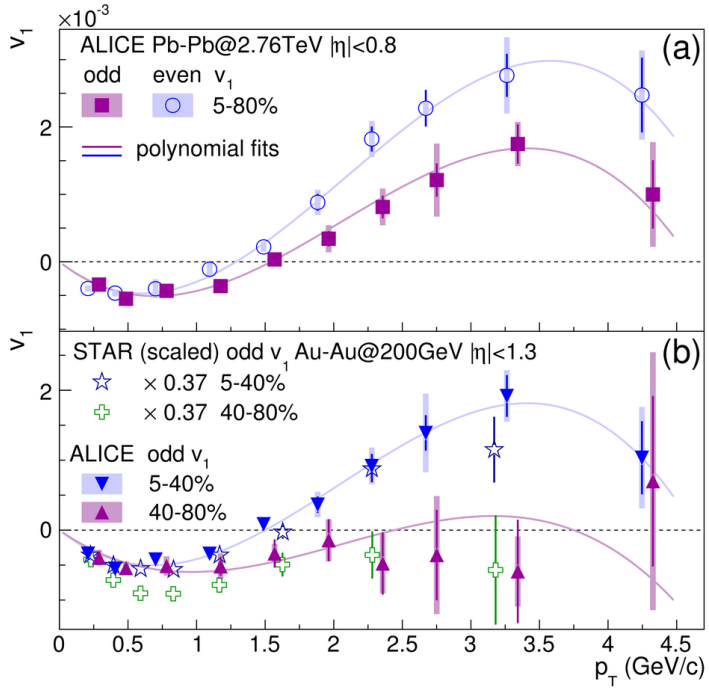

Figure 5.30: (a) v_1 versus transverse momentum measured by ALICE. (b) v_1^{odd} comparison with STAR data[5]. Lines represent fits with a third order polynomial [4]

Figure 5.30 shows the measurement of $v_1^{even}(p_T)$ from the ALICE collaboration. They report values that are 40x smaller than that measured here by CMS and by ATLAS. The discrepancy here further backs ALICE's assertion that the participant and spectator collision symmetry planes are weakly correlated. Understanding this discrepancy is an important experimental contribution for modelling the poorly understood initial conditions in heavy ion collisions.

Future Studies

Future studies to be preformed would include the measurement of v_1 as functions of both pseudorapidity and transverse momentum using the CMS Spectator Reaction Plane Detector(RPD) planned for installation for the start of heavy ion collisions in 2015. This will allow CMS to make a measurement that can be directly compared to the ALICE results for directed flow. In addition a study of v_1 for identified charged particles would give an interesting constraint on the early evolution of the nuclear medium. A similar measurement was done by STAR and can be seen in Fig.5.31.

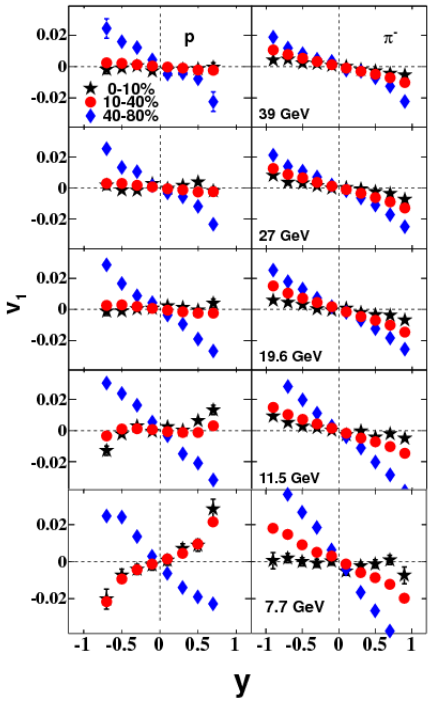

Figure 5.31: Directed flow for protons and for negative pions as a function of rapidity for central, mid-central, and peripheral collisions at various beam energies as measured by the STAR experiment [8]. Only satistical errors are shown.

An analysis of the directed flow will also be carried out using additional methods not mentioned in this work. These methods include the 2 and 3 particle cumulant methods used by ATLAS and STAR, respectively. The last method uses the information stored in eigenvectors to extract, not just flow, but also to estimate non-flow effects in the detector [17]. These three measurements are currently underway.

Bibliography

[1] Centrality determination for heavy ion data 2010. *CMS Analysis Note*, AN-10-412, 2010.

[2] Tracking and Vertexing Results from First Collisions. Technical Report CMS-PAS-TRK-10-001, CERN, 2010. Geneva, 2010.

[3] G. Aad et al. Measurement of the azimuthal anisotropy for charged particle production in $\sqrt{s_{NN}} = 2.76$ tev lead-lead collisions with the atlas detector. *Phys. Rev. C*, 86:014907, Jul 2012.

[4] B. Abelev et al. Directed flow of charged particles at midrapidity relative to the spectator plane in pb-pb collisions at $\sqrt{s_{NN}} = 2.76$ tev. *Phys. Rev. Lett.*, 111:232302, Dec 2013.

[5] B. I. Abelev et al. System-size independence of directed flow measured at the bnl relativistic heavy-ion collider. *Phys. Rev. Lett.*, 101:252301, Dec 2008.

[6] Wolfgang Adam, Boris Mangano, Thomas Speer, and Teddy Todorov. Track Reconstruction in the CMS tracker. Technical Report CMS-NOTE-2006-041, CERN, Geneva, Dec 2006.

[7] L. Adamczyk et al. Directed flow of identified particles in Au + Au collisions at $\sqrt{S_{NN}} = 200$ GeV at rhic. *Phys. Rev. Lett.*, 108:202301, May 2012.

[8] L. Adamczyk et al. Beam-energy dependence of the directed flow of protons, antiprotons, and pions in au+au collisions. *Phys. Rev. Lett.*, 112:162301, Apr 2014.

[9] J. Adams et al. Azimuthal anisotropy at the relativistic heavy ion collider: The first and fourth harmonics. *Phys. Rev. Lett.*, 92:062301, Feb 2004.

[10] J. Adams et al. Directed flow in au+au collisions at $\sqrt{s_{NN}}$=62.4 gev. *Phys. Rev. C*, 73:034903, Mar 2006.

[11] G. Agakishiev et al. Directed and elliptic flow of charged particles in cu + cu collisions at $\sqrt{s_{NN}} = 22.4$ gev. *Phys. Rev. C*, 85:014901, Jan 2012.

[12] C. Alt et al. Directed and elliptic flow of charged pions and protons in pb+pb collisions at 40a and 158a gev. *Phys. Rev. C*, 68:034903, Sep 2003.

[13] B. B. Back et al. Energy dependence of directed flow over a wide range of pseudorapidity in au+au collisions at the bnl relativistic heavy ion collider. *Phys. Rev. Lett.*, 97:012301, Jul 2006.

[14] David Barney. Large Transverse View of CMS. Novemeber 2011.

[15] J. Barrette et al. Proton and pion production relative to the reaction plane in au + au collisions at 11a *gev/c*. *Phys. Rev. C*, 56:3254–3264, Dec 1997.

[16] J. Beringer et al. Review of particle physics. *Phys. Rev. D*, 86:010001, Jul 2012.

[17] Rajeev S. Bhalerao, Jean-Yves Ollitrault, Subrata Pal, and Derek Teaney. Principal component analysis of event-by-event fluctuations. *Phys. Rev. Lett.*, 114:152301, Apr 2015.

[18] P. Billoir and S. Qian. Simultaneous pattern recognition and track fitting by the kalman filtering method. *Nuclear Instruments and Methods in Physics Research Section A: Accelerators, Spectrometers, Detectors and Associated Equipment*, 294(12):219 – 228, 1990.

[19] G. Bishop and G. Welch.

[20] J. Bleibel, G. Burau, and C. Fuchs. Anisotropic flow in pb + pb collisions at {LHC} from the quarkgluon string model with parton rearrangement. *Physics Letters B*, 659(3):520 – 524, 2008.

[21] V. Blobel. Software alignment for tracking detectors. *Nuclear Instruments and Methods in Physics Research Section A: Accelerators, Spectrometers, Detectors and Associated Equipment*, 566(1):5 – 13, 2006. {TIME} 2005 Proceedings of the 1st Workshop on Tracking in High Multiplicity Environments 1st Workshop on Tracking in High Multiplicity Environments.

[22] Jean-Luc Caron. Overall view of LHC experiments.. Vue d'ensemble des experiences du LHC. AC Collection. Legacy of AC. Pictures from 1992 to 2002., May 1998.

[23] S. Chatrchyan et al. Dependence on pseudorapidity and on centrality of charged hadron production in pbpb collisions at $\sqrt{s_{\mathrm{NN}}} = 2.76tev$. *Journal of High Energy Physics*, 2011(8), 2011.

[24] S. Chatrchyan et al. Observation of a new boson at a mass of 125 gev with the {CMS} experiment at the {LHC}. *Physics Letters B*, 716(1):30 – 61, 2012.

[25] Collaboration CMS. CMS collision events: first lead ion collisions. CMS Collection., Nov 2010.

[26] CMS Collaboration. Transverse-momentum and pseudorapidity distributions of charged hadrons in pp collisions at $\sqrt{s} = 7$ TeV. *Phys. Rev. Lett.*, 105:022002, 2010.

[27] The CMS Collaboration, S Chatrchyan, et al. The cms experiment at the cern lhc. *Journal of Instrumentation*, 3(08):S08004, 2008.

[28] L. P. Csernai, V. K. Magas, H. Stöcker, and D. D. Strottman. Fluid dynamical prediction of changed v_1 flow at energies available at the cern large hadron collider. *Phys. Rev. C*, 84:024914, Aug 2011.

[29] Susanna Cucciarelli, Marcin Konecki, Danek Kotlinski, and Teddy Todorov. Track reconstruction, primary vertex finding and seed generation with the Pixel Detector. Technical Report CMS-NOTE-2006-026, CERN, Geneva, Jan 2006.

[30] Susanna Cucciarelli, Danek Kotlinski, and Teddy Todorov. Position Determination of Pixel Hits. Technical Report CMS-NOTE-2002-049, CERN, Geneva, Nov 2002.

[31] V. ern. Thermodynamical approach to the traveling salesman problem: An efficient simulation algorithm. *Journal of Optimization Theory and Applications*, 45(1):41–51, 1985.

[32] G Flucke, P Schleper, G Steinbrck, and M Stoye. Cms silicon tracker alignment strategy with the millepede ii algorithm. *Journal of Instrumentation*, 3(09):P09002, 2008.

[33] R. Frhwirth. Application of kalman filtering to track and vertex fitting. *Nuclear Instruments and Methods in Physics Research Section A: Accelerators, Spectrometers, Detectors and Associated Equipment*, 262(23):444 – 450, 1987.

[34] Fernando G. Gardim, Frédérique Grassi, Yogiro Hama, Matthew Luzum, and Jean-Yves Ollitrault. Directed flow at midrapidity in event-by-event hydrodynamics. *Phys. Rev. C*, 83:064901, Jun 2011.

[35] Veikko Karimki, Tapio Lampen, and Frank-Peter Schilling. The HIP Algorithm for Track Based Alignment and its Application to the CMS Pixel Detector. Technical Report CMS-NOTE-2006-018, CERN, Geneva, Jan 2006.

[36] S. Kirkpatrick, C.D. Gelatt Jr., and M.P. Vecchi. Optimization by simulated annealing. *Science*, 220(4598):671–680, 1983. cited By 16381.

[37] Thomas Lenzi. Development and Study of Different Muon Track Reconstruction Algorithms for the Level-1 Trigger for the CMS Muon Upgrade with GEM Detectors. 2013.

[38] Ting Miao, N Leioatts, Hans Wenzel, and Francisco Yumiceva. Beam Position Determination using Tracks. Technical Report CMS-NOTE-2007-021, CERN, Geneva, Aug 2007.

[39] Jean-Yves Ollitrault, Arthur M. Poskanzer, and Sergei A. Voloshin. Effect of flow fluctuations and nonflow on elliptic flow methods. *Phys. Rev. C*, 80:014904, Jul 2009.

[40] A. M. Poskanzer and S. A. Voloshin. Methods for analyzing anisotropic flow in relativistic nuclear collisions. *Phys. Rev. C*, 58:1671–1678, Sep 1998.

[41] Dr. Eric Michael Richardson. *Elliptic Flow at Forward Rapidity in* $\sqrt{s_{NN}}$ *= 200 GeV Au+Au Collisions*. PhD thesis, University of Maryland, 2012.

[42] Christof Roland. Track Reconstruction in Heavy Ion Events using the CMS Tracker. Technical Report CMS-NOTE-2006-031, CERN, Geneva, Jan 2006.

[43] K. Rose. Deterministic annealing for clustering, compression, classification, regression, and related optimization problems. *Proceedings of the IEEE*, 86(11):2210–2239, Nov 1998.

[44] Tai Sakuma and Thomas McCauley. Detector and event visualization with sketchup at the cms experiment. *Journal of Physics: Conference Series*, 513(2):022032, 2014.

[45] Thomas Speer, Kirill Prokofiev, R Frhwirth, Wolfgang Waltenberger, and Pascal Vanlaer. Vertex Fitting in the CMS Tracker. Technical Report CMS-NOTE-2006-032, CERN, Geneva, Feb 2006.

[46] Peter-John Stanskas. *The Centrality Dependence of Flow in Au+Au Collisions at 8 and 10.8 AGeV*. PhD thesis, University of Maryland, 2001.

[47] M Swartz, D Fehling, G Giurgiu, P Maksimovic, and V Chiochia. A new technique for the reconstruction, validation, and simulation of hits in the CMS Pixel Detector. *PoS*, Vertex 2007(CMS-NOTE-2007-033):035. 37 p, Jul 2007.

[48] CERN Tejinder S. Virdee. Assembly of the CMS HF (hadron forward) calorimeter, April 2003 to June 2005. CMS Collection., Jun 2005.

[49] Sergei A. Voloshin, Arthur M. Poskanzer, and Raimond Snellings. Collective phenomena in non-central nuclear collisions. 2008.